

Aus dem
Deutschen Herzzentrum der Charité
Klinik für Angeborene Herzfehler/ Kinderkardiologie
Direktor: Professor Dr. med. Felix Berger

und dem
Institut für kardiovaskuläre Computer-assistierte Medizin
Institutsleiter: Professor Dr. med. Titus Kühne

Habilitationsschrift

Präzisionsmedizin in der Kinder- und Erwachsenenkardiologie – klinische Anwendung bildbasierter *in silico* Modellierung

zur Erlangung der Lehrbefähigung
für das Fach Experimentelle Kinderkardiologie

vorgelegt dem Fakultätsrat der Medizinischen Fakultät
Charité-Universitätsmedizin Berlin

von

Dr. med. Lisa Marie Schafstedde

Eingereicht: März 2023

Dekan: Professor Dr. med. Joachim Spranger

1. Gutachterin: Frau Prof. Dr. Inga Voges, Kiel
2. Gutachterin: Frau Prof. Dr. Sandy Engelhardt, Heidelberg

Inhaltsverzeichnis

Abkürzungsverzeichnis.....	2
1. Einleitung	3
1.1 Technischer Hintergrund verschiedener Simulationsverfahren	5
1.2 Klinische Anwendungsbeispiele im Bereich der Kinder- und Erwachsenenkardiologie	8
2. Fragestellung und Zielsetzung	11
3. Eigene Arbeiten.....	12
3.1 Proof of Concept: Bildbasierte Modellierung hämodynamischer Parameter für die patientenspezifische virtuelle Therapieplanung.....	12
3.2 Validierung der patientenspezifischen virtuellen Therapieplanung gegen den klinischen Goldstandard	24
3.3 Erste Anwendung der patientenspezifischen virtuellen Therapieplanung am Beispiel von drei Patient*innen mit komplexer univentrikulärer Physiologie	37
3.4 Optimierung: Einsatz von künstlicher Intelligenz anstelle computergestützter Strömungssimulationen für eine bessere klinische Translation	56
3.5 Optimierung: Nutzen synthetischer Patientenkollektive zum Überwinden existierender klinischer Datenlücken.....	70
4. Diskussion	85
4.1 Bildbasierte <i>in silico</i> Modellierung hämodynamischer Parameter.....	85
4.2 Validierung gegen den klinischen Goldstandard des Herzkatheters	86
4.3 Klinische Anwendung der virtuellen Therapieplanung	88
4.4 Einsatz von künstlicher Intelligenz anstelle numerischer Strömungssimulationen für eine bessere klinische Translation	91
4.5 Nutzen synthetischer Patientenkollektive zum Überwinden existierender klinischer Datenlücken	93
5. Zusammenfassung und Ausblick.....	96
Literaturverzeichnis	97
Danksagung.....	105
Erklärung	106

Abkürzungsverzeichnis

AKE	Aortenklappenersatz
ANN	Artificial Neural Network, zu Deutsch: künstliches neuronales Netz
AS	Aortenklappenstenose
AVA	Aortic Valve Area, zu Deutsch: Aortenklappenöffnungsfläche
CFD	Computational Fluid Dynamics, zu Deutsch: computergestützte Strömungssimulationen
CT	Computertomographie
DL	Deep Learning
FVM	Finite-Volumen-Methode
GAN	Generative Adversarial Network, zu Deutsch: erzeugende gegnerische Netzwerke
ISTA	Aortenisthmusstenose
KI	Künstliche Intelligenz
ML	Maschinelles Lernen
MRT	Magnetresonanztomographie
PAVM	Pulmonale arteriovenöse Malformation
PCA	Principal Component Analysis, zu Deutsch: Hauptkomponenten-Analyse
PPM	Patient-Prothesis-Mismatch, zu Deutsch: Klappen-Prothesen-Mismatch
RKLD	Relative Kullback-Leibler Divergenz
SD	Standard Deviation, zu Deutsch: Standardabweichung
SSM	Statistical Shape Model, zu Deutsch: statistisches Formmodell
TAVI	Transcatheter Aortic Valve Implantation, zu Deutsch: Transkatheter Aortenklappenimplantation
TCPC	Total Cavopulmonary Connection, zu Deutsch: totale kavopulmonale Verbindung
TPG	Transvalvular Pressure Gradient, zu Deutsch: transvalvulärer Druckgradient
WSS	wall shear stress, zu Deutsch: Wandschubspannung

1. Einleitung

Die Möglichkeit verschiedene Organsysteme virtuell abzubilden, bietet ein großes Potential für die personalisierte Medizin. Dabei kann nicht nur die Funktion des jeweiligen Organs virtuell simuliert werden, sondern auch mögliche Manipulationen im Sinne von operativen oder interventionellen Eingriffen. Die richtige Therapie zum richtigen Zeitpunkt, nichtinvasiv und patientenindividuell zu identifizieren, ist das große Ziel der Präzisionsmedizin.¹

Durch den stetigen Fortschritt sowohl im Bereich der Bildgebung als auch in mathematischen Modellierungstechniken sowie einer zunehmenden Verfügbarkeit von leistungsstarker Informationstechnologie, gewinnen *in silico* (angelehnt an das Lateinische „*in silicio*“, also „*in silicium*“ bzw. im übertragenden Sinne im Computer ablaufende) Modellierungsverfahren eine immer größere Bedeutung auch im Bereich der kardiovaskulären Medizin.²⁻⁴

Die Grundlage solcher Modellierungsansätze sind medizinische Bilddaten (Echo, Computer- oder Magnetresonanztomographie), sodass der Begriff der bildbasierten Modellierung („image-based modelling“) geprägt wurde. Basierend auf Rekonstruktionen der dreidimensionalen Herz- und Gefäßanatomie sowie Informationen zu den patientenspezifischen Randbedingungen können numerische Verfahren angewendet werden, um verschiedene Parameter der kardialen Funktion und Hämodynamik zu quantifizieren.

Die bildbasierte *in silico* Modellierung von Hämodynamik und Funktion des Herzens kann dabei einerseits helfen, die diagnostische Aussagekraft unterschiedlicher Bildgebungsmodalitäten zu erweitern, andererseits aber auch, verschiedene Parameter der postinterventionellen bzw. postoperativen Funktion vorherzusagen und so das geeignete patientenindividuelle Therapieverfahren zu identifizieren.⁵⁻⁸ So kann zum Beispiel mittels numerischer Modellierung der Druckverlust über einer Herzklappe quantifiziert werden, ohne dass dafür eine kosten- und vor allem strahlenintensive Herzkatheteruntersuchung durchgeführt werden muss.^{9,10} Aber auch bei Patient*innen mit Klappeninsuffizienzen, welche entweder mittels Klappenersatz oder -rekonstruktion behandelt werden können, wurden bereits erste virtuelle Werkzeuge entwickelt, mit deren Hilfe es möglich ist, die Veränderungen des Klappenanus, die chirurgisch induzierten Gewebedehnungen oder aber die resultierenden Nahtkräfte nach durchgeföhrter Anuloplastik bereits präoperativ zu quantifizieren und hämodynamische Parameter des postoperativen Zustands vorherzusagen.^{11,12}

Im Bereich der pädiatrischen Kardiologie, insbesondere bei Patient*innen mit komplexen angeborenen Herzfehlern, ist eine individualisierte Therapieplanung zudem von ganz besonderer

Bedeutung. Da die Anatomie des kardiovaskulären Systems in diesem Patientenkollektiv hoch individuell ist, gibt es häufig keine für das jeweilige Krankheitsbild einheitliche Therapie. Die virtuelle Behandlungsplanung bietet hier ein großes Potential für die multimodale Therapiefindung.^{8,13-15}

Die Translation solcher Modellierungsansätze in die Klinik stellt jedoch weiterhin eine große Hürde dar.^{16,17} Einerseits muss die Genauigkeit der jeweiligen Simulationsmethode quantifiziert und die Methode selbst validiert werden. Dafür benötigt es in der Regel eine hohe Anzahl an Patientendaten, die insbesondere in der Kinderkardiologie, aber auch aufgrund zunehmend strengerer Datenschutzrichtlinien häufig nicht zur Verfügung stehen. Andererseits sind die Simulationsverfahren sehr komplex und verlangen neben einer hohen technischen Expertise auch beachtliche Rechenkapazitäten und -laufzeiten, wodurch sich ihr routinemäßiger Einsatz in der Klinik ebenfalls verkompliziert.

Das Problem der hohen Komplexität könnte durch den Einsatz künstlicher Intelligenz überwunden werden.¹⁸ Ein maschinelles Modell, wenn einmal trainiert, bietet den Vorteil, komplexe häodynamische Zusammenhänge schnell zu analysieren und damit häodynamische Ergebnisse akkurat und in Echtzeit vorherzusagen, ohne dass für die konkrete Anwendung ein hohes Fachwissen oder spezielle technische Voraussetzungen vonnöten wären. Fehlende klinische Daten wiederum könnten mittels synthetischer Daten augmentiert werden, sodass sowohl für mögliche Validierungsstudien als auch zum Trainieren des maschinellen Algorithmus' ein ausreichend großer Datensatz zur Verfügung stünde.

In der vorliegenden Habilitationsschrift wird zunächst am Beispiel des Aortenklappenersatzes gezeigt, wie in silico Modellierung häodynamischer Parameter für die patientenindividuelle Therapieplanung funktionieren kann⁹ sowie eine Validierung der bildbasierten Modellierung gegen den klinischen Goldstandard des Herzkatheters vorgestellt.¹⁹ Am Beispiel von komplexen Patient*innen aus dem Bereich der Kinderkardiologie wird die Anwendung und der klinische Nutzen der patientenspezifischen Therapieplanung gezeigt.²⁰ Zuletzt werden zwei Optimierungsvorschläge beschrieben, die den Einsatz von künstlicher Intelligenz als Alternative zu computergestützten Strömungssimulationen für eine bessere klinische Translation²¹ sowie den Nutzen synthetischer Patientenkohorten zum Überwinden existierender klinischer Datenlücken zeigen.²²

1.1 Technischer Hintergrund verschiedener Simulationsverfahren

1.1.1 Bildbasierte Modellierung

Um die patientenspezifische Strömung innerhalb des Herzens beziehungsweise der zu- oder abführenden Gefäße zu simulieren, wird zum einen ein genaues, dreidimensionales Modell benötigt und zum anderen Informationen über den Zu- und Abfluss. Beides lässt sich aus klinischen Bilddaten, wie zum Beispiel der kardialen Magnetresonanztomographie (MRT) oder der Computertomographie (CT) ableiten.²³

Zur Erzeugung eines dreidimensionalen Modells muss zunächst die entsprechende Region aus den Bilddaten rekonstruiert werden. Diese Rekonstruktion erfolgt entweder manuell, automatisch mittels eines geeigneten Algorithmus oder als Kombination aus manuellen und automatisierten Methoden. Um die patientenspezifischen Flussinformationen zu erhalten, braucht es entweder zeitlich aufgelöste Bildaufnahmen, wodurch Volumenänderungen und damit letztlich Volumenströme quantifiziert werden können oder spezielle Sequenzen, wie beispielsweise 4D Fluss MRT-Sequenzen, auf deren Grundlage zeitlich aufgelöste Geschwindigkeiten im Gefäß bestimmt werden können.

Liegen sowohl Informationen über die Gefäßgeometrie als auch über die dazu gehörigen Randbedingungen vor (beispielsweise Flussvolumina, Drücke, oder aber literaturbasierte Annahmen), können sogenannte numerische Simulationsverfahren angewendet und die Strömung innerhalb eines Gefäßes berechnet werden.²⁴

1.1.2 Numerische Strömungssimulation

Die Strömung von Fluiden lässt sich im Allgemeinen durch eine Reihe von Gleichungen, die sogenannten Navier-Stokes-Gleichungen, für die Erhaltung von Impuls und Masse beschreiben. Die numerische Strömungssimulation (englisch Computational Fluid Dynamics, CFD) verwendet dabei unterschiedliche Methoden zur näherungsweisen Lösung strömungsmechanischer Probleme. Die sogenannte Finite-Volumen-Methode (FVM) ist insbesondere für kompressible Strömungen geeignet, also für Fluide, deren Dichte mit ihrem Druck variiert, und stellt ein numerisches Verfahren dar, mit dessen Hilfe Druck- und Geschwindigkeitsfelder innerhalb eines vordefinierten Gebiets berechnet werden können. Sie stellt die in dieser Arbeit zugrundliegende Methode der CFD dar.

Mittels der FVM wird der Rechenbereich in diskrete Volumenelemente unterteilt und die Navier-Stokes-Gleichungen in integraler Form diskretisiert. Durch iterative numerische Lösungsverfahren wird anschließend deren Lösung auf Volumenelementen approximiert. Vereinfacht ausgedrückt

werden mittels der FVM komplexe mathematische Probleme in kleinere Teilbereiche unterteilt, die als „Finite-Volumen“ bezeichnet werden. Jedes Finite-Volumen wird dann einzeln untersucht und die Veränderungen der relevanten physikalischen Größen innerhalb dieses Volumens werden annäherungsweise berechnet. Diese Berechnungen werden schließlich zu einer Gesamtlösung zusammengeführt.

Für die Berechnung der aortalen Strömung beispielsweise, muss also ein enorm großes lineares Gleichungssystem gelöst werden. Da es sich bei Blut zudem um ein nicht-kompressibles und nicht-newtonsches Fluid handelt, dessen Viskosität nicht konstant bleibt, müssen zusätzliche Modellierungsansätze für die Beschreibung der Viskosität angewendet werden, die die Laufzeit der Simulationen erhöhen. Außerdem gilt es zu berücksichtigen, dass bei den in der Aorta auftretenden Strömungsgeschwindigkeiten mit der Entstehung von turbulenten Strömungscharakteristiken zu rechnen ist, sodass weitere Turbulenzmodelle in die Strömungssimulation integriert werden müssen.

Es ergeben sich lange Laufzeiten der Berechnungen sowie ein Bedarf an hoher Rechenkapazität, um die Komplexität der zugrunde liegenden Strömungsmechanik rechnerisch zu erfassen.

1.1.3 Das künstliche neuronale Netz

Künstliche neuronale Netze (englisch artificial neural network, ANN) sind ein Unterzweig der künstlichen Intelligenz. Sie dienen vor allem der Abstraktion, beziehungsweise der Modellbildung von Informationsverarbeitung. Dabei lernt ein ANN Zusammenhänge zwischen Eingangs- und Zielgrößen und wird so trainiert, dass es am Ende für bestimmte Eingangsmuster zugehörige Ausgabemuster erzeugt. Es handelt sich dabei um einen sogenannten Funktionsapproximator.

Unterschiedliche Lernverfahren können für verschiedene Fragestellungen angewendet werden. Alle Lernverfahren benötigen dabei Trainings- und Testdaten, welche gut ausgewählt sein müssen, da durch einseitig ausgewählte Trainingsdaten fehlerhafte Muster durch das ANN „gelernt“ werden können. Unabhängig davon, welches Lernverfahren angewendet wird, am Ende entsteht ein Algorithmus, der in der Lage ist, hochdimensionale Probleme instantan berechnen zu können. Das heißt, wenn ein Algorithmus erst einmal erfolgreich trainiert wurde, wird für seine Anwendung weder eine hohe technische Expertise noch eine extreme Rechenkapazität gebraucht und hochkomplexe - beispielsweise strömungsmechanische - Probleme können in Echtzeit gelöst werden.

Die Grundidee der letzten zwei in dieser Habilitationsschrift vorgelegten Arbeiten besteht daher darin, die rechentechnisch aufwendige FVM mithilfe eines künstlichen neuronalen Netzes zu ersetzen, um

so die personalisierte *in silico* Modellierung möglicher Behandlungsoptionen für den klinischen Gebrauch leichter zugänglich zu machen.

1.1.4 Synthetische Patientenkohorten

Um eine hohe Genauigkeit des ANN zu erzielen, bedarf es jedoch einer großen Menge an Trainingsdaten. Im klinischen Kontext bedeutet dies eine hohe Anzahl an Patientendaten, welche nicht immer leicht zu akquirieren sind.

Einerseits gibt es das Problem existierender Datenlücken; nicht für jede Patient*in stehen alle demographischen Informationen, klinischen und laborchemischen Parameter oder Bilddateninformationen in gleichem Maße zur Verfügung. Andererseits gibt es aber auch klinische Bereiche, wie zum Beispiel das Feld der angeborenen Herzfehler, in dem aufgrund der Seltenheit ihres Vorkommens keine großen Patientenkohorten zu erwarten sind.

Künstliche, also synthetische Patientenkohorten könnten daher dabei helfen, die erforderliche Menge an Trainingsdaten für das erfolgreiche Entwickeln eines ANN bereit zu stellen.²⁵ Diesem Thema widmet sich die fünfte der in dieser Habilitationsschrift vorgelegten Arbeit.

Der zugrunde liegende Ansatz ist dabei die Erzeugung eines sogenannten statistischen Formmodells.²⁶ Mithilfe eines statistischen Formmodells lassen sich Formvarianten systematisch quantifizieren. Mögliche Zusammenhänge zwischen verschiedenen Formparametern werden hierbei durch das Formmodell analytisch ermittelt. Das Formmodell selbst beruht auf der sogenannten Hauptkomponentenanalyse (englisch principal component analysis, PCA). Durch sie können Datensätze vereinfacht werden, indem eine Vielzahl statistischer Variablen durch eine geringere Zahl möglichst aussagekräftiger „Hauptkomponenten“ beschrieben werden. Dabei ist das Ziel, dass möglichst wenig Informationen verloren gehen, während die Komplexität der Geometriebeschreibung reduziert wird.

So kann zum Beispiel die gesamte Anatomie des Aortenbogens auf verschiedene geometrische Komponenten reduziert werden.²⁷ Eine Kombination dieser geometrischen Komponenten erlaubt dann die Erzeugung künstlicher Geometrien und führt so zu einer Augmentierung des bestehenden Datensatzes.

1.2 Klinische Anwendungsbeispiele im Bereich der Kinder- und Erwachsenenkardiologie

1.2.1 Aortenklappenstenose

Die Aortenklappenstenose (AS) ist die häufigste Form der Herzklappenerkrankung mit einer Prävalenz von über 10% in der Gruppe der über 75-jährigen.^{28,29} Unbehandelt führt eine moderate bis schwere AS kurz- bis mittelfristig zum Tod.^{30,31} Derzeit existiert ein sehr breites Spektrum an Behandlungsmöglichkeiten, vom chirurgischen Aortenklappenersatz (AKE) bis hin zur kathetergestützten Aortenklappenimplantation (TAVI).^{32,33} Gemeinsames Ziel ist die Wiederherstellung eines physiologischen Flussprofiles über einer nicht-stenosierten Aortenklappe.

Doch es konnte gezeigt werden, dass auch nach durchgeföhrtem AKE abnorme Blutflussprofile persistieren.³⁴ Dies ist ein ernstzunehmendes Problem, da pathologische Veränderungen des Blutflussprofils und der Wandschubspannung (WSS) eine Dysfunktion der Endothelzellen und damit einen Wandumbau der Aorta auslösen können.^{35,36} Die Folge sind eine erhöhte Morbidität und Mortalität, nicht zuletzt durch ein erhöhtes Risiko für Aneurysmenbildung und pathologisches Remodeling des Myokards.³⁶⁻³⁸ Auch das Problem des sogenannten „Klappen-Prothesen-Mismatch“ (englisch patient-prothesis-mismatch, PPM), welches durch ein Missverhältnis zwischen implantierter Klappenprothesengröße und dem Aortendurchmesser der Patient*in entsteht, ist heutzutage weithin anerkannt.³⁹⁻⁴² Bei bis zu 20% aller Patient*innen nach AKE tritt ein solches PPM auf^{43,44} und die Langzeitfolgen sind fatal.^{40,45,46}

Eine valide Vorhersage des postoperativen oder -interventionellen Ergebnisses wäre daher von entscheidender Bedeutung, um die optimale Art der Behandlung für jede individuelle Anatomie zu identifizieren. Numerische Strömungssimulationen werden bereits eingesetzt, um ergänzende hämodynamische Informationen zu gewinnen, die mit klinischen Bildgebungsverfahren allein nicht direkt beurteilt werden können.^{2,47-49}

1.2.2 Aortenisthmusstenose

Im Bereich der Kinderkardiologie ist die Aortenisthmusstenose (ISTA) eine der häufigsten angeborenen Herzkrankheiten und manifestiert sich als lokale Verengung des Aortenbogens mit einem konsekutiv hohen Druckgradienten.^{50,51} In etwa 75% der Fälle liegt zudem eine bikuspide Aortenklappe vor.⁵² Während sich die Überlebenszeiten nach ISTA-Behandlung in den letzten Jahrzehnten deutlich verbessert haben, sind Langzeitkomplikationen wie die Bildung von

Aneurysmen, kardiovaskuläre Ereignisse, arterieller Bluthochdruck oder die Notwendigkeit zu Folgeeingriffen aufgrund von Re-Stenosierungen weiterhin eine klinische Herausforderung.⁵³⁻⁵⁵

Ein enges Monitoring der Patient*innen mit ISTA ist daher von besonderer Bedeutung. Dabei liegt der Fokus vor allem auf der Beurteilung und Kontrolle einer möglichen Re-Stenosierung sowie der Bestimmung des Druckgradienten über der Aortenklappe und der Stenose innerhalb des Aortenbogens. Mittels moderner Bildgebung (Echo, MRT, CT) kann die Stenose beurteilt werden, nicht selten ist jedoch auch eine strahlenbelastende und invasive Herzkatheteruntersuchung notwendig.

Eine patientenspezifische Modellierung der aortalen Strömung mittels geeigneter Simulationsverfahren wäre daher wünschenswert, um die strömungsmechanischen Verhältnisse innerhalb des Aortenbogens ohne zusätzliche Belastung für die Patient*in zu beurteilen. Darüber hinaus ließen sich verschiedene Therapieoptionen sowie das zu erwartende häodynamische Ergebnis simulieren, wodurch das individuelle Behandlungsergebnis verbessert werden könnte. Erste Arbeiten auf diesem Gebiet haben vielversprechende Ergebnisse gezeigt.^{8,56,57}

1.2.3 Univentrikuläre Fontanzirkulation

Einige besonders schwere Herzfehler in der Kinderkardiologie lassen sich nicht biventrikulär korrigieren, sondern nur mittels mehrschrittiger Operationsprozeduren nach dem Fontan-Prinzip palliieren. Dieses umfasst in der Regel drei Operationen, die in unterschiedlichen Lebensabschnitten der Patient*innen durchgeführt werden: Als erste die sogenannte Norwood-Operation in den ersten Lebenstagen nach der Geburt, bei der der Pulmonalarterienstamm vom Herzen abgetrennt und mit der Aorta verbunden wird. Zur Oxygenierung des venösen Blutes in der Lunge wird zudem ein Shunt zwischen einem Ast der Aorta und der Pulmonalarterie etabliert, sodass die Durchblutung von Lungenarterien und Aorta gesichert ist, allerdings auf Kosten einer zentralen Zyanose. In einem zweiten Schritt im Alter von ca. vier bis sechs Monaten, wird dann die sogenannten Glenn-Operation durchgeführt, bei der die obere Hohlvene vom rechten Vorhof abgetrennt und mit der Pulmonalarterie verbunden wird. Der zuvor geschaffene Shunt zwischen Aorta und Pulmonalarterie wird wieder entfernt. Insgesamt wird so der rechte Ventrikel entlastet, da das venöse Blut aus der oberen Körperhälfte nun am rechten Herzen vorbei direkt in die Lungenarterien geleitet wird. Lediglich das venöse Blut der unteren Körperhälfte mischt sich in diesem Zustand noch mit dem sauerstoffreichen Blut aus der Lunge im Körperkreislauf. In einem letzten Schritt, wenn die Patient*innen ca. zwei bis drei Jahre alt sind, wird dann die sogenannte totale kavopulmonale Anastomose (total cavopulmonary connection, TCPC) etabliert, wodurch die univentrikuläre Fontanzirkulation erreicht ist. Dabei wird auch das venöse Blut aus der unteren Körperhälfte in die

Pulmonalarterie geleitet, sodass das gesamte venöse Blut am rechten Herzen vorbei direkt in die Lungenarterien gelangt.

Infolge der kontinuierlichen Verbesserung der chirurgischen Techniken, der präoperativen Auswahlkriterien und der perioperativen Betreuung sowie Innovationen im Bereich der medizinischen und interventionellen Behandlungsstrategien erreichen immer mehr Kinder mit einem solchen angeborenen Herzfehler heutzutage das Erwachsenenalter und damit nehmen auch die Langzeitkomplikationen zu.⁵⁸⁻⁶⁰

Ein Beispiel ist die Entwicklung von sogenannten pulmonalen arteriovenösen Malformationen (PAVM). Das Fehlen eines hypothetisch angenommenen, bis heute noch nicht identifizierten „hepatischen Faktors“ in den Lungengefäßen von Patient*innen mit univentrikulärer Physiologie wird dabei als Ursache für die Entstehung solcher PAVM diskutiert.⁶¹ PAVM sind durch direkte Gefäßverbindungen zwischen den Lungenarterien und -venen charakterisiert und können den klinischen Verlauf von Patient*innen durch chronische Zyanose und Herzinsuffizienz nachhaltig verschlechtern. Während ein spezifischer „hepatischer Faktor“ bisher noch nicht identifiziert wurde, wird ein verminderter oder fehlender hepatovenöser Blutfluss in die Lungenarterien, welcher meist mit einer Flussdifferenz zwischen rechter und linker Pulmonalarterie verbunden ist, mit der Entwicklung von PAVM in Verbindung gebracht.⁶² Diese Beobachtung wird durch mehrere Fallberichte gestützt, in denen nach chirurgischer oder interventioneller Umleitung des Lebervenenblutes zu gleichen Anteilen in beide Pulmonalarterien die Auflösung von PAVM beschrieben wird.^{63,64}

Auch in einem solch komplexen Kontext könnte *in silico* Modellierung helfen, die geeignetste individuelle Therapiestrategie zu identifizieren und damit dazu beitragen, einem ohnehin bereits sehr belasteten Patientenkollektiv unnötig invasive Untersuchungen zu ersparen.^{14,65,66}

Anhand dieser drei vorgestellten Krankheitsbilder werden im Weiteren verschiedene Techniken der *in silico* Modellierung vorgestellt und Möglichkeiten erarbeitet, wie die klinische Translation der personalisierten Präzisionsmedizin leichter realisiert werden könnte.

2. Fragestellung und Zielsetzung

Das Ziel der in dieser Habilitationsschrift vorgelegten wissenschaftlichen Arbeiten war die Beantwortung folgender Fragen:

- Ist es möglich, verschiedene Parameter der postoperativen Hämodynamik basierend auf rein präoperativer Bildgebung akkurat vorherzusagen?
- Ist es möglich, funktionelle, hämodynamische Parameter basierend auf CT-Bildgebung akkurat zu quantifizieren und korrelieren diese Parameter mit dem klinischen Goldstandard der invasiven Herzkatheterdiagnostik?
- Wie lässt sich die virtuelle Therapieplanung im klinischen Kontext anwenden?
- Gibt es Möglichkeiten, den komplexen Arbeitsablauf der virtuellen Therapieplanung mittels künstlicher Intelligenz zu vereinfachen und somit leichter in den klinischen Alltag zu implementieren?
- Wie lässt sich das Problem der existierenden klinischen Datenlücken überwinden?

Dazu werden fünf Arbeiten mit den im Folgenden aufgeführten Themenschwerpunkten vorgestellt:

- **Proof of Concept:** Bildbasierte in silico Modellierung hämodynamischer Parameter für die patientenspezifische virtuelle Therapieplanung
- **Validierung:** Validierung der bildbasierten in silico Modellierung gegen den klinischen Goldstandard des Herzkatheters
- **Anwendung:** Erste Anwendung der patientenspezifischen virtuellen Therapieplanung am Beispiel von drei Patient*innen mit komplexer univentrikulärer Physiologie
- **Optimierung:**
 - 1) Einsatz von künstlicher Intelligenz als Alternative zu computergestützten Strömungssimulationen für eine bessere klinische Translation
 - 2) Nutzen synthetischer Patientenkollektive zum Überwinden existierender klinischer Datenlücken

3. Eigene Arbeiten

3.1 Proof of Concept: Bildbasierte Modellierung hämodynamischer Parameter für die patientenspezifische virtuelle Therapieplanung

Um zu zeigen, dass eine patientenindividuelle virtuelle Therapieplanung möglich ist, wurde zunächst eine Proof of Concept Studie durchgeführt. Sie stellt einen methodischen Ansatz vor, mit dessen Hilfe es möglich ist, für Patient*innen mit hochgradiger Aortenstenose und Indikation zum biologischen Aortenklappenersatz postoperative hämodynamische Parameter bereits präoperativ vorherzusagen.

Hemodynamic Modeling of Biological Aortic Valve Replacement Using Preoperative Data Only

Florian Hellmeier, Jan Brüning, Simon Sündermann, Lina Jarmatz, **Marie Schafstedde**, Leonid Goubergrits, Titus Kühne, Sarah Nordmeyer

Der nachfolgende Text entspricht inhaltlich dem Abstrakt der oben genannten Publikation als Übersetzung durch die Autorin:

*„Die Vorhersage der aortalen Hämodynamik nach chirurgischem biologischen Aortenklappenersatz (AKE) könnte dazu beitragen, die patientenindividuelle Therapieplanung und damit das postoperative Ergebnis zu verbessern. Ziel dieser Studie ist es, einen methodischen Ansatz vorzustellen, mit dessen Hilfe es möglich ist, für Patient*innen nach biologischem AKE postoperative hämodynamische Parameter (wie die maximale Geschwindigkeit über der Aortenklappe, den Druckgradienten über der Aortenklappe, die Wandparallelität des aortalen Blutflusses oder die Flussexzentrität) basierend auf rein präoperativer Bildgebung vorherzusagen.“*

*Für 10 Patient*innen mit Indikation zum biologischen AKE wurde zusätzlich ein virtueller AKE durchgeführt. Genutzt wurden dafür lediglich die präoperativ aufgenommenen 4D-Fluss MRT Daten. Anschließend wurden computergestützte Strömungssimulationen (CFD) durchgeführt und die oben genannten hämodynamischen Parameter zwischen den postoperativen 4D Fluss Daten und den CFD-Ergebnissen verglichen.*

Es zeigte sich eine starke Korrelation zwischen den 4D Fluss- und CFD-basierten Parametern der maximalen Geschwindigkeit und des Druckgradienten ($R^2=0.75$ und $R^2=0.81$) mit einem mittleren quadratischen Fehler von 0.21 m/s bzw. 3.8 mmHg. Die Parameter der Wandparallelität sowie der

Flussexzentrizität waren jedoch mit $R^2=0.44$ bzw. $R^2=0.20$ nur mäßig und schwach korreliert. Die Visualisierung der Strömung durch Stromlinien zeigte in den meisten Fällen eine gute qualitative Übereinstimmung zwischen den 4D Fluss-Daten und den CFD-basierten Ergebnissen.

*Mittels dem in dieser Arbeit vorgestellten Ansatz scheint es möglich zu sein, hämodynamische Parameter wie die maximale Geschwindigkeit sowie den Druckgradienten über der Aortenklappe für Patient*innen mit Indikation zum biologischen AKE basierend auf rein präoperativer MRT-Bildgebung akkurat vorherzusagen. Der dafür notwendige Arbeitsablauf kann in einem angemessenen Zeitrahmen durchgeführt werden und bietet die Möglichkeit, die postoperative Klappenprothesenleistung abzuschätzen und damit Patient*innen mit erhöhtem Risiko für ein sogenanntes „Klappen-Prothesen-Mismatch“ bereits präoperativ zu identifizieren. Für neuere Parameter wie die Wandparallelität des aortalen Blutflusses oder die Flussexzentrizität scheint die präoperative Vorhersage schwieriger zu sein. Eine weitere Optimierung des Arbeitsablaufes sowie die Validierung der Ergebnisse sind ausstehend.“*



Hemodynamic Modeling of Biological Aortic Valve Replacement Using Preoperative Data Only

Florian Hellmeier^{1*}, Jan Brünig¹, Simon Sündermann^{2,3,4}, Lina Jarmatz¹,
Marie Schafstedde^{1,5,6}, Leonid Goubergrits^{1,7}, Titus Kühne^{1,4,6} and Sarah Nordmeyer^{1,6}

¹ Charité - Universitätsmedizin Berlin, Institute for Imaging Science and Computational Modelling in Cardiovascular Medicine, Berlin, Germany, ² Charité - Universitätsmedizin Berlin, Department of Cardiovascular Surgery, Berlin, Germany, ³ German Heart Center Berlin, Department of Cardiothoracic and Vascular Surgery, Berlin, Germany, ⁴ DZHK (German Center for Cardiovascular Research), Partner Site Berlin, Berlin, Germany, ⁵ Berlin Institute of Health (BIH), Berlin, Germany, ⁶ German Heart Center Berlin, Department of Congenital Heart Disease, Berlin, Germany, ⁷ Einstein Center Digital Future, Berlin, Germany

OPEN ACCESS

Edited by:

Stefan Stortecky,
Bern University Hospital, Switzerland

Reviewed by:

Dominik Obrist,
University of Bern, Switzerland
Paul Philipp Heinisch,
Bern University Hospital, Switzerland

Dario De Marinis,
University of Bern, Switzerland
Silje Ekroll Jahren,
University of Bern, Switzerland

*Correspondence:

Florian Hellmeier
florian.hellmeier@charite.de

Specialty section:

This article was submitted to
Structural Interventional Cardiology,
a section of the journal
Frontiers in Cardiovascular Medicine

Received: 12 August 2020

Accepted: 21 December 2020

Published: 09 February 2021

Citation:

Hellmeier F, Brünig J, Sündermann S, Jarmatz L, Schafstedde M, Goubergrits L, Kühne T and Nordmeyer S (2021) Hemodynamic Modeling of Biological Aortic Valve Replacement Using Preoperative Data Only. *Front. Cardiovasc. Med.* 7:593709.
doi: 10.3389/fcvm.2020.593709

Objectives: Prediction of aortic hemodynamics after aortic valve replacement (AVR) could help optimize treatment planning and improve outcomes. This study aims to demonstrate an approach to predict postoperative maximum velocity, maximum pressure gradient, secondary flow degree (SFD), and normalized flow displacement (NFD) in patients receiving biological AVR.

Methods: Virtual AVR was performed for 10 patients, who received actual AVR with a biological prosthesis. The virtual AVRs used only preoperative anatomical and 4D flow MRI data. Subsequently, computational fluid dynamics (CFD) simulations were performed and the abovementioned hemodynamic parameters compared between postoperative 4D flow MRI data and CFD results.

Results: For maximum velocities and pressure gradients, postoperative 4D flow MRI data and CFD results were strongly correlated ($R^2 = 0.75$ and $R^2 = 0.81$) with low root mean square error (0.21 m/s and 3.8 mmHg). SFD and NFD were moderately and weakly correlated at $R^2 = 0.44$ and $R^2 = 0.20$, respectively. Flow visualization through streamlines indicates good qualitative agreement between 4D flow MRI data and CFD results in most cases.

Conclusion: The approach presented here seems suitable to estimate postoperative maximum velocity and pressure gradient in patients receiving biological AVR, using only preoperative MRI data. The workflow can be performed in a reasonable time frame and offers a method to estimate postoperative valve prosthesis performance and to identify patients at risk of patient-prosthesis mismatch preoperatively. Novel parameters, such as SFD and NFD, appear to be more sensitive, and estimation seems harder. Further workflow optimization and validation of results seems warranted.

Keywords: aortic valve replacement, virtual intervention, CFD, 4D flow MRI, hemodynamics

INTRODUCTION

Nine thousand eight hundred and twenty nine surgical isolated aortic valve replacements (AVR) and at least 13,279 transcatheter aortic valve implantations (TAVI) were performed in Germany in 2018. Approximately 10% of the surgical AVRs used mechanical prostheses, with the remainder being tissue valve prostheses of animal or human origin, while TAVI currently exclusively use tissue valve prostheses (1). In general, the decision whether to use a surgical or transcatheter approach as well as the choice of prosthesis material is a clinical one and considers, among other factors, age, life expectancy, risk of surgery, indications and contraindications for anticoagulation, other preexisting cardiovascular conditions, and the will of the patient.

A clinically relevant problem after AVR is patient-prosthesis mismatch (PPM), typically classified by indexed effective orifice area (IEOA), which is defined as the effective orifice area (EOA) of the prosthesis in cm^2 normalized with the body surface area in m^2 . For echocardiography-based IEOA, values above $0.85 \text{ cm}^2/\text{m}^2$ are commonly classified as no PPM, values between $0.65 \text{ cm}^2/\text{m}^2$ and $0.85 \text{ cm}^2/\text{m}^2$ as moderate PPM, and values below $0.65 \text{ cm}^2/\text{m}^2$ as severe PPM (2). PPM has been shown to lead to increased morbidity and mortality as well as decreased left ventricular mass regression following AVR (2, 3). Mechanistically, PPM leads to increased cardiac workload through higher-than-normal postoperative aortic valve resistance and may require redo AVR. Other parameters to assess the effect of prosthesis size on hemodynamics are maximum velocity and pressure gradient across the aortic valve. Please note that the term “pressure gradient” is used in its medical sense, describing what is essentially a pressure difference. Parameters quantifying aortic hemodynamics include secondary flow degree (SFD) and normalized flow displacement (NFD). SFD quantifies the amount of secondary flow while incorporating vessel orientation, unlike helicity, for example. It has previously been used to characterize aortic flows in the presence of valve prostheses (4), to evaluate hemodynamic reactions to exercise (5), and is related to wall shear stress (6). Regarding NFD, several groups identified an association between increased NFD and aortic dilation (7–9), while others found it to be related to left ventricular remodeling (10). Compared to jet angle, NFD seems to be a more reliable measure of flow eccentricity (11).

Maximum velocity and pressure gradient are typically estimated using echocardiography in clinical settings. While inexpensive and readily available, echocardiography-based determination of velocities and pressure gradients is heavily operator-dependent and only able to capture velocity components in the direction of wave propagation. Current research by Adriaans et al. indicates that time-resolved phase-contrast magnetic resonance imaging (4D flow MRI) offers more consistent measurement of velocity fields (12).

Given that the hemodynamic result of AVR can currently only be assessed retroactively, it would be beneficial to develop computational approaches capable of providing hemodynamic estimates ahead of surgery, which could help in improving therapy planning and outcomes by providing additional information to clinicians. Computational fluid dynamics (CFD)

simulations provide a way to predict hemodynamic parameters, and predictive modeling of diseases of the aortic, coronary, and cerebral vasculature using CFD is a field of active research (13–15). Some current CFD models provide diagnostic accuracy comparable to clinical diagnostic procedures, e.g., in the estimation of fractional flow reserve (16, 17). The publications by Morris et al. (13) and Itatani et al. (14) also contain well-written introductions to CFD methods used in cardiovascular medicine, which may be helpful to readers unfamiliar with CFD. The online version of the former publication also contains two videos on the topic. There are various approaches for simulating aortic valve prosthesis hemodynamics, ranging from 2D models to spatially and temporally resolved FSI simulations including prosthesis leaflet dynamics (18, 19). Most studies focus on estimating specific properties, such as thrombogenicity of mechanical bi-leaflet prostheses, or comparing the hemodynamics of different prostheses types (4, 20). Numerical studies on biological prostheses usually focus on transcatheter implantation and specific aspects of this intervention type, e.g., the predictability of paravalvular leakage (21). In contrast, this study tries to provide a method capable of estimating the immediate hemodynamic outcome after AVR in a homogenous cohort.

Given their frequent clinical use and the fact that they exhibit a natural orientation during implantation, we decided to focus on surgically implanted, biological aortic valve prostheses. This study aims to provide a method capable of estimating clinically relevant hemodynamic aortic valve parameters in patients receiving surgical AVR with a biological valve prosthesis, using only information available preoperatively. This was done by using preoperative MRI data of the patients to reconstruct the geometry of the aorta and perform virtual AVR. Subsequently, CFD simulations were performed on the virtual AVR geometries and the relevant hemodynamic parameters were computed from the CFD results. The CFD-based hemodynamic parameters were then compared with the same parameters computed from postoperative 4D flow MRI data. We decided to compare CFD against 4D flow MRI instead of echocardiography due to the increased reproducibility and consistency of 4D flow MRI mentioned above.

PATIENTS AND METHODS

The data used in this study was acquired during the SMART study (ClinicalTrials.gov identifier NCT03172338, German Heart Center Berlin, ethics committee approval ID EA2/133/14, 10.12.2015). Written informed consent was obtained from all patients.

Magnetic Resonance Imaging Acquisition

We used data from 10 patients, who underwent surgical AVR at the German Heart Center Berlin. Patient characteristics are summarized in **Table 1**. All patients received a Carpentier-Edwards Perimount Magna Ease aortic valve prosthesis (Edwards Lifesciences, Irvine, USA). Pre- and post-operative anatomical MRI imaging was performed on a 1.5 T Achieva MRI scanner (Philips Medical Systems, Hamburg, Germany) with a typical

TABLE 1 | Patient characteristics.

Characteristic	Median (range) or ratio
Age [years]	64 (57–72)
Sex [female]	3/10
Weight [kg]	95 (70–110)
Height [cm]	182 (164–198)
Body surface area [m^2]	2.19 (1.80–2.42)
Aortic valve stenosis, preoperative	10/10
Aortic valve insufficiency, preoperative	4/10 (all classified as mild)

reconstructed voxel size of $0.80 \times 0.80 \times 2.00$ mm. Anatomical imaging data was obtained during diastole. 4D flow MRI data was reconstructed at a typical voxel size of $2.80 \times 2.25 \times 2.25$ mm with a temporal resolution of 25 phases per cardiac cycle.

Based on the anatomical imaging data, the left ventricular outflow tract (LVOT), the thoracic aorta, and the most proximal parts of the brachiocephalic, left common carotid, and left subclavian artery were manually segmented using ZIBAmira (version 2015.28, Zuse Institute Berlin, Berlin, Germany). Additionally, the nadirs and commissures of the native aortic valve, the ostia and most proximal parts of the coronary arteries, the anterior leaflet of the mitral valve, and the native aortic valve were segmented approximatively to aid orientation during virtual intervention (**Figures 1A,B**).

Computational Fluid Dynamics

Geometries of the Perimount Magna Ease prosthesis and its opened leaflets were kindly provided to us by Claudio Capelli (Institute of Cardiovascular Science, University College London, London, UK). A model of the opened prosthesis was then constructed from the prosthesis frame and leaflet models (**Figure 1C**); the resulting model of the open prosthesis was subsequently scaled to approximate the different sizes offered by the manufacturer (19–29 mm in 2 mm intervals). Virtual interventions consisted of positioning a 3D model of an opened Perimount Magna Ease prosthesis in the preoperative vessel geometry, subsequent intersection of the prosthesis and vessel geometries, and cleanup of the resulting geometry using STAR-CCM+ (version 13.02, Siemens Digital Industries Software, Plano, USA) and MeshLab (version 2016.12, Visual Computing Lab, Istituto di Scienza e Tecnologie dell'Informazione, Pisa, Italy) to produce a manifold and topologically correct surface geometry (**Figure 1D**). Choice of prosthesis size and placement was performed by a cardiac surgeon with experience in surgical AVR. In cases where the prosthesis size virtually implanted by the surgeon was different from the one used during the actual surgery, a second geometry was created using the prosthesis size used during surgery, placed in the same position as the first prosthesis. **Table 2** shows the prosthesis sizes for all patients.

The resulting geometry was then used to perform computational fluid dynamics (CFD) simulations using STAR-CCM+. Peak systolic, stationary boundary conditions were set using 4D flow MRI profiles for the LVOT inlet (**Figure 1E**) and 4D flow MRI flow rates for the descending aorta outlet. **Table 2**

shows inlet flow rates and Reynolds numbers for all patients. Reynolds numbers were calculated at the narrowest part of the prostheses using the rheological model's infinite shear viscosity $\mu_\infty = 0.0035$ Pa·s. Flow profiles were extracted from the 4D flow MRI data with MEVISFlow (version 11.0, Fraunhofer MEVIS, Bremen, Germany). The remainder of the flow was distributed among the branching vessels of the aortic arch using Murray's law and requiring that the brachiocephalic artery receives the same flow rate as the left common carotid and left subclavian artery together. Inlet turbulence intensity was set at 5%, similar to values measured by Isaaz et al. *in vivo* (22). An implicit finite volume solver using a shear stress transport $k-\omega$ turbulence model was used to solve the Navier-Stokes and continuity equations, which describe the flow field. Blood was modeled as a constant density ($1,050\text{ kg/m}^3$) Carreau-Yasuda fluid (zero shear viscosity $\mu_0 = 0.16$ Pa·s, infinite shear viscosity $\mu_\infty = 0.0035$ Pa·s, power constant $n = 0.2128$, transition parameter $a = 0.64$, relaxation parameter $\lambda = 8.2$ s); for a discussion of viscosity models in aortic CFD, refer to Karimi et al. (23). The boundaries of the flow domain, i.e., the aortic wall and the valve prosthesis, were modeled as rigid. Aortic geometries were modeled in their diastolic state. Based on a convergence study, the base mesh size was chosen at 0.5 mm, at and below which mesh resolution did not relevantly influence the evaluated hemodynamic parameters. A blended wall function approach was used for wall treatment. Cell counts varied from 2.85 to 5.09 million per geometry, depending on the physical size of the computational domain. Simulations were performed on a Xeon E5-2630 v4 CPU (Intel, Santa Clara, USA); the modeling workflow took approximately a week per patient, including segmentation, geometry preparation, virtual intervention, and simulation.

Hemodynamic Parameters

Evaluated hemodynamic parameters were v_{max} (maximum flow velocity in the valve jet), dp_{max} (maximum pressure gradient across the aortic valve), SFD (secondary flow degree), and NFD (normalized flow displacement). dp_{max} of 4D flow MRI and CFD data was estimated from v_{max} using the commonly used, strongly simplified version of the Bernoulli equation $dp_{max} = 4 \cdot v_{max}^2$ with the units of v_{max} being m/s and the unit of dp_{max} being mmHg (24). Note that while this estimate and its derivatives are commonly and successfully used in clinical decision making and guidelines, they do not accurately reflect the actual physical pressure drop across the aortic valve. For a discussion of pressure recovery in aortic stenoses and prostheses, refer, for example, to Baumgartner et al. (25) or Dohmen et al. (26). SFD and NFD are scalar parameters calculated from three vessel cross sections, which were placed at the sinotubular junction, directly proximal of the brachiocephalic artery and in the middle between the two previous sections (i.e., in the middle of the ascending aorta). SFD is defined as the mean in-plane velocity divided by the mean through-plane velocity. NFD is defined as the flow displacement normalized by the vessel diameter, with the flow displacement being the distance between the vessel center and the center of the flow. We used the hydraulic vessel diameter (4 times cross-sectional area divided by perimeter) for normalization. We also estimated MRI- and CFD-based IEOA for each patient. EOA was

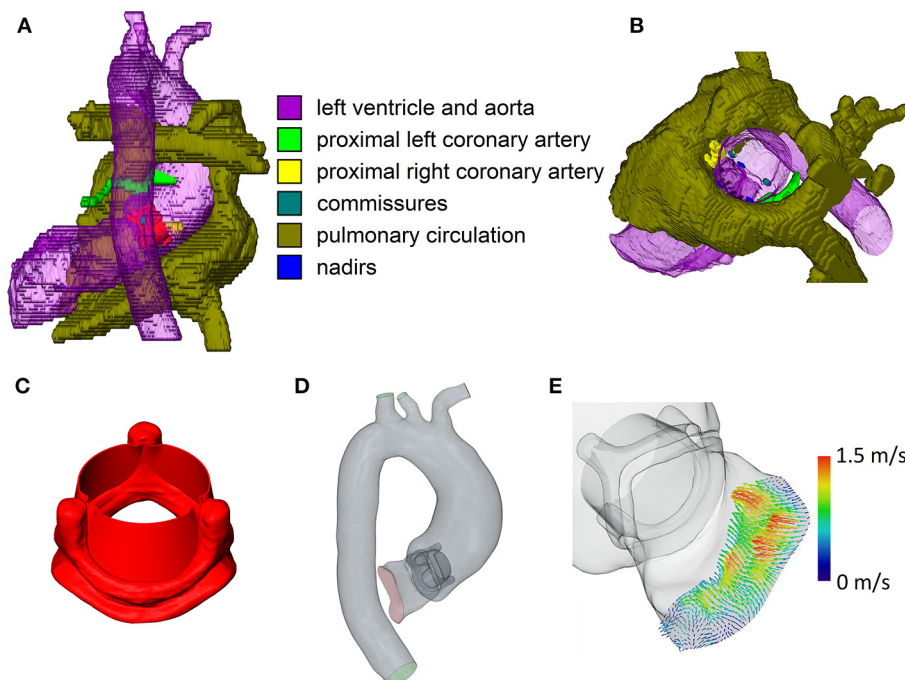


FIGURE 1 | Relevant steps of the virtual intervention process. **(A)** Example of virtual operating field, dorsal view, ascending aorta and aortic arch removed. **(B)** Example of the virtual operating field, oblique view, 3D model of the open 23 mm valve prosthesis. **(D)** Example of the final CFD domain used for simulation. **(E)** 4D flow MRI inlet profile for CFD simulations. Note that the images are not from the same patient.

TABLE 2 | Prosthesis size, peak systolic flow rate, and Reynolds number for all patients.

Patient	Nominal prosthesis size, virtual intervention [mm]	Nominal prosthesis size, actual surgery [mm]	Peak systolic inlet flow rate [ml/s]	Reynolds number at the prosthesis, actual size [-]
I	23	23	354	6,997
II	29	27	430	7,240
III	25	25	394	7,164
IV	25	23	539	10,653
V	25	23	367	7,253
VI	25	23	235	4,645
VII	27	23	407	8,044
VIII	25	21	296	6,407
IX	25	25	412	7,491
X	23	25	464	8,437

estimated using the respective d_{\max} and the EOA equation used by Weese et al. (27). The EOA estimate was then normalized using patient body surface area, to obtain an estimate of IEOA. Additionally, streamlines were calculated to visualize the flows and allow qualitative comparison. Parameters were extracted, calculated, and visualized using MEVISFlow, ZIBAmira and MATLAB (version 2017b, MathWorks, Natick, USA).

Using these hemodynamic parameters, CFD flow fields were compared against postoperative 4D flow MRI data of the patients. To reduce bias, evaluation of v_{\max} and placement of the cross sections used to compute SFD and NFD were done by different authors for the CFD and MRI data. The author analyzing CFD data did not have access to the post-interventional MRI data, and the authors analyzing the post-interventional MRI data did not have access to the CFD data. Note that there are 2 CFD data sets for the cases, for which the prosthesis size chosen during the virtual intervention (index vi) did not match the one used during actual surgery (index as), one for each of the two sizes.

Statistical analysis was performed for v_{\max} , d_{\max} , SFD, NFD, IEOA_{mri}, and IEOA_{as}, using MATLAB. Since only simple linear regression was performed, the unadjusted coefficient of determination R^2 , which in this case is the square of Pearson's r , was used. Estimates of parameters are indicated using the hat operator, e.g., \hat{v}_{\max} . Where specified, the use of median and interquartile range as measures of central tendency and dispersion was based on inspection of histograms of the underlying data.

RESULTS

In order to identify the hemodynamic results, the following indices are used: mri for the results derived from postoperative 4D flow MRI, vi for the results of the CFD simulations using the prosthesis size determined by the surgeon during virtual intervention, and as for the results of the CFD simulations using

TABLE 3 | 4D flow MRI- and CFD-based estimated indexed effective orifice areas (IEOA) for all patients.

Patient	Estimated IEOA _{mri} [cm ² /m ²]	Estimated IEOA _{as} [cm ² /m ²]
I	0.74	1.07
II	0.73	1.14
III	0.59	0.85
IV	0.62	0.80
V	0.91	1.10
VI	0.84	0.96
VII	0.66	0.87
VIII	0.70	0.96
IX	1.00	1.11
X	0.76	0.92

the prosthesis size used during the actual surgery performed on the patient. Given the number of patients, we decided to follow a descriptive statistics approach.

Choice of Prosthesis Size and IEOA

Table 2 summarizes the prosthesis sizes used during virtual interventions and actual surgeries, while **Table 3** shows estimated IEOA_{as} for the actual size CFD simulations and IEOA_{mri} for the postoperative 4D flow MRI data. We also calculated the coefficient of determination for linear regression between IEOA_{as} and IEOA_{mri}, which was $R^2 = 0.52$. For three patients, the prosthesis sizes chosen during virtual intervention and actual surgery were identical. The mean absolute error between the prosthesis size chosen during virtual intervention and the prosthesis size actually used was 1.8 mm with the virtual interventions using a larger prosthesis size on average.

Pressure Gradients and Maximum Velocities

Figure 2 shows scatter and linear regression plots for v_{max} and dp_{max}. Coefficient of determination (R^2), root mean square error (RMSE), and regression equation for v_{max,mri} vs. v_{max,vi} were $R^2 = 0.69$, RMSE = 0.24 m/s, and $\hat{v}_{max,mri} = 0.8478 \cdot v_{max,vi} + 0.7887$ m/s, while they were $R^2 = 0.75$, RMSE = 0.21 m/s, and $\hat{v}_{max,mri} = 0.9073 \cdot v_{max,as} + 0.5787$ m/s for v_{max,mri} vs. v_{max,as}. Median values (interquartile range) of v_{max} were 2.1 m/s (0.3 m/s), 1.7 m/s (0.6 m/s), and 1.7 m/s (0.4 m/s) for v_{max,mri}, v_{max,vi}, and v_{max,as}, respectively. Similarly, the statistics were $R^2 = 0.73$, RMSE = 4.5 mmHg, and $\hat{dp}_{max,mri} = 1.227 \cdot dp_{max,vi} + 5.601$ mmHg for dp_{max,mri} vs. dp_{max,vi}, with $R^2 = 0.81$, RMSE = 3.8 mmHg, and $\hat{dp}_{max,mri} = 1.175 \cdot dp_{max,as} + 4.281$ mmHg for dp_{max,mri} vs. dp_{max,as}. Median values (interquartile range) of dp_{max} were 18 mmHg (5 mmHg), 11 mmHg (8 mmHg), and 12 mmHg (6 mmHg) for dp_{max,mri}, dp_{max,vi}, and dp_{max,as}, respectively.

Quantitative Description of Hemodynamics

Linear regression results for SFD and NFD are shown in **Table 4**; the coefficients of determination for SFD and NFD were generally lower than for v_{max} and dp_{max}. Median values (interquartile range) of SFD over all cross sections were 0.70 (0.57), 0.88

(0.56), and 0.95 (0.51) for SFD_{mri}, SFD_{vi}, and SFD_{as}, respectively. Median values (interquartile range) of NFD over all cross sections were 0.072 (0.090), 0.148 (0.066), and 0.155 (0.062) for NFD_{mri}, NFD_{vi}, and NFD_{as}, respectively. Additionally, **Table 4** shows median values and interquartile ranges of SFD and NFD for each cross section individually. **Figure 2** contains scatter and linear regression plots for SFD and NFD, color- and marker-coded by cross-section location.

Qualitative Description of Hemodynamics

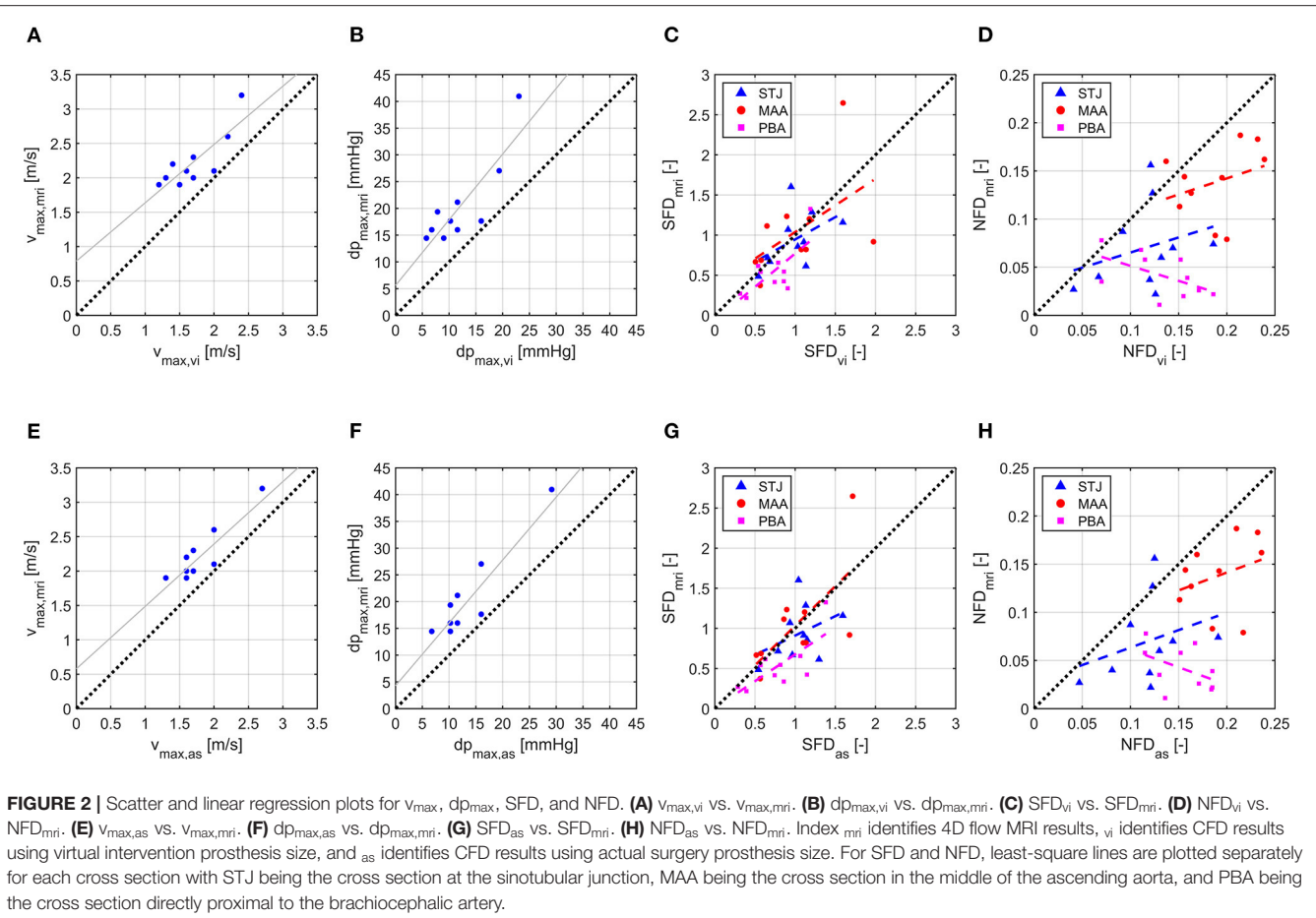
For hemodynamic visualization, **Figure 3** shows streamlines for all patients. For most patients, the MRI- and CFD-based flow fields agree well, with the main flow features and velocities being comparable. In general, the locations of regions with very low velocities close to stagnation are very similar between both methods. In several patients, these regions are located close to the concave curvature of the ascending aorta (e.g., patients III, VI, VII, and VIII). In patient III, a similar region is identified in the descending aorta by both methods. The orientation of the jet passing through the valve prosthesis, and thus the orientation of the valve prosthesis itself, is also comparable between both methods. Only in patients I and III can a slight deviation between the simulation using the actual size and the MRI measurements be observed.

However, some relevant deviations between measured and calculated hemodynamics can be found. In patient VI, a flow acceleration in the proximal descending aorta is observed in the MRI data. This flow feature is not nearly as pronounced in the CFD data, even though the vessel contours agree well in that region. In the MRI data of patient II, high velocities are observed immediately downstream of the valve prosthesis with a subsequent strong deceleration proximal to the aortic arch. This flow pattern is not found in the CFD data.

The simulations using prosthesis sizes chosen during virtual intervention (CFD_{vi}) tend to show lower flow velocities than the simulations using prosthesis sizes chosen during actual surgery (CFD_{as}). The visualization also shows that flow patterns are quite similar between CFD_{vi} and CFD_{as}.

DISCUSSION

R^2 and RMSE indicate good agreement between MRI- and CFD-based values of v_{max} and dp_{max}. This suggests that postoperative maximum pressure gradients and velocities can be estimated reasonably well using the current CFD model. The correlation between MRI-based and CFD-based values was generally stronger for the simulations using the actual prosthesis size over the simulations using the prosthesis size chosen during virtual intervention. As the virtual intervention prosthesis sizes were, on average, off by about one size, this observation can most likely be attributed to the mismatch between actual and virtual prosthesis size. Simulations using the prosthesis size chosen during virtual intervention tend to show lower flow velocities, which seems plausible given their, on average, larger orifice areas. The difference in prosthesis size is likely caused by the virtual intervention providing no sizing mechanism similar to the use of a sizing instrument during actual surgeries. This seems to



lead to overestimation of the space available for implantation. Furthermore, the suture ring may *in vivo* assume a shape different from the 3D prosthesis model. In practice, the issue of correctly predicting prosthesis size could easily be overcome by being mindful of the tendency to overestimate prosthesis size as well as by performing simulations with multiple possible prosthesis sizes ahead of surgery. This would ensure that the surgeon would preoperatively have CFD results available for all plausible sizes, effectively removing the problem of having to choose the correct prosthesis size.

The underestimation of v_{\max} and dp_{\max} by CFD might partially be caused by the CFD simulations being based on preoperative MRI profiles. After valve replacement, peak systolic flow likely increases due to reduced valvular resistance, which in turn might explain the relatively higher v_{\max} and dp_{\max} in the MRI data. Additionally, postoperative prosthesis opening might be subtotal compared to the idealized, fully open prosthesis model used for CFD, resulting in higher v_{\max} and dp_{\max} .

IEOA_{mri} and IEOA_{as} were moderately correlated, indicating that the predicting postoperative IEOA still poses some challenge. While IEOA is a relevant factor, current recommendations also emphasize the importance of flow velocity and pressure gradient in assessing hemodynamic prosthesis performance (28). These parameters exhibit fairly low RMSE of 0.21 m/s and 3.8 mmHg,

respectively. By considering all parameters together, one should therefore be able to arrive at a reasonably accurate estimate of postoperative prosthesis performance.

While good agreement between real and virtual intervention was observed for the pressure gradient and the maximum velocity, SFD and NFD featured lower R^2 and worse RMSE. The latter parameters describe the spatially resolved hemodynamics. Even though 4D flow MRI and the velocity information calculated using CFD were registered, to ensure identical orientation of the evaluation cross sections used for both data sets, minor deviations might still be present. Furthermore, SFD and NFD are likely more susceptible to the segmentation of the patient-specific geometry as well as the orientation of the valve prosthesis. Especially the latter parameter will directly affect NFD, as the orientation of the valve prosthesis will directly affect the orientation of its jet-like outflow. As only preoperative information was used for the virtual intervention, the orientation of the virtual and real prosthesis might differ. There might also be some differences between pre- and postoperative anatomies, which could have an influence on SFD/NFD. While we focused on patients receiving isolated AVR, there might still be small anatomical changes associated with surgery and MRI image acquisition, e.g., due to sutures, mobilization of anatomical structures, the prosthesis itself, or subtly different patient posture

TABLE 4 | Median value, interquartile range (IQR), and linear regression for SFD and NFD.

Parameter	Median (IQR) for mri	Median (IQR) for vi	Median (IQR) for as	R ² mri vs. vi	R ² mri vs. as	RMSE mri vs. vi	RMSE mri vs. as
SFD all cross sections	0.70 (0.57)	0.88 (0.56)	0.95 (0.51)	0.38	0.44	0.39	0.37
SFD sinotubular junction	0.89 (0.49)	0.99 (0.45)	1.08 (0.21)	0.25	0.16	0.32	0.33
SFD middle of ascending aorta	0.87 (0.52)	0.99 (0.60)	1.00 (0.56)	0.27	0.46	0.56	0.48
SFD proximal to brachiocephalic artery	0.48 (0.28)	0.77 (0.32)	0.78 (0.49)	0.49	0.53	0.24	0.23
NFD all cross sections	0.072 (0.09)	0.148 (0.066)	0.155 (0.062)	0.23	0.20	0.048	0.049
NFD sinotubular junction	0.065 (0.05)	0.122 (0.040)	0.122 (0.030)	0.08	0.10	0.044	0.044
NFD middle of ascending aorta	0.144 (0.049)	0.192 (0.058)	0.189 (0.054)	0.10	0.10	0.038	0.038
NFD proximal to brachiocephalic artery	0.037 (0.036)	0.141 (0.048)	0.160 (0.054)	0.30	0.20	0.020	0.021

Index *mri* identifies 4D flow MRI results, *vi* identifies CFD results using virtual intervention prosthesis size, and *as* identifies CFD results using actual surgery prosthesis size. Coefficients of determination (R^2) and root mean square error (RMSE) are for linear regression between MRI- and CFD-based values; all regressions use the CFD-based values as the independent variable.

during postoperative MRI. Another factor possibly influencing SFD and NFD calculation is the use of a RANS-based turbulence model to keep computation time reasonable. RANS-based turbulence models cannot capture all temporal and spatial scales of the flow, which may lead to subtle differences in SFD and NFD. Additionally, the 4D flow MRI resolution was significantly lower than the resolution of the CFD mesh, meaning that some flow scales included in the calculation of CFD-based SFD/NFD might not have been included in the calculation of MRI-based SFD/NFD. Finally, the inlet velocity profiles were measured before AVR and they might subsequently change. It has been shown that the inlet profile can affect the flow distal to the valve prosthesis (6).

Another point regarding NFD is that it has previously been shown to correlate with aortic dilation in patients with high NFD values secondary to strongly eccentric flow, in turn caused by bicuspid aortic valve morphology (7, 8). Burris et al. found an NFD cutoff value of 0.2, above which the aortic growth rate increased significantly in their study (8). Such high values of NFD did rarely occur in our patients, likely due to them receiving the prostheses as well as none of them exhibiting relevant ascending aorta dilation. It is therefore conceivable that the correlation between MRI- and CFD-based NFD would be stronger in patients with higher NFD, in whom constant modeling errors would be relatively smaller.

The MRI- and CFD-based streamlines are quite similar for most patients. In most cases, relevant flow features, such as recirculation zones and the location of prosthesis jet impingement on the aortic wall, were comparable. Velocity magnitudes were mostly similar. The existing small differences could have potentially been caused by segmentation differences, subtly different prosthesis placement, and inertial effects.

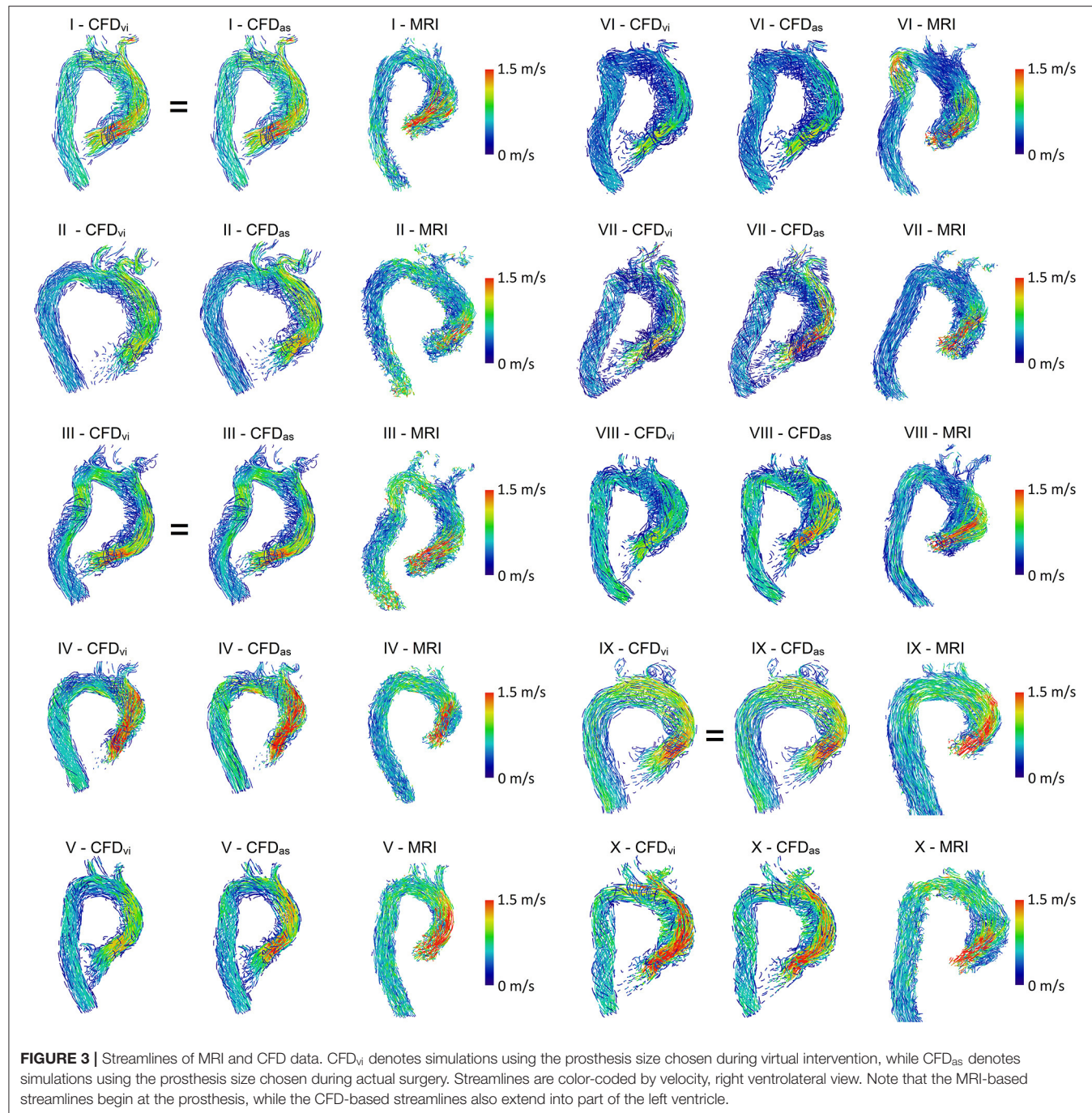
The present study demonstrates a method to estimate postoperative hemodynamic parameters after AVR using only preoperative data. Unlike more complex CFD models, which may include unsteady FSI simulations of prosthesis hemodynamics (19, 20), the approach presented in this study uses a less complex model, including rigid walls and stationary boundary conditions. While this means that hemodynamic parameters

cannot be evaluated in a time-resolved manner and also neglects dynamic effects, it reduces modeling and computation time and avoids having to estimate unknown elastic properties of the aorta and valve prosthesis. The present method is less well-suited for understanding complex flow phenomena and does not allow analysis of certain features, such as valve prosthesis opening and closing. The workflow can, however, be performed in a clinically reasonable time frame and offers good robustness, which is important for clinical applicability and direct comparison against postoperative 4D flow MRI data. Novel aspects of the present study include the model being solely based on preoperative data, its results being directly compared to postoperative 4D flow MRI data and the virtual intervention being performed by a cardiac surgeon with experience in AVR.

Limitations

The model used in this study uses a quasi-steady approach to predict the peak systolic hemodynamics after AVR. The aorta and the leaflets of the aortic valve prosthesis were modeled as rigid. Additionally, to evaluate the predictive capabilities of this model, only patient data acquired before AVR was used. These limitations might partially explain the weak-to-moderate correlations of SFD and NFD. For example, replacement of the diseased valve might affect myocardial function and thus the LVOT flow profile as well as peak systolic flow rates. Additionally, the surgical implantation will result in small changes to the anatomy of the ascending aorta. There are currently no models to predict either the change in ventricular hemodynamics or the postoperative anatomy. However, the changes in anatomy seem to be limited, as the vessel contours of the ascending aorta in agree well in all cases.

While simulation of the dynamic behavior of aortic valve prostheses is technically feasible, such simulations not only are associated with higher computational costs but also require estimation of patient-specific material properties. Furthermore, either the transient LVOT inflow profile must be measured, or the left ventricular contraction must be modeled. All these steps



introduce additional uncertainty due to model assumptions and additional measurements.

CONCLUSION

The results demonstrate that, using the approach presented in this study, MRI-based maximum pressure gradients and velocities across biological aortic valve prostheses can be

estimated reasonably well from CFD simulations based only on preoperative MRI and clinical patient data. The approach could potentially be used to identify which prosthesis sizes are likely to put individual patients at risk of increased postoperative pressure gradient ahead of surgery and to estimate postoperative prosthesis performance. The workflow is comparatively inexpensive computationally and can be performed within a clinically reasonable time frame. Regarding

novel and sensitive hemodynamic parameters like SFD or NFD, further work needs to be undertaken to accurately estimate them in the patient collective described here.

DATA AVAILABILITY STATEMENT

The raw data supporting the conclusions of this article will be made available by the authors, without undue reservation.

ETHICS STATEMENT

The studies involving human participants were reviewed and approved by Ethikkommission, Charité - Universitätsmedizin Berlin. The patients/participants provided their written informed consent to participate in this study.

AUTHOR CONTRIBUTIONS

All roles according to CRediT (contributor roles taxonomy). FH, SN, LG, and TK: conceptualization. FH, JB, LG, MS, and

SN: formal analysis. TK, LG, and SN: funding acquisition. SN, SS, FH, LJ, and JB: investigation. FH, SN, JB, and SS: methodology. LG, TK, and SN: supervision. FH and MS: visualization. FH, LG, JB, and SN: writing—original draft. SS, LJ, MS, and TK: writing—review and editing. All authors contributed to the article and approved the submitted version.

FUNDING

This work was supported by the German Federal Ministry of Education and Research (BMBF, grant ID: 031A427A). We acknowledge support from the German Research Foundation (DFG) and the Open Access Publication Fund of Charité - Universitätsmedizin Berlin.

ACKNOWLEDGMENTS

The authors would like to thank Claudio Capelli (Institute of Cardiovascular Science, University College London, London, UK) for providing 3D models of the valve prosthesis and its leaflets.

REFERENCES

- Beckmann A, Meyer R, Lewandowski J, Markewitz A, Harringer W. German heart surgery report 2018: the annual updated registry of the German society for thoracic and cardiovascular surgery. *Thorac Cardiovasc Surg.* (2019) 67:331–44. doi: 10.1055/s-0039-1693022
- Fallon JM, DeSimone JP, Brennan JM, O'Brien S, Thibault DP, DiScipio AW, et al. The incidence and consequence of prosthesis-patient mismatch after surgical aortic valve replacement. *Ann Thorac Surg.* (2018) 106:14–22. doi: 10.1016/j.athoracsur.2018.01.090
- Bilkhu R, Jahangiri M, Otto CM. Patient-prosthesis mismatch following aortic valve replacement. *Heart.* (2019) 105:s28–33. doi: 10.1136/heartjnl-2018-313515
- Hellmeier F, Nordmeyer S, Yevtushenko P, Bruening J, Berger F, Kuehne T. Hemodynamic evaluation of a biological and mechanical aortic valve prosthesis using patient-specific MRI-based CFD. *Artif Organs.* (2018) 42:49–57. doi: 10.1111/aor.12955
- Schubert C, Brüning J, Goubergrits L, Hennemuth A, Berger F, Kühne T, et al. Assessment of hemodynamic responses to exercise in aortic coarctation using MRI-ergometry in combination with computational fluid dynamics. *Sci Rep.* (2020) 10:18894. doi: 10.1038/s41598-020-75689-z
- Goubergrits L, Mevert R, Yevtushenko P, Schaller J, Kertzscher U, Meier S, et al. The impact of MRI-based inflow for the hemodynamic evaluation of aortic coarctation. *Ann Biomed Eng.* (2013) 41:2575–87. doi: 10.1007/s10439-013-0879-2
- Hope MD, Sigovan M, Wrenn SJ, Saloner D, Dyverfeldt P. MRI hemodynamic markers of progressive bicuspid aortic valve-related aortic disease. *J Magn Reson Imaging.* (2014) 40:140–5. doi: 10.1002/jmri.24362
- Burris NS, Sigovan M, Knauer HA, Tseng EE, Saloner D, Hope MD. Systolic flow displacement correlates with future ascending aortic growth in patients with bicuspid aortic valves undergoing magnetic resonance surveillance. *Invest Radiol.* (2014) 49:635–9. doi: 10.1097/RLI.0000000000000064
- Garcia J, Barker AJ, Murphy I, Jarvis K, Schnell S, Collins JD, et al. Four-dimensional flow magnetic resonance imaging-based characterization of aortic morphometry and haemodynamics: impact of age, aortic diameter, and valve morphology. *Eur Heart J Cardiovasc Imaging.* (2016) 17:877–84. doi: 10.1093/eihci/jev228
- von Knobelsdorff-Brenkenhoff F, Karunaharamoorthy A, Trauzedel RF, Barker AJ, Blaszczyk, Markl M, et al. Evaluation of aortic blood flow and wall shear stress in aortic stenosis and its association with left ventricular remodeling. *Circ Cardiovasc Imaging.* (2016) 9:e004038. doi: 10.1161/CIRCIMAGING.115.004038
- Sigovan M, Hope MD, Dyverfeldt P, Saloner D. Comparison of four-dimensional flow parameters for quantification of flow eccentricity in the ascending aorta. *J Magn Reson Imaging.* (2011) 34:1226–30. doi: 10.1002/jmri.22800
- Adriaans BP, Westenberg JJM, van Cauteren YJM, Gerretsen S, Elbaz MSM, Bekkers SCAM, et al. Clinical assessment of aortic valve stenosis: comparison between 4D flow MRI and transthoracic echocardiography. *J Magn Reson Imaging.* (2020) 51:472–80. doi: 10.1002/jmri.26847
- Morris PD, Narracott A, von Tengg-Kobligk H, Soto DAS, Hsiao S, Lungu A, et al. Computational fluid dynamics modelling in cardiovascular medicine. *Heart.* (2016) 102:18–28 doi: 10.1136/heartjnl-2015-308044
- Itatani K, Miyazaki S, Furusawa T, Numata S, Yamazaki S, Morimoto K, et al. New imaging tools in cardiovascular medicine: computational fluid dynamics and 4D flow MRI. *Gen Thorac Cardiovasc Surg.* (2017) 65:611–21. doi: 10.1007/s11748-017-0834-5
- Murayama Y, Fujimura S, Suzuki T, Takao H. Computational fluid dynamics as a risk assessment tool for aneurysm rupture. *Neurosurg Focus.* (2019) 47:E12. doi: 10.3171/2019.4.FOCUS19189
- Morris PD, Ryan D, Morton AC, Lycett R, Lawford PV, Hose DR, et al. Virtual fractional flow reserve from coronary angiography: modeling the significance of coronary lesions: results from the VIRTU-1 (VIRTUAl Fractional Flow Reserve From Coronary Angiography) study. *JACC Cardiovasc Imaging.* (2013) 6:149–57. doi: 10.1016/j.jcin.2012.08.024
- Nørgaard BL, Leipsis J, Gaur S, Seneviratne S, Ko BS, Ito H, et al. Diagnostic performance of noninvasive fractional flow reserve derived from coronary computed tomography angiography in suspected coronary artery disease: the NXT trial (Analysis of Coronary Blood Flow Using CT Angiography: Next Steps). *J Am Coll Cardiol.* (2014) 63:1145–55. doi: 10.1016/j.jacc.2013.11.043
- Kaminsky R, Dumont K, Weber H, Schroll M, Verdonck P. PIV validation of blood-heart valve leaflet interaction modelling. *Int J Artif Organs.* (2007) 30:640–8. doi: 10.1177/039139880703000712
- Luraghi G, Wu W, De Gaetano F, Matas JFR, Moggridge GD, Serrani M, et al. Evaluation of an aortic valve prosthesis: fluid-structure interaction or structural simulation? *J Biomech.* (2017) 58:45–51. doi: 10.1016/j.jbiomech.2017.04.004

20. Dumont K, Vierendeels J, Kaminsky R, van Nooten G, Verdonck P, Bluestein D. Comparison of the hemodynamic and thrombogenic performance of two bileaflet mechanical heart valves using a CFD/FSI model. *J Biomech Eng.* (2007) 129:558–65. doi: 10.1115/1.2746378
21. Bianchi M, Marom G, Ghosh RP, Rotman OM, Parikh P, Gruberg L, et al. Patient-specific simulation of transcatheter aortic valve replacement: impact of deployment options on paravalvular leakage. *Biomech Model Mechanobiol.* (2019) 18:435–51. doi: 10.1007/s10237-018-1094-8
22. Isaaz K, Bruntz JF, Da Costa A, Winninger D, Cerisier A, de Chillou C, et al. Noninvasive quantitation of blood flow turbulence in patients with aortic valve disease using online digital computer analysis of Doppler velocity data. *J Am Soc Echocardiogr.* (2003) 16:965–74. doi: 10.1016/S0894-7317(03)00420-6
23. Karimi S, Dabagh M, Vasava P, Dadvar M, Dabir B, Jalali P. Effect of rheological models on the hemodynamics within human aorta: CFD study on CT image-based geometry. *J Non-Newton Fluid.* (2014) 207:42–52. doi: 10.1016/j.jnnfm.2014.03.007
24. Hatle L, Angelsen BA, Tromsdal A. Non-invasive assessment of aortic stenosis by Doppler ultrasound. *Br Heart J.* (1980) 43:284–92. doi: 10.1136/hrt.43.3.284
25. Baumgartner H, Stefenelli T, Niederberger J, Schima H, Maurer G. “Overestimation” of catheter gradients by Doppler ultrasound in patients with aortic stenosis: a predictable manifestation of pressure recovery. *J Am Coll Cardiol.* (1999) 33:1655–61. doi: 10.1016/S0735-1097(99)00066-2
26. Dohmen G, Schmitz C, Steinseifer U, Hatam N, Hilgers RD, Autschbach R, et al. Influence of aortic dimensions on the hemodynamic performance of small aortic valve prostheses: impact on patient/prosthesis mismatch. *Thorac Cardiovasc Surg.* (2011) 59:449–53. doi: 10.1055/s-0030-1271012
27. Weese J, Lungu A, Peters J, Weber FM, Waechter-Stehle I, Hose DR. CFD- and Bernoulli-based pressure drop estimates: a comparison using patient anatomies from heart and aortic valve segmentation of CT images. *Med Phys.* (2017) 44:2281–92. doi: 10.1002/mp.12203
28. Lancellotti P, Pibarot P, Chambers J, Edvardsen T, Delgado V, Dulgheru R, et al. Recommendations for the imaging assessment of prosthetic heart valves: a report from the European Association of Cardiovascular Imaging endorsed by the Chinese Society of Echocardiography, the Inter-American Society of Echocardiography, and the Brazilian Department of Cardiovascular Imaging. *Eur Heart J Cardiovasc Imaging.* (2016) 17:589–90. doi: 10.1093/eihci/jew025

Conflict of Interest: The authors declare that the research was conducted in the absence of any commercial or financial relationships that could be construed as a potential conflict of interest.

Copyright © 2021 Hellmeier, Brünning, Sündermann, Jarmatz, Schafstedde, Goubergrits, Kühne and Nordmeyer. This is an open-access article distributed under the terms of the Creative Commons Attribution License (CC BY). The use, distribution or reproduction in other forums is permitted, provided the original author(s) and the copyright owner(s) are credited and that the original publication in this journal is cited, in accordance with accepted academic practice. No use, distribution or reproduction is permitted which does not comply with these terms.

3.2 Validierung der patientenspezifischen virtuellen Therapieplanung gegen den klinischen Goldstandard

Mit dem Ziel, die virtuelle, hämodynamische Modellierung zu validieren, erfolgte sodann ein Vergleich zwischen dem Goldstandard der klinischen Druckmessung (der invasiven Herzkatheterdiagnostik) und dem bildbasierten Simulationsverfahren. Dieser wurde an 84 Patient*innen mit Aortenstenose durchgeführt, die vor einer geplanten Transkatheter Aortenklappenimplantation (TAVI) eine CT-Bildgebung sowie eine diagnostische Herzkatheteruntersuchung erhielten.

Computed Tomography-Based Assessment of Transvalvular Pressure Gradient in Aortic Stenosis

Benedikt Franke, Jan Brüning, Pavlo Yevtushenko, Henryk Dreger, Anna Brand, Benjamin Juri, Axel Unbehaun, Jörg Kempfert, Simon Sündermann, Alexander Lembcke, Natlia Solowjowa, Sebastian Kelle, Volkmar Falk, Titus Kühne, Leonid Goubergrits, **Marie Schafstedde**

Der nachfolgende Text entspricht inhaltlich dem Abstrakt der oben genannten Publikation als Übersetzung durch die Autorin:

*„Bei Patient*innen mit Aortenklappenstenose (AS) liefert die kardiale Computertomographie (CT) für die Behandlungsplanung wichtige Informationen über die kardiovaskuläre Anatomie, nicht jedoch über relevante hämodynamische Parameter wie zum Beispiel den transvalvulären Druckgradienten (TPG).*

*Ziel dieser Studie ist die Validierung eines Modells reduzierter Ordnung zur bildbasierten Vorhersage des TPGs bei Patient*innen mit AS.*

*Mittels eines Modells reduzierter Ordnung wurde der TPG auf Grundlage des präoperativ durchgeführten CTs berechnet. Gefüttert wurde das Modell mit Informationen über den patientenspezifischen spitzensystolischen Volumenstrom sowie die Aortenklappenöffnungsfläche. Letztere wurde durch Segmentierung der Aortenklappensegel bestimmt, während der Volumenstrom auf Grundlage einer volumetrischen Segmentierung des linken Ventrikels quantifiziert wurde. Zur Validierung wurden invasive Herzkatheterdruckmessungen aus dem linken Ventrikel und der Aorta Ascendens herangezogen. Insgesamt wurden 84 Datensätze von Patient*innen mit AS verwendet, um den CT-basierten TPG mit dem Katheter-basierten TPG zu vergleichen.*

Der CT-basierte TPG und der Katheter-basierte TPG lagen bei 48.0 ± 26 mmHg bzw. 50.6 ± 28.0 ($p=0.56$). Mittels Bland-Altman-Analyse konnte eine gute Übereinstimmung zwischen beiden

Methoden mit einem mittleren Unterschied im TPG von 2.6 mmHg und einer Standardabweichung von 19.3 mmHg gezeigt werden. Beide Methoden zeigten eine gute Korrelation mit r=0.72 (p<0.001).

*Die in dieser Studie vorgestellte Methode ermöglicht die bildbasierte Bestimmung des TPG bei Patient*innen mit AS und erweitert somit die derzeitigen Möglichkeiten der kardialen CT für die patientenspezifische Diagnostik und Behandlungsplanung.“*



Computed Tomography-Based Assessment of Transvalvular Pressure Gradient in Aortic Stenosis

Benedikt Franke^{1†}, Jan Brüning^{1†}, Pavlo Yevtushenko¹, Henryk Dreger^{2,3}, Anna Brand^{2,3}, Benjamin Juri³, Axel Unbehaun^{2,4}, Jörg Kempfert⁴, Simon Sündermann^{3,4}, Alexander Lembcke⁵, Natalia Solowjowa⁴, Sebastian Kelle⁶, Volkmar Falk⁴, Titus Kuehne^{1,2,7}, Leonid Goubergrits^{1,8} and Marie Schafstedde^{1,2,7,9*}

OPEN ACCESS

Edited by:

Grigoris Korosoglou,
GRN Klinik Weinheim, Germany

Reviewed by:

Sorin Giusca,
GRN Klinik Weinheim, Germany
Christin Tesche,
Medical University of South Carolina,
United States

*Correspondence:

Marie Schafstedde
schafstedde@dhzb.de

[†]These authors have contributed
equally to this work and share first
authorship

Specialty section:

This article was submitted to
Cardiovascular Imaging,
a section of the journal
Frontiers in Cardiovascular Medicine

Received: 07 May 2021

Accepted: 09 July 2021

Published: 08 September 2021

Citation:

Franke B, Brüning J, Yevtushenko P,
Dreger H, Brand A, Juri B,
Unbehaun A, Kempfert J,
Sündermann S, Lembcke A,
Solowjowa N, Kelle S, Falk V,
Kuehne T, Goubergrits L and
Schafstedde M (2021) Computed
Tomography-Based Assessment of
Transvalvular Pressure Gradient in
Aortic Stenosis.

Front. Cardiovasc. Med. 8:706628.
doi: 10.3389/fcvm.2021.706628

Background: In patients with aortic stenosis, computed tomography (CT) provides important information about cardiovascular anatomy for treatment planning but is limited in determining relevant hemodynamic parameters such as the transvalvular pressure gradient (TPG).

Purpose: In the present study, we aimed to validate a reduced-order model method for assessing TPG in aortic stenosis using CT data.

Methods: TPG_{CT} was calculated using a reduced-order model requiring the patient-specific peak-systolic aortic flow rate (Q) and the aortic valve area (AVA). AVA was determined by segmentation of the aortic valve leaflets, whereas Q was quantified based on volumetric assessment of the left ventricle. For validation, invasively measured TPG_{catheter} was calculated from pressure measurements in the left ventricle and the ascending aorta. Altogether, 84 data sets of patients with aortic stenosis were used to compare TPG_{CT} against TPG_{catheter}.

Results: TPG_{catheter} and TPG_{CT} were 50.6 ± 28.0 and 48.0 ± 26 mmHg, respectively ($p = 0.56$). A Bland–Altman analysis revealed good agreement between both methods with a mean difference in TPG of 2.6 mmHg and a standard deviation of 19.3 mmHg. Both methods showed good correlation with $r = 0.72$ ($p < 0.001$).

Conclusions: The presented CT-based method allows assessment of TPG in patients with aortic stenosis, extending the current capabilities of cardiac CT for diagnosis and treatment planning.

Keywords: cardiac computed tomography, aortic stenosis, transvalvular pressure gradient, image-based modeling, reduced order model

INTRODUCTION

Aortic valve stenosis (AS) is the most common heart valve disease requiring surgery or intervention (1). In the aging population, the incidence of AS is increasing, reaching a prevalence of 12% in the population over 75 years of age (2). Patients with mild-to-moderate stenosis often remain symptom-free for a long period of time. However, mortality increases rapidly with the onset of symptoms (3). According to current guidelines, grading of AS severity is primarily based on the maximum flow velocity across the aortic valve, which is used for calculation of the transvalvular pressure gradient (TPG) and the aortic valve area (AVA) (4, 5).

CT became indispensable for planning of surgical or transcatheter aortic valve implantation (TAVI). This includes the assessment of anatomic structures, like the aortic annulus, the coronary ostia, and diameters and curvatures of all vessels from the catheter's entry side to the aortic valve. Moreover, CT contributes to the evaluation of AS severity by measurement of AVA (6, 7) as well as aortic valve calcium scoring in low-flow low-gradient AS (5, 8, 9). However, measurements of functional hemodynamic parameters, for example, TPG, that allow assessment of AS severity are not yet possible. Such functional measurements, which are currently only possible using echocardiography or cardiac catheterization, would improve the diagnostic value of CT in terms of a unified diagnostic tool.

The objective of this study is to introduce a method for TPG assessment using patient-specific aortic flow rates (Q) and AVA, both measured from cardiac CT images only. To validate this CT-based method, calculated TPG will be compared with catheter-based measurements.

METHODS

For this study, retrospective data of patients with AS treated with TAVI in two different centers between February 2019 and October 2020 were used. The following inclusion criteria were defined: aortic stenosis patients who were treated using TAVI; temporally resolved CT images were acquired for TAVI planning; and blood pressures in the left ventricle and the ascending aorta were invasively measured using catheterization during the TAVI procedure but before implantation of the device. No additional exclusion criteria were defined.

The study was registered at ClinicalTrials.gov (NCT04600739) and was approved by the institutional review board (IRB) (EA2/174/19). Individual informed consent was waived by the IRB due to the retrospective nature of this study.

CT Image Acquisition

CT data sets of the entire heart were acquired as part of TAVI planning to assist in the choice of size and type of prosthesis. The median time between CT imaging and TAVI procedure was 12 (1–148) days. Following intravenous contrast material injection, an electrocardiogram-synchronized scan was performed using either a dual-source multislice spiral CT scanner (Somatom Definition Flash, Siemens Healthcare, Erlangen, Germany) or a wide area-detector volume CT scanner (Aquilion One Vision,

Canon Medical Systems, or Revolution CT, GE Healthcare, Chicago, IL, USA). All scanning was performed at a tube voltage of 100 kV and an individually adapted tube current using the scanner exposure control software. For each subject, a multiphase data set was reconstructed that allows exact identification of the systolic phase with the widest aortic valve opening. All images were reconstructed with a standard soft-tissue convolution kernel and with the use of a dedicated noise-reduction software. Spatial and temporal resolution of the CT images varied. The spatial resolution used for segmentation was $(0.39 - 0.648 \text{ mm}) \times (0.39 - 0.648 \text{ mm})$ in-plane resolution and $(0.5 - 1 \text{ mm})$ slice thickness. The temporal resolution ranged from 70 to 140 ms.

Measurement of Invasive Pressure Gradients

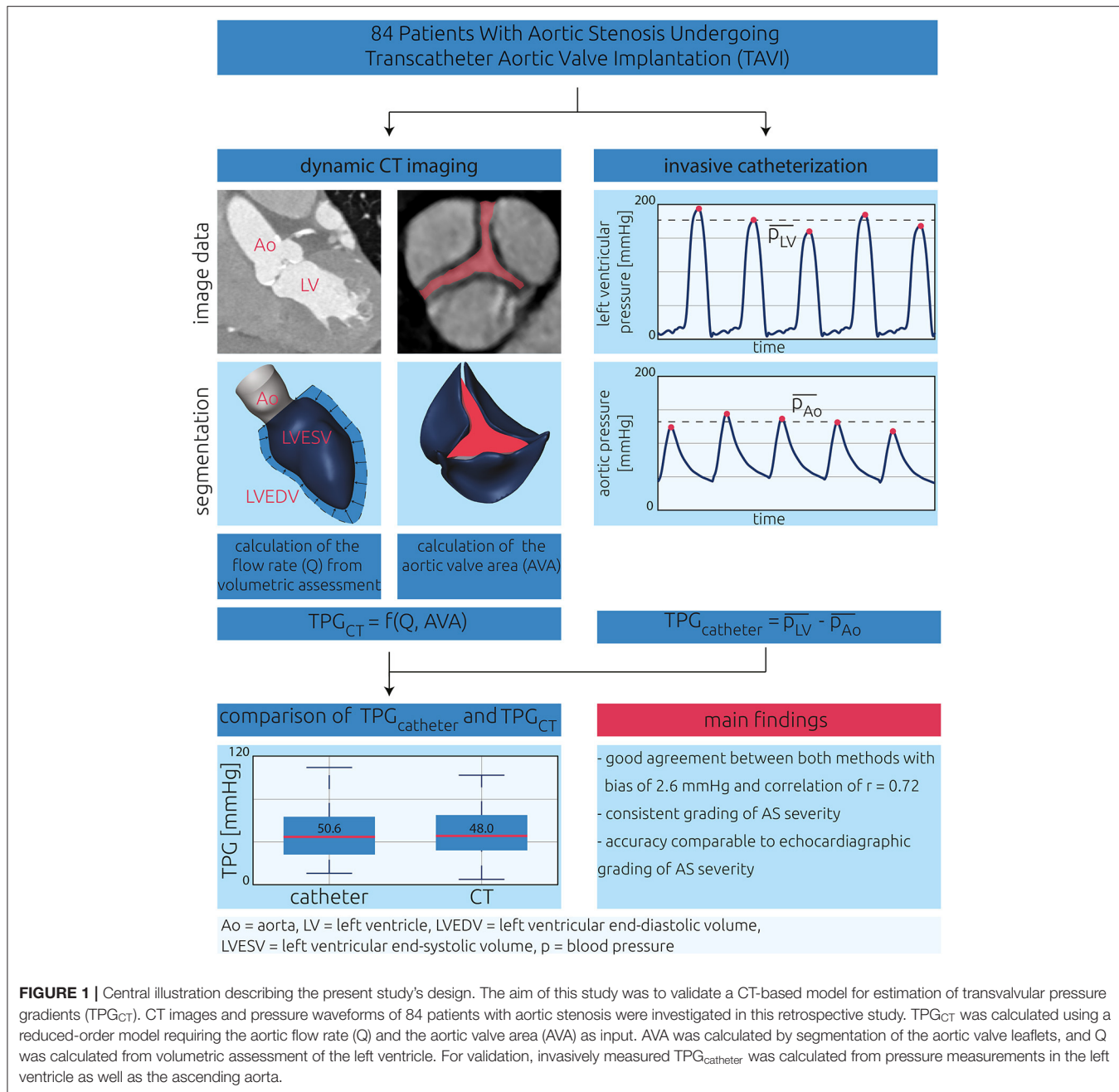
Based on the decision of the Heart Team, catheterization was performed under local (remifentanil) or general anesthesia (propofol and remifentanil). Blood pressure waveforms were measured in the ascending aorta as well as in the left ventricle using a 6-F pigtail catheter (Cordis, Dublin, Ireland). Measurements in the ascending aorta were always performed before measurements in the left ventricle. For each measurement, at least three consecutive cardiac cycles were acquired. The peak-systolic pressure in the left ventricle and the ascending aorta was calculated as the average of all peak values. $\text{TPG}_{\text{catheter}}$ was then calculated as the difference between the average peak-systolic pressure in the left ventricle and the ascending aorta.

Non-invasive Measurements of Pressure Gradients Using Doppler Ultrasound

In addition to the invasive measurement of $\text{TPG}_{\text{catheter}}$, non-invasive measurements using Doppler ultrasound and the Bernoulli equation ($\text{TPG}_{\text{echo}} = 4v^2$, where v is the maximum velocity) were acquired from clinical information systems. These measurements were performed as part of the preoperative diagnostic assessment within the same inpatient stay, but not simultaneously to either the catheterization or the CT image acquisition.

Model for CT-Based Estimation of Pressure Gradients

A reduced-order model based on dynamic CT data was used for non-invasive assessment of TPG. For application of the model, the patient-specific volume flow rate (Q) passing through the stenosed aortic valve and the maximum AVA were measured using dynamic CT data (see Figure 1). First, the left ventricular volume was segmented for every time frame of the CT data using an approach described earlier (10, 11). Briefly, using an automated segmentation procedure, a predefined parametric model containing, among others, the left ventricle, the aortic bulbus, the ascending aorta, and the three aortic leaflets was adapted to the Hounsfield values of the patient-specific CT data for each time frame. Thus, the three-dimensional geometries of these anatomical structures were available. The peak-systolic volume flow rate was then calculated by calculating the left ventricular volume change between the respective time frames



and dividing the difference by the temporal resolution of the CT images. In the presence of a mitral insufficiency (MI), Q was reduced by 10, 30, or 50%, for mild, moderate, and severe MI, respectively. Grading of MI severity was assessed from retrospective Doppler ultrasound reports. The regurgitation fraction used to adjust the aortic flow rate for MI corresponds to the lower thresholds defined for multimodal assessment of MI (12, 13).

The model used in the automatic segmentation procedure assumes an almost point-symmetric aortic valve, where all three leaflets are similar in size and shape. To mitigate this

rather strong assumption, the aortic valve segmentation was manually adjusted to better represent the patient-specific valve. Here, a plane parallel to the aortic annulus was specified. Then, the contours of each leaflet were adjusted by manual interaction to fit on the Hounsfield contours visible in the CT images for multiple slices downstream the aortic annulus until the last leaflet tip was not visible anymore. This procedure was only performed for the peak-systolic phase where the maximum AVA was observed. AVA was calculated by identifying the minimal projected area enclosed by the three aortic valve leaflets.

With the use of both parameters, the non-invasive TPG_{CT} was calculated as

$$TPG_{CT} = 185.5 \cdot Q^{1.483} \cdot AVA^{-1.385} \quad (1)$$

Here, TPG_{CT} is in mmHg, Q in l/s, and AVA in cm^2 .

For this study, the model's coefficients were adjusted compared with an initial feasibility study (11) as the segmentation procedure was optimized to better capture the asymmetry of native aortic valves. For the adjustment, computational fluid dynamic simulations were performed for 58 patients, following the description of Franke et al. (11). Thus, the numerical setup will only be described in a succinct manner.

The patient-specific anatomy of the left ventricle, ascending aorta, and aortic leaflets was smoothed; and the left ventricle was cut perpendicular to the left ventricular outflow tract's (LVOT's) centerline, ~20–30 mm below the aortic valve annulus. With the use of STAR-CCM+ (v. 15.02, Siemens PLM Software Inc., Plano, TX, USA), polyhedral volume meshes with a base size of 0.5–0.8 mm and a boundary layer consisting of five prism cell layers were generated. Each prism cell layer's thickness was 20% larger than that of the previous one. The overall thickness of this boundary layer was one-third of the base size. Near the aortic valve leaflets, a refinement region was specified, where the base size was reduced by half. At the LVOT, the peak-systolic volume flow rate Q was specified as boundary condition. At the end of the ascending aorta, a constant pressure outlet boundary condition was specified. Walls were assumed to be rigid, and a no-slip boundary condition was applied. Blood was modeled as non-Newtonian fluid with a constant density of 1,050 kg/m³. The fluid's dynamic viscosity was modeled using the Carreau–Yasuda model described by Karimi et al. (14). A realizable k-epsilon two-equation turbulence model was used. Simulations were considered converge if the calculated TPG was stable and convergence criteria for mass and momentum were below a threshold of 10^{-3} . TPG was calculated as the difference in surface-averaged static pressure upstream and downstream the stenosed aortic valve. The three model coefficients, i.e., the constant coefficient as well the exponents for AVA and Q in Equation (1), were then calculated using the curve fitting toolbox and the non-linear least-square option provided by MATLAB (v. 2019b, MathWorks Inc., Natick, MA, USA).

Only data sets that were not used for validation (e.g., data of patients for whom a CT scan but no invasive pressure measurements were available) were included in this adjustment cohort.

Statistical, Error, and Operator-Bias Analysis

Distributions of evaluated parameters were visualized using boxplots. Agreement between $TPG_{catheter}$ and the TPG_{CT} was visualized using the Bland–Altman plots. Differences between heart rates during TAVI and CT as well as between $TPG_{catheter}$ and TPG_{CT} were tested for significance. Here, the differences were tested for normal distribution using the Shapiro–Wilk test.

In case of normal distribution, a paired-samples t -test was used. Otherwise, differences were tested using a Wilcoxon signed-rank test. The same metrics were also calculated for the agreement between $TPG_{catheter}$ and TPG_{echo} .

To investigate possible systematic error sources, the model's prediction error ($TPG_{catheter} - TPG_{CT}$) was compared for the following confounding variables: HR difference between catheterization and CT, degree of MI, temporal resolution of the dynamic CT, and patient's sex. Here, a paired-sample t -test was used for normally distributed parameters, whereas a Mann–Whitney U -test was used otherwise. Additionally, some AS patients included in this study were identified as low-flow low-gradient cases. The prediction error of patients with low-flow low-gradient stenosis was then compared with the prediction error of those without. Here, a two-sample t -test was used.

For quantification of the intra- and interobserver variabilities, 10 cases were chosen from the validation cohort. For intraobserver variability, analysis segmentations of the aortic valve geometries were repeated by the main operator 6 months after the initial segmentations. In addition, segmentations were performed by another user for analysis of interobserver variability. Based on these segmentations, AVA was then calculated and compared with each other. For both analyses, intraclass correlation coefficients (ICCs) were calculated according to the convention by McGraw and Wong [ICC (1) (15)]. Only the operator bias on AVA was investigated, as the volume flow rate quantification was based upon the automatic segmentation of the left ventricle.

A significance level of $p = 0.05$ was used for all hypothesis tests.

RESULTS

Following the inclusion criteria, data of 84 (43 female) patients were used for validation of TPG_{CT} . Patient characteristics at baseline are presented in Table 1. This information includes demographic, catheter-, CT-, and echocardiographic-based parameters. The average and standard deviation of AVA calculated from the segmented aortic valves was $0.75 \pm 0.25 \text{ cm}^2$, with individual values ranging from 0.31 to 1.77 cm^2 . The peak-systolic flow rate (Q) passing through the stenosed aortic valve featured an average and standard deviation of $296 \pm 106 \text{ ml/s}$, with individual values ranging from 98 to 584 ml/s . TPG_{CT} , which was calculated using Q and AVA , resulted in an average and standard deviation of $48.0 \pm 25.9 \text{ mmHg}$.

The average and standard deviation of the systolic, static pressure measured in the left ventricle and the ascending aorta was 162.7 ± 32.4 and $113.1 \pm 25.0 \text{ mmHg}$, respectively, resulting in a $TPG_{catheter}$ of $50.6 \pm 27.4 \text{ mmHg}$. For TPG_{echo} , the average and standard deviation was $61.9 \pm 22.0 \text{ mmHg}$.

According to a Wilcoxon signed-rank test, the heart rate during catheterization was significantly lower than that during CT acquisition: 62.5 ± 13.2 vs. $70.7 \pm 20.1 \text{ bpm}$, $p < 0.001$ (see Figure 2A). All individual parameters are provided as Supplementary Material.

TABLE 1 | Overview of relevant parameters of the present study.

Parameter		Mean \pm SD	Range	Data availability	
Name	Unit		Min	Max	
General patient information					
Age	(Years)	82 \pm 5	61	94	84 (100%)
Height*	(cm)	168 \pm 10	145	195	78 (90%)
Weight*	(kg)	77 \pm 19	35	135	80 (95%)
BSA*	(m ²)	1.86 \pm 0.25	1.20	2.41	78 (93%)
Systolic blood pressure (cuff measurement)*	(mmHg)	134.7 \pm 22.8	90.0	198.0	76 (90%)
Diastolic blood pressure (cuff measurement)*	(mmHg)	71.0 \pm 14.5	40	106	76 (90%)
Computed tomography					
AVA	(cm ²)	0.79 \pm 0.25	0.31	1.77	84 (100%)
Peak-systolic flow rate	(ml/s)	296 \pm 106	98	584	84 (100%)
TPG _{CT}	(mmHg)	48.0 \pm 25.9	10.4	109.0	84 (100%)
Heart rate*	(1/min)	71 \pm 20	37	132	81 (96%)
Number of time frames	(–)	20 (11–20)	6	22	84 (100%)
Ejection fraction	(%)	58 \pm 15	19	83	84 (100%)
Stroke volume	(ml)	79.1 \pm 24.9	25.9	138.7	84 (100%)
Stroke volume index*	(ml/m ²)	43.3 \pm 12.3	19.3	81.1	78 (93%)
Cardiac output	(l/min)	5.5 \pm 1.8	2.6	11.7	84 (100%)
Total calcium volume*	(mm ³)	986 \pm 497	6	2,643	65 (77%)
At non-coronary leaflet	(mm ³)	459 \pm 292	0	1,298	65 (77%)
At left coronary leaflet	(mm ³)	265 \pm 150	0	781	65 (77%)
At right coronary leaflet	(mm ³)	261 \pm 177	0	1,085	65 (77%)
Catheterization					
Pressure in left ventricle	(mmHg)	162.7 \pm 32.4	100	259	84 (100%)
Pressure in ascending aorta	(mmHg)	113.1 \pm 25.0	65	182	84 (100%)
TPG _{catheter}	(mmHg)	50.5 \pm 28.0	5	160	84 (100%)
Heart rate*	(1/min)	63 \pm 13	39	108	83 (99%)
Echocardiography					
TPG _{echo} *	(mmHg)	61.9 \pm 22.0	20.0	118.0	80 (95%)
AVA _{echo}	(cm ²)	0.74 \pm 0.17	0.4	1.1	74 (88%)
Stroke volume*	(ml)	52.2 \pm 16.7	17.0	97.0	65 (77%)
Stroke volume index*	(ml/m ²)	28.4 \pm 9.0	9.3	52.5	63 (75%)
Ejection fraction*	(%)	57.3 \pm 8.9	25.0	73.0	78 (93%)
Severity of aortic regurgitation (number of patients)*	(–)	None (11)	Mild (56)	Moderate (9)	76 (90%)
Severity of mitral regurgitation (number of patients)	(–)	None (9)	Mild (59)	Moderate (16)	84 (100%)

All values, except for the number of time frames, are given as mean and standard deviation (SD). The number of time frames is specified as median and interquartile range (IQR) (75th–25th percentile). The range for all parameters is given as well. Body surface area (BSA) was calculated using the DuBois formula. Parameters highlighted using*, i.e., echocardiographic information, except degree of mitral insufficiency, were not available for all patients. The number and percentage of available data sets are given as data availability in absolute values and percent.

CT-Based Prediction of the Transvalvular Pressure Gradient

A Bland–Altman plot comparing TPG_{CT} against TPG_{catheter} is shown in **Figure 3**. The bias between both methods, which is defined by the average of the differences of both methods and the standard deviation of those differences, was 2.6 ± 19.3 mmHg, which resulted in relatively wide limits of agreement, defined as mean \pm 1.96 times the standard deviation of -35.2 to 37.9 mmHg. The means of both methods did not differ significantly, according to a Wilcoxon signed-rank test ($p = 0.56$), and a good correlation between the non-invasive estimation of TPG and

the catheter-based measurements was observed ($r = 0.72$, $p < 0.001$, see **Figure 4**). Both pressure gradient distributions and all individual values of both methods are shown in **Figure 2B**. In contrast, the correlation between TPG_{catheter} and TPG_{echo} was $r = 0.80$, and the average and standard deviation of the differences between those two methods was -11.5 ± 16.4 mmHg, resulting in limits of agreement of -43.6 to 20.6 mmHg. TPG_{echo} systematically overpredicted TPG_{catheter} ($p < 0.001$, paired-samples *t*-test).

Discriminating patients by their sex revealed only minor differences in the predictive capabilities of the model. For women,

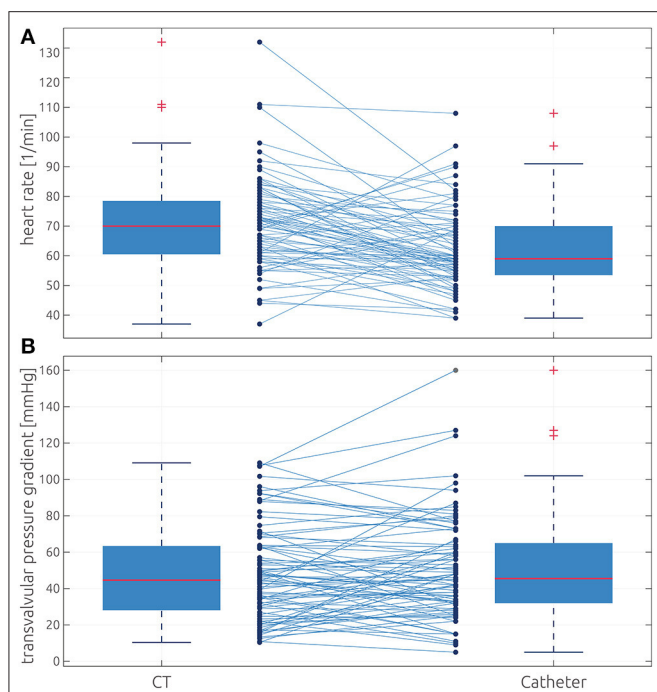


FIGURE 2 | Comparison of heart rate and transvalvular pressure gradient distributions between both methods. **(A)** Box plots showing the measured heart rate during CT (left) and catheterization (right). **(B)** Box plots showing the distributions of TPG_{CT} (left) and the TPG_{catheter} (right). The box defines the range from the 25th to 75th percentile, whereas the whiskers indicate the inner 99% assuming normal distribution. Values outside this range are marked as outliers using red crosses. All individual values and their correspondence between both methods are shown as connected dots.

the average and standard deviation of the differences between both methods was 5.2 ± 18.8 mmHg whereas -0.1 ± 19.5 mmHg for men ($p = 0.14$). Significant differences between women and men were found for AVA (0.71 vs. 0.87 cm 2 , $p < 0.001$) and volume flow rate (271 vs. 321 ml/s, $p = 0.03$), with both parameters being larger in men than in women. While TPG_{catheter} (55.4 vs. 45.7 mmHg) and TPG_{CT} (50.2 vs. 45.8 mmHg) were larger in female patients than in male patients, these differences were not significant ($p = 0.11$ and 0.47 , respectively).

Additional to the effect of the patients' sex, the influence of three possible sources of error on the accuracy of the model was investigated. No relevant bias in the model's accuracy was found between patients who featured an absolute heart rate difference between CT and catheterization of 10 bpm or more and those patients with similar heart rates during both procedures: 3.2 ± 21.0 vs. -1.1 ± 17.3 mmHg, $p = 0.35$. In contrast, the temporal resolution of the dynamic CT images has a strong effect on the model's prediction error. The average and standard deviation of the prediction error was 21.3 ± 20.9 mmHg for cases where a heartbeat was resolved with 10 phases or less, whereas it was -3.4 ± 16.2 mmHg when a higher temporal resolution was available ($p < 0.001$). The model's prediction error was also larger in patients with moderate MI compared with patients with no or only mild MI: 12.1 ± 18.1 vs. 0.17 ± 20.2 mmHg, $p = 0.03$. The

respective distributions of the model's prediction error are shown in Figure 5. Finally, the prediction error for patients who have been identified as low-flow low-gradient cases ($n = 11$) during clinical routine was compared with that of all other patients ($n = 63$). On average, in low-flow low-gradient cases, TPG_{CT} was larger than TPG_{catheter} (-8.6 ± 15.0 mmHg), whereas predicted TPG_{CT} was smaller than the catheter-based measurements for all other patients (4.3 ± 19.6 mmHg). However, this difference was not significant according to a two-sample *t*-test ($p = 0.25$).

To quantify consistency in grading of AS severity, a maximum TPG threshold of 64 mmHg was used, corresponding to the maximum velocity of 4 m/s and the corresponding mean threshold of 40 mmHg defined in clinical guidelines. In 77 of 84 patients (91.7%), both methods consistently predicted a TPG of either below or above 64 mmHg. In four patients (4.8%), TPG_{catheter} was above this threshold, while TPG_{CT} was smaller than 64 mmHg. Finally, in two patients (2.3%), TPG_{CT} was above 64 mmHg, whereas TPG_{catheter} was below this threshold.

ICCs calculated for the intra- and interobserver analyses were 0.99 and 0.88, indicating an excellent intraobserver reliability and a good agreement between different observers.

DISCUSSION

Our results show that CT-based estimation of TPG performs well compared with invasive cardiac catheterization. The proposed method is easy to apply and complements the current diagnostic capabilities of cardiac CT imaging by providing additional functional hemodynamic information.

CT-Based Analysis of Cardiac Anatomy and Function

Recent advancements in cardiac CT have led to significant improvement in image quality while exposure to radiation simultaneously decreased (16, 17). As a result, CT became an essential tool for treatment planning in AS. In clinical routine, CT is mainly used for the evaluation of anatomical structures of the aorta, the valve annulus, coronary arteries, and the LV outflow tract. However, the valve's geometry can also be visualized using CT, allowing direct measurement of AVA (7, 18). The additional possibility of grading the severity of AS using TPG would further enhance the value of CT by transforming it to a unified diagnostic tool for the evaluation of structural heart disease, combining comprehensive assessment of anatomic and hemodynamic information. The presented method is straightforward and allows assessing TPG from ventricular volumes and the anatomy of the aortic valve. While complete automation of the segmentation of the patient-specific left ventricle and the aortic valve is possible (10), manual correction was still necessary due to the aortic valve's asymmetry. However, this correction could also be automated in the future, so that a fully automated approach might be feasible.

The ability to determine hemodynamic parameters would complement various other CT-based functional measurements that have been established in recent years for cardiovascular applications. Well-known examples are measurement of

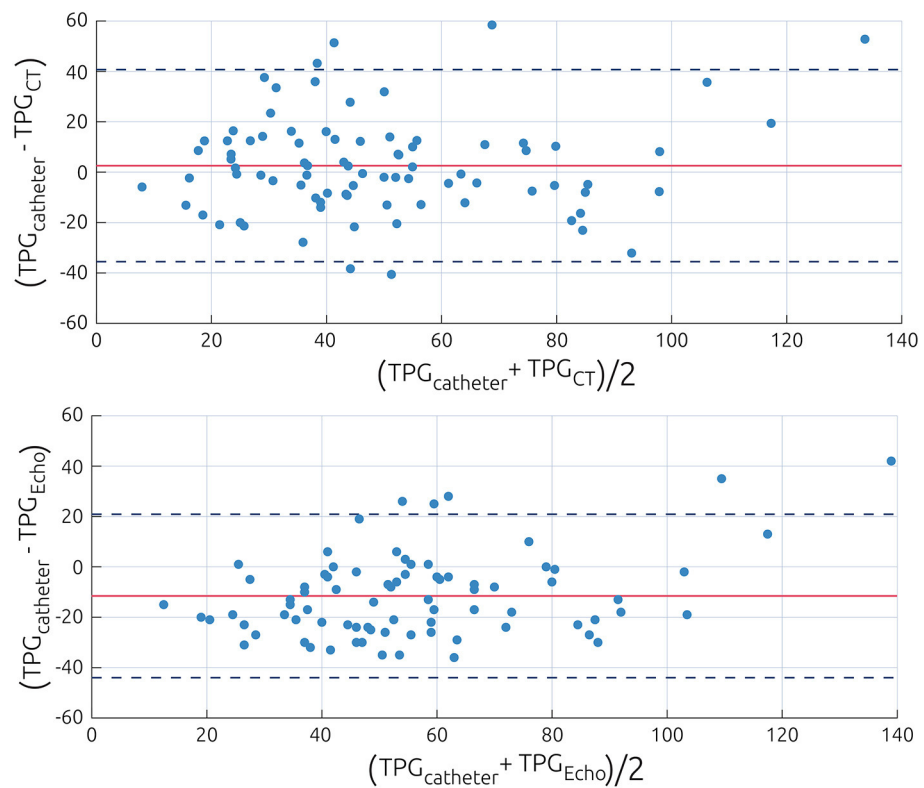


FIGURE 3 | Bland–Altman plot visualizing the differences between the catheter-based measurements of the pressure gradient and the non-invasive estimations using the power law model (**Top**) or Doppler echocardiography (**Bottom**). Data are presented as difference of both methods against the average of both methods. The value of the average prediction error is indicated by a solid line, whereas the dashed lines indicate the average prediction error ± 1.96 times the standard deviation of this error.

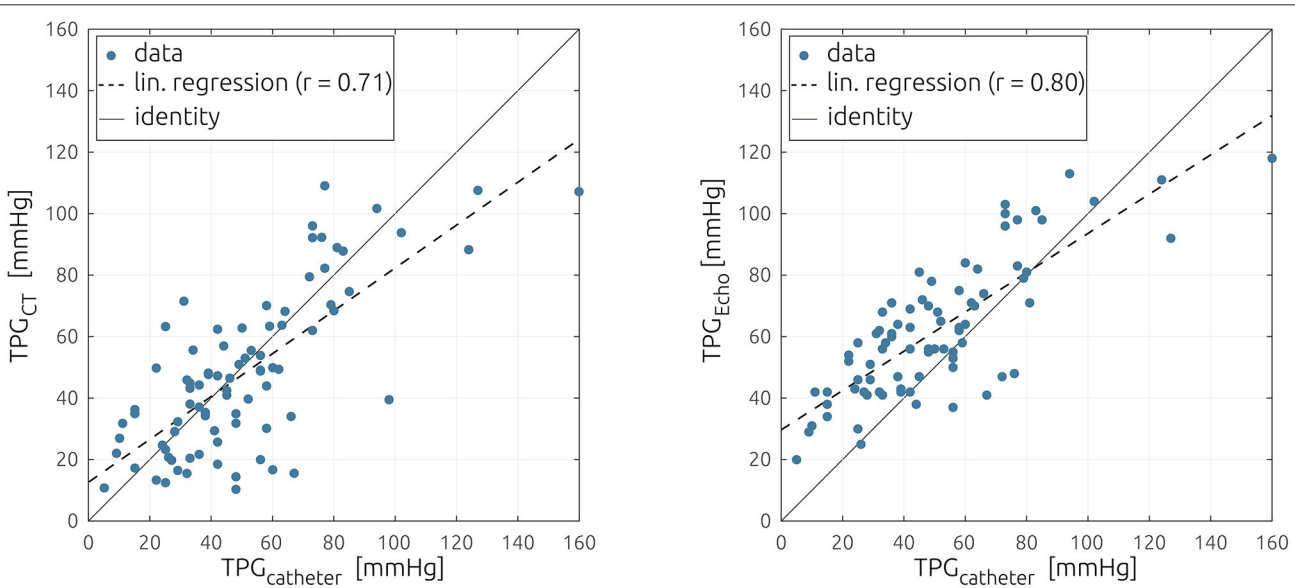


FIGURE 4 | Scatter plot comparing the catheter-based measurements of the pressure gradient against the non-invasive estimation using the reduced-order model (**Left**) and echocardiography (**Right**). The linear regression is shown as a dashed line.

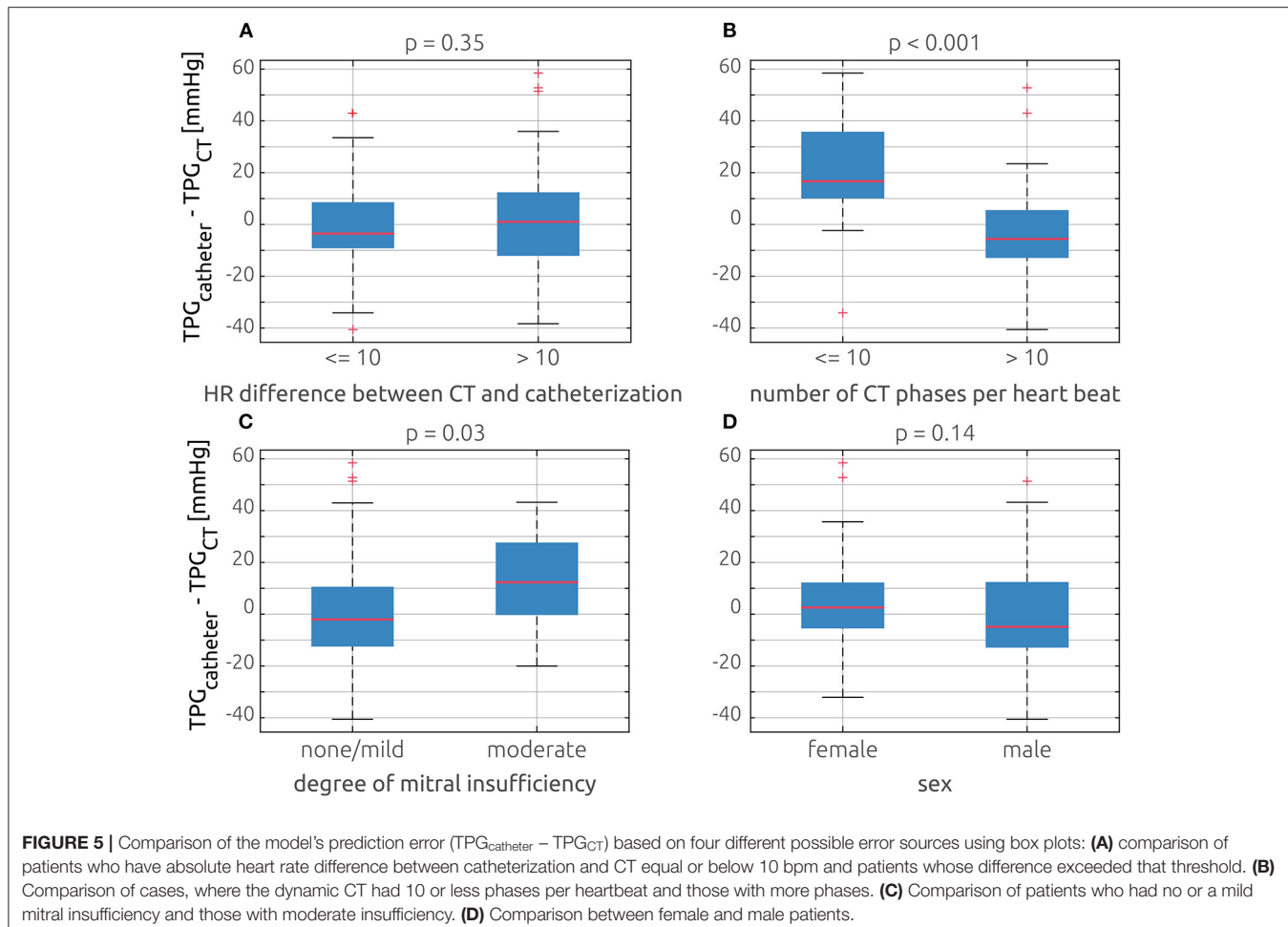


FIGURE 5 | Comparison of the model's prediction error ($\text{TPG}_{\text{catheter}} - \text{TPG}_{\text{CT}}$) based on four different possible error sources using box plots: **(A)** comparison of patients who have absolute heart rate difference between catheterization and CT equal or below 10 bpm and patients whose difference exceeded that threshold. **(B)** Comparison of cases, where the dynamic CT had 10 or less phases per heartbeat and those with more phases. **(C)** Comparison of patients who had no or a mild mitral insufficiency and those with moderate insufficiency. **(D)** Comparison between female and male patients.

myocardial perfusion (19, 20) or calculation of fractional flow reserve in patients with coronary artery disease (21–23).

Grading of Aortic Stenosis Severity

According to clinical guidelines, grading of AS severity is required for treatment planning (4, 5). This grading is currently based on either AVA or TPG. Except for planimetric assessment of AVA, models are used to calculate these parameters from either the velocity information obtained using Doppler echocardiography (e.g., Bernoulli equation for TPG; continuity equation for AVA) or the pressure obtained during heart catheterization (e.g., Gorlin equation for AVA). However, those models require additional measurements, for example, cross-sectional areas of the LVOT and the aorta for application of the continuity equation or the cardiac output and systolic ejection period for application of the Gorlin equation, increasing their uncertainty. For both echocardiography- and catheter-based classifications, inconsistent gradings of AS severity are reported in ~30% of patients (24, 25).

Due to its ubiquitous availability and non-invasiveness, echocardiography is the standard for diagnosis of patients with AS (12), even though it is known to systematically overpredict TPG compared with catheterization (26). This overestimation

results from neglect of blood flow velocities distal to the aortic valve by the Bernoulli equation. Furthermore, the method is susceptible to interobserver variability (27). However, in a well-controlled environment, where echocardiographic and catheter-based assessments of AS severity are performed simultaneously, good correlations ($r > 0.9$), low standard errors of estimate (SEEs < 15 mmHg), and good agreement for graduation of AS severity between both methods were reported (28–31). In contrast, performing the non-invasive assessment 1 week before catheterization led to slightly weaker correlations ($r \approx 0.8$) and increased errors (SEE ≈ 25 mmHg) (30–32).

In our study, we also found a slight overestimation of echocardiography based TPG_{echo}. However, TPG_{echo} correlated well with TPG_{catheter}. While the Bland–Altman analysis revealed relatively large limits of agreement, those were similar to previous studies comparing echocardiography and catheterization. Thus, good agreement with respect to the expected accuracy, except for the systematic overestimation, was found. In terms of the agreement between TPG_{CT} and TPG_{catheter}, our results were also similar to the findings reported in studies comparing invasive catheterization and echocardiography as well as the echocardiographic measurements acquired for this study's cohort. With a consistent grading of severity in 92% of all

cases, the presented approach performed exceptionally well in this regard.

In this study, direct measurements of TPG using cardiac catheterization, clinically considered as gold standard, was considered as ground truth against which the reduced-order model was validated. However, even this technique is associated with errors. Using two independent measurements in the LV and the aorta rather than simultaneous pressure measurements may affect the quantification of TPG. Furthermore, the position of the catheter in the ascending aorta, as well as the additional decrease of the aortic valve's cross section due to the catheter, especially in patients with already low AVA, may affect accuracy (33).

Error Analysis

Analysis of different probable sources for bias revealed that the model's prediction of TPG worked equally well for male and female patients. While a heart rate difference between CT and catheterization of 10 bpm or more resulted in significantly larger prediction error, this effect was rather small. The presence of a moderate MI as well as a limited temporal resolution of CT images of 10 or less phases resulted in differences in the model's prediction error of more than 10 mmHg on average. As the volume flow rate Q is derived from left ventricle segmentations, the limited temporal resolution resulted in an inaccurate assessment of the left ventricle volume change and thus of the volume flow rate. Therefore, the peak-systolic flow rate was underestimated, which led to an underestimation of TPG_{CT} .

Similarly, TPG_{CT} was smaller than $TPG_{catheter}$ for patients with moderate MI, suggesting that the compensation of the aortic flow was too rigorous, resulting in an underestimation of Q and thus of TPG_{CT} . If the model is only applied to the 55 patients with a temporal CT resolution of more than 10 phases per heartbeat and no or only a mild MI, the correlation between methods increases to $r = 0.81$, and SEE decreases to 15.3 mmHg. Out of the seven outliers shown in the Bland–Altman plot (Figure 3), five had a moderate regurgitation, or a limited temporal resolution, or both. Therefore, more thoroughly constraining the inclusion criteria for future investigations using the presented approach might be warranted.

Limitations

There are several important limitations to this study. Due to the retrospective study design, data acquisition was not performed simultaneously but with a median delay of 12 (1–148) days, which certainly decreases the agreement between all methods compared. In contrast to CT and transthoracic echocardiographic (TTE) examinations, catheterization was performed under sedation, which further affects hemodynamics and therefore accuracy of TPG assessment. Additionally, the proposed CT-based TPG assessment still requires minor manual interaction, which might represent a potential additional error source.

As the study only includes TAVI patients, we cannot exclude a certain selection bias due to the type of intervention. However, due to the retrospective study design, this limitation could not be mitigated, as TAVI patients were the only AS patients for whom pressure gradients were routinely measured using

catheterization. Also, the decision between TAVI and surgical valve replacement is based on risk scores rather than the severity of the AS; thus, neither the AVA nor the peak-systolic volume flow rate is relevant for this decision. The stenosis relevant parameter (e.g., AVA and TPG) distributions are similar between patients undergoing TAVI or surgical valve replacement (34). Nonetheless, the validity of this assumption as well as the applicability of this approach in patients with low gradients should be evaluated in a future prospective trial.

Outlook

The presented reduced-order model might be extended by a functionality to also predict TPG during physical exercise in the future. The change of cardiovascular functional parameters (e.g., cardiac output or peak-systolic flow rate) due to physical exercise can be predicted if these parameters were known at rest (35). In our own preliminary work comparing cardiac catheterization and pharmaceutical exercise testing using dobutamine, the increase in TPG during physical stress was successfully predicted (36). As changes in AVA during physical stress are rather small, this approach might be applicable to our approach, allowing non-invasive assessment of TPG at different levels of exercise. The findings of this study, especially regarding the level of agreement between both methods and possible error sources, are vital for the design of a prospective validation study. Here, an *a priori* power analysis for sample size estimation, simultaneous acquisition, or at least acquisition in close succession of CTA and catheter-based pressure gradients seems warranted.

CONCLUSION

The presented approach allows estimation of TPG in patients with AS from dynamic cardiac CT images only. This additional hemodynamic assessment might complement the current diagnostic capabilities of cardiac CT and hence the preoperative treatment planning of patients with AS.

DATA AVAILABILITY STATEMENT

The original contributions presented in the study are included in the article/**Supplementary Material**, further inquiries can be directed to the corresponding author/s.

ETHICS STATEMENT

The studies involving human participants were reviewed and approved by Ethikkommission der Charité—Universitätsmedizin Berlin. Written informed consent for participation was not required for this study in accordance with the national legislation and the institutional requirements.

AUTHOR CONTRIBUTIONS

LG, TK, and MS: conceptualization. HD, AB, AL, NS, and BJ: data curation. BF, JB, and LG: formal analysis and methodology. TK and MS: funding acquisition and

supervision. MS, HD, AB, AL, and BJ: investigation. JB and MS: validation. BF and JB: visualization. BF, JB, and MS: writing—original draft. All authors writing—review and editing. All authors contributed to the article and approved the submitted version.

FUNDING

MS was participant in the BIH-Charité Junior Digital Clinician Scientist Program funded by the Charité—Universitätsmedizin Berlin and the Berlin Institute of Health.

REFERENCES

- Nishimura RA, Otto CM, Bonow RO, Carabello BA, Erwin JP III, Guyton RA, et al. 2014 AHA/ACC guideline for the management of patients with valvular heart disease: executive summary: a report of the American College of Cardiology/American Heart Association Task Force on Practice Guidelines. *J Am Coll Cardiol.* (2014) 63:2438–88. doi: 10.1161/CIR.000000000000029
- Nkomo VT, Gardin JM, Skelton TN, Gottdiener JS, Scott CG, Enriquez-Sarano M. Burden of valvular heart diseases: a population-based study. *Lancet.* (2006) 368:1005–11. doi: 10.1016/S0140-6736(06)69208-8
- Lindman BR, Clavel MA, Mathieu P, Iung B, Lancellotti P, Otto CM, et al. Calcific aortic stenosis. *Nat Rev Dis Primers.* (2016) 2:16006. doi: 10.1038/nrdp.2016.6
- Otto CM, Nishimura RA, Bonow RO, Carabello BA, Erwin JP III, Gentile F, et al. 2020 ACC/AHA guideline for the management of patients with valvular heart disease: executive summary: a report of the American College of Cardiology/American Heart Association Joint Committee on Clinical Practice Guidelines. *Circulation.* (2021) 143:e35–71. doi: 10.1161/CIR.0000000000000932
- Baumgartner H, Falk V, Bax JJ, De Bonis M, Hamm C, Holm PJ, et al. 2017 ESC/EACTS guidelines for the management of valvular heart disease. *Rev Esp Cardiol.* (2018) 71:110. doi: 10.1016/j.rec.2017.12.013
- Hoeijmakers M, Silva Soto DA, Waechter-Stehle I, Kasztelnik M, Weese J, Hose DR, et al. Estimation of valvular resistance of segmented aortic valves using computational fluid dynamics. *J Biomech.* (2019) 94:49–58. doi: 10.1016/j.jbiomech.2019.07.010
- Mittal TK, Reichmuth L, Bhattacharyya S, Jain M, Baltaeva A, Rahman Haley S, et al. Inconsistency in aortic stenosis severity between CT and echocardiography: prevalence and insights into mechanistic differences using computational fluid dynamics. *Open Heart.* (2019) 6:e001044. doi: 10.1136/openhrt-2019-001044
- Pawade T, Clavel MA, Tribouilloy C, Dreyfus J, Mathieu T, Tastet L, et al. Computed tomography aortic valve calcium scoring in patients with aortic stenosis. *Circ Cardiovasc Imaging.* (2018) 11:e007146. doi: 10.1161/CIRCIMAGING.117.007146
- Clavel MA, Magne J, Pibarot P. Low-gradient aortic stenosis. *Eur Heart J.* (2016) 37:2645–57. doi: 10.1093/euroheartj/ehw096
- Weese J, Lungu A, Peters J, Weber FM, Waechter-Stehle I, Hose DR. CFD- and Bernoulli-based pressure drop estimates: a comparison using patient anatomies from heart and aortic valve segmentation of CT images. *Med Phys.* (2017) 44:2281–92. doi: 10.1002/mp.12203
- Franke B, Weese J, Waechter-Stehle I, Bruning J, Kuehne T, Goubergrits L. Towards improving the accuracy of aortic transvalvular pressure gradients: rethinking Bernoulli. *Med Biol Eng Comput.* (2020) 58:1667–79. doi: 10.1007/s11517-020-02186-w
- Zoghbi WA, Enriquez-Sarano M, Foster E, Grayburn PA, Kraft CD, Levine RA, et al. American society of recommendations for evaluation of the severity of native valvular regurgitation with two-dimensional and Doppler echocardiography. *J Am Soc Echocardiogr.* (2003) 16:777–802. doi: 10.1016/S0894-7317(03)00335-3
- Chew PG, Bounford K, Plein S, Schlosshan D, Greenwood JP. Multimodality imaging for the quantitative assessment of mitral regurgitation. *Quant Imaging Med Surg.* (2018) 8:342–59. doi: 10.21037/qims.2018.04.01
- Karimi S, Dabagh M, Vasava P, Dadvar M, Dabir B, Jalali P. Effect of rheological models on the hemodynamics within human aorta: CFD study on CT image-based geometry. *J Non-Newton Fluid.* (2014) 207:42–52. doi: 10.1016/j.jnnfm.2014.03.007
- McGraw KO, Wong SP. Forming inferences about some intraclass correlation coefficients. *Psychol Methods.* (1996) 1:30–46. doi: 10.1037/1082-989X.1.1.30
- Kolossvary M, Kellermayer M, Merkely B, Maurovich-Horvat P. Cardiac computed tomography radiomics: a comprehensive review on radiomic techniques. *J Thorac Imaging.* (2018) 33:26–34. doi: 10.1097/RTI.0000000000000268
- Ginat DT, Gupta R. Advances in computed tomography imaging technology. *Annu Rev Biomed Eng.* (2014) 16:431–53. doi: 10.1146/annurev-bioeng-121813-113601
- Pouleur AC, le Polain de Waroux JB, Pasquet A, Vanoverschelde JL, Gerber BL. Aortic valve area assessment: multidetector CT compared with cine MR imaging and transthoracic and transesophageal echocardiography. *Radiology.* (2007) 244:745–54. doi: 10.1148/radiol.2443061127
- Taron J, Foldyna B, Eslami P, Hoffmann U, Nikolaou K, Bamberg F. Cardiac computed tomography - more than coronary arteries? A clinical update. *Rofo.* (2019) 191:817–26. doi: 10.1055/a-0924-5883
- Nakahara T, Toyama T, Jinzaki M, Seki R, Saito Y, Higuchi T, et al. Quantitative analysis of iodine image of dual-energy computed tomography at rest: comparison with 99mTc-tetrofosmin stress-rest single-photon emission computed tomography myocardial perfusion imaging as the reference standard. *J Thorac Imaging.* (2018) 33:97–104. doi: 10.1097/RTI.0000000000000284
- Coenen A, Rossi A, Lubbers MM, Kurata A, Kono AK, Chelu RG, et al. Integrating CT myocardial perfusion and CT-FFR in the work-up of coronary artery disease. *JACC Cardiovasc Imaging.* (2017) 10:760–70. doi: 10.1016/j.jcmg.2016.09.028
- Taylor CA, Fonte TA, Min JK. Computational fluid dynamics applied to cardiac computed tomography for noninvasive quantification of fractional flow reserve: scientific basis. *J Am Coll Cardiol.* (2013) 61:2233–41. doi: 10.1016/j.jacc.2012.11.083
- Driessens RS, Danad I, Stuijfzand WJ, Rajmakers PG, Schumacher SP, van Diemen PA, et al. Comparison of coronary computed tomography angiography, fractional flow reserve, and perfusion imaging for ischemia diagnosis. *J Am Coll Cardiol.* (2019) 73:161–73. doi: 10.1016/j.jacc.2018.10.056
- Minners J, Allgeier M, Gohlke-Baerwolf C, Kienzle RP, Neumann FJ, Jander N. Inconsistencies of echocardiographic criteria for the grading of aortic valve stenosis. *Eur Heart J.* (2008) 29:1043–8. doi: 10.1093/euroheartj/ehm543
- Minners J, Allgeier M, Gohlke-Baerwolf C, Kienzle RP, Neumann FJ, Jander N. Inconsistent grading of aortic valve stenosis by current guidelines: haemodynamic studies in patients with apparently normal left ventricular function. *Heart.* (2010) 96:1463–8. doi: 10.1136/hrt.2009.181982
- Baumgartner H, Stefenelli T, Niederberger J, Schima H, Maurer G. “Overestimation” of catheter gradients by Doppler ultrasound in patients

ACKNOWLEDGMENTS

The authors wish to thank Irina Waechter-Stehle and Jürgen Weese from Philips GmbH Innovative Technologies for providing the model, which was used for semi-automatic segmentation of the left ventricle and the aortic valve.

SUPPLEMENTARY MATERIAL

The Supplementary Material for this article can be found online at: <https://www.frontiersin.org/articles/10.3389/fcvm.2021.706628/full#supplementary-material>

- with aortic stenosis: a predictable manifestation of pressure recovery. *J Am Coll Cardiol.* (1999) 33:1655–61. doi: 10.1016/S0735-1097(99)00666-2
27. Wong S, Spina R, Toemoe S, Dhital K. Is cardiac magnetic resonance imaging as accurate as echocardiography in the assessment of aortic valve stenosis? *Interact Cardiovasc Thorac Surg.* (2016) 22:480–6. doi: 10.1093/icvts/ivv362
 28. Jaffe WM, Roche AH, Coverdale HA, McAlister HF, Ormiston JA, Greene ER. Clinical evaluation versus Doppler echocardiography in the quantitative assessment of valvular heart disease. *Circulation.* (1988) 78:267–75. doi: 10.1161/01.CIR.78.2.267
 29. Zoghbi WA, Farmer KL, Soto JG, Nelson JG, Quinones MA. Accurate noninvasive quantification of stenotic aortic valve area by Doppler echocardiography. *Circulation.* (1986) 73:452–9. doi: 10.1161/01.CIR.73.3.452
 30. Currie PJ, Seward JB, Reeder GS, Vlietstra RE, Bresnahan DR, Bresnahan JF, et al. Continuous-wave Doppler echocardiographic assessment of severity of calcific aortic stenosis: a simultaneous Doppler-catheter correlative study in 100 adult patients. *Circulation.* (1985) 71:1162–9. doi: 10.1161/01.CIR.71.6.1162
 31. Currie PJ, Hagler DJ, Seward JB, Reeder GS, Fyfe DA, Bove AA, et al. Instantaneous pressure gradient: a simultaneous Doppler and dual catheter correlative study. *J Am Coll Cardiol.* (1986) 7:800–6. doi: 10.1016/S0735-1097(86)80339-4
 32. Parameswaran AC, Reisner D, Amanullah A. Discrepancy between gradients derived by cardiac catheterization and by Doppler echocardiography in aortic stenosis: how often does pressure recovery play a role? *Echocardiography.* (2009) 26:1000–5; quiz: 999. doi: 10.1111/j.1540-8175.2009.00909.x
 33. McWilliams RG, Robertson I, Smye SW, Wijesinghe L, Kessel D. Sources of error in intra-arterial pressure measurements across a stenosis. *Eur J Vasc Endovasc Surg.* (1998) 15:535–40. doi: 10.1016/S1078-5884(98)80116-0
 34. Makkar RR, Thourani VH, Mack MJ, Kodali SK, Kapadia S, Webb JG, et al. Five-year outcomes of transcatheter or surgical aortic-valve replacement. *New Engl J Med.* (2020) 382:799–809. doi: 10.1056/NEJMoa1910555
 35. Runte K, Brosien K, Salcher-Konrad M, Schubert C, Goubergrits L, Kelle S, et al. Hemodynamic changes during physiological and pharmacological stress testing in healthy subjects, aortic stenosis and aortic coarctation patients—a systematic review and meta-analysis. *Front Cardiovasc Med.* (2019) 6:43. doi: 10.3389/fcvm.2019.00043
 36. Runte K, Brosien K, Schubert C, Nordmeyer J, Kramer P, Schubert S, et al. Image-based computational model predicts dobutamine-induced hemodynamic changes in patients with aortic coarctation. *Circ Cardiovasc Imaging.* (2021) 14:e011523. doi: 10.1161/CIRCIMAGING.120.011523

Conflict of Interest: The authors declare that the research was conducted in the absence of any commercial or financial relationships that could be construed as a potential conflict of interest.

Publisher's Note: All claims expressed in this article are solely those of the authors and do not necessarily represent those of their affiliated organizations, or those of the publisher, the editors and the reviewers. Any product that may be evaluated in this article, or claim that may be made by its manufacturer, is not guaranteed or endorsed by the publisher.

Copyright © 2021 Franke, Brüning, Yevtushenko, Dreger, Brand, Juri, Unbehauen, Kempfert, Sündermann, Lembecke, Solowjowa, Kelle, Falk, Kuehne, Goubergrits and Schafstedde. This is an open-access article distributed under the terms of the Creative Commons Attribution License (CC BY). The use, distribution or reproduction in other forums is permitted, provided the original author(s) and the copyright owner(s) are credited and that the original publication in this journal is cited, in accordance with accepted academic practice. No use, distribution or reproduction is permitted which does not comply with these terms.

3.3 Erste Anwendung der patientenspezifischen virtuellen Therapieplanung am Beispiel von drei Patient*innen mit komplexer univentrikulärer Physiologie

Nachdem die Validierung ergab, dass eine bildbasierte Vorhersage hämodynamischer Parameter verlässlich ist, wurde die virtuelle patientenspezifische Therapieplanung erstmalig in der Klinik an drei Patient*innen mit komplexer univentrikulärer Physiologie angewandt.

Virtual treatment planning in three patients with univentricular physiology using computational fluid dynamics – Pitfalls and strategies

Marie Schafstedde, Pavlo Yevtushenko, Sarah Nordmeyer, Peter Kramer, Anastasia Schleiger, Natalia Solowjowa, Felix Berger, Joachim Photiadis, Yaroslav Mykychak, Mi-Young Cho, Stanislav Ovrioutski, Titus Kühne, Jan Brüning

Der nachfolgende Text entspricht inhaltlich dem Abstrakt der oben genannten Publikation als Übersetzung durch die Autorin:

*„Eine ungleichmäßige Verteilung des hepatovenösen Blutflusses in die Lungenarterien wird als Ursache für die Entwicklung pulmonaler arteriovenöser Malformationen (PAVM) bei Patient*innen mit univentrikulärer Physiologie angenommen. Eine gleichmäßige Verteilung des Lebervenenblutes wird daher als Therapieziel angestrebt. Aktuell gibt es jedoch keine etablierte Methode zur Vorhersage der postinterventionellen Hämodynamik. Die computer-gestützte Strömungssimulation (CFD) bietet die Möglichkeit, die Verteilung des hepatovenösen Blutflusses in patientenspezifischen Anatomien vor und nach einer virtuellen Behandlung zu quantifizieren. Diese Studie untersucht den potenziellen Nutzen und die klinische Anwendbarkeit einer CFD-basierten patientenindividuellen Behandlungsplanung.“*

*Bei drei Patient*innen mit univentrikulärer Fontanzirkulation und PAVM wurden sowohl eine Magnetresonanztomographie (MRT) als auch eine Computertomographie (CT) durchgeführt. Bei allen drei Patient*innen bestand die klinische Indikation für eine Operation oder eine Herzkatheterintervention zur Umleitung und ausgeglicheneren Verteilung des hepatovenösen Blutflusses. Auf Grundlage sowohl der MRT als auch der CT-Daten wurde zunächst die patientenspezifische Anatomie rekonstruiert. Anschließend wurden CFD-Simulationen sowohl für den unbehandelten Zustand als auch für verschiedene chirurgische oder interventionelle Behandlungsoptionen durchgeführt. Diese verschiedenen Behandlungen wurden auf Vorschlag behandelnder Kardiolog*innen und Chirurg*innen für angeborene Herzfehler mit langjähriger*

*Erfahrung in der interventionellen und chirurgischen Behandlung von Patient*innen mit univentrikulärer Physiologie durchgeführt. Die Verteilung des hepatovenösen Blutflusses wurde für alle Simulationen quantifiziert, um die praktikabelste Behandlungsentscheidung hinsichtlich der Umverteilung des Leberblutflusses zu ermitteln.*

*Bei allen drei Patient*innen konnte die komplexe Fontan-Anatomie rekonstruiert werden. Aufgrund des Vorhandenseins von metallischen Stentimplantaten war jedoch ein hybrider Ansatz erforderlich, der sowohl auf CT- als auch auf MRT-Daten beruhte. Die virtuelle Simulation der präinterventionellen Blutflussverteilung stimmte gut mit der tatsächlichen angiografischen Quantifizierung überein. Für jede Patient*in wurde anschließend eine Behandlungsoption ermittelt, die zu einer Verbesserung der Blutflussverteilung führte. Bei einem Patienten lagen Follow-Up Daten nach der Behandlung vor. Hier wichen die virtuelle Behandlungssimulation und die MRT-basierten Flussmessungen um 15 % voneinander ab.*

*Die Kombination moderner Simulationsmethoden mit bildgebenden Verfahren zur Beurteilung der patientenindividuellen Anatomie und Hämodynamik bietet das Potential, die patientenspezifische Therapieplanung bei Patient*innen mit ausgeprägtem hepatischem Flussmismatch und PAVM zu verbessern. In dieser Studie zeigen wir, dass virtuelle Therapieplanung bei Patient*innen mit komplexer univentrikulärer Physiologie und umfangreichen Voreingriffen angewendet werden kann. In einigen Fällen können jedoch hybride Ansätze erforderlich sein, die Informationen aus verschiedenen Bildmodalitäten nutzen.“*



OPEN ACCESS

EDITED BY

Silvia Schievano,
University College London,
United Kingdom

REVIEWED BY

Giovanni Biglino,
University of Bristol, United Kingdom
Marina Hughes,
Norfolk and Norwich University
Hospital, United Kingdom

*CORRESPONDENCE

Marie Schafstedde
marie.schafstedde@charite.de

SPECIALTY SECTION

This article was submitted to
Pediatric Cardiology,
a section of the journal
Frontiers in Cardiovascular Medicine

RECEIVED 17 March 2022

ACCEPTED 18 July 2022

PUBLISHED 03 August 2022

CITATION

Schafstedde M, Yevtushenko P,
Nordmeyer S, Kramer P, Schleiger A,
Solowjowa N, Berger F, Photiadis J,
Mykychak Y, Cho M-Y, Ovroutski S,
Kuehne T and Brüning J (2022) Virtual
treatment planning in three patients
with univentricular physiology using
computational fluid dynamics—Pitfalls and
strategies.

Front. Cardiovasc. Med. 9:898701.
doi: 10.3389/fcvm.2022.898701

COPYRIGHT

© 2022 Schafstedde, Yevtushenko,
Nordmeyer, Kramer, Schleiger,
Solowjowa, Berger, Photiadis,
Mykychak, Cho, Ovroutski, Kuehne and
Brüning. This is an open-access article
distributed under the terms of the
[Creative Commons Attribution License
\(CC BY\)](#). The use, distribution or
reproduction in other forums is
permitted, provided the original
author(s) and the copyright owner(s)
are credited and that the original
publication in this journal is cited, in
accordance with accepted academic
practice. No use, distribution or
reproduction is permitted which does
not comply with these terms.

Virtual treatment planning in three patients with univentricular physiology using computational fluid dynamics—Pitfalls and strategies

Marie Schafstedde^{1,2,3,4*}, Pavlo Yevtushenko²,
Sarah Nordmeyer^{1,2}, Peter Kramer¹, Anastasia Schleiger¹,
Natalia Solowjowa⁵, Felix Berger^{1,4,6}, Joachim Photiadis⁷,
Yaroslav Mykychak⁷, Mi-Young Cho⁷, Stanislav Ovroutski¹,
Titus Kuehne^{1,2,4} and Jan Brüning²

¹Department of Congenital Heart Disease—Pediatric Cardiology, German Heart Center Berlin, Berlin, Germany, ²Institute for Cardiovascular Computer-Assisted Medicine, Charité—Universitätsmedizin Berlin, Berlin, Germany, ³Berlin Institute of Health, Berlin, Germany, ⁴German Centre for Cardiovascular Research, Partner Site Berlin, Berlin, Germany, ⁵Department of Cardiothoracic and Vascular Surgery, German Heart Center Berlin, Berlin, Germany, ⁶Department of Pediatric Cardiology, Charité—Universitätsmedizin Berlin, Berlin, Germany, ⁷Department of Congenital Heart Surgery, German Heart Center Berlin, Berlin, Germany

Background: Uneven hepatic venous blood flow distribution (HFD) to the pulmonary arteries is hypothesized to be responsible for the development of intrapulmonary arteriovenous malformations (PAVM) in patients with univentricular physiology. Thus, achieving uniform distribution of hepatic blood flow is considered favorable. However, no established method for the prediction of the post-interventional hemodynamics currently exists. Computational fluid dynamics (CFD) offers the possibility to quantify HFD in patient-specific anatomies before and after virtual treatment. In this study, we evaluated the potential benefit of CFD-assisted treatment planning.

Materials and methods: Three patients with total cavopulmonary connection (TCPC) and PAVM underwent cardiovascular magnetic resonance imaging (CMR) and computed tomography imaging (CT). Based on this imaging data, the patient-specific anatomy was reconstructed. These patients were considered for surgery or catheter-based intervention aiming at hepatic blood flow re-routing. CFD simulations were then performed for the untreated state as well as for different surgical and interventional treatment options. These treatment options were applied as suggested by treating cardiologists and congenital heart surgeons with longstanding experience in interventional and surgical treatment of patients with univentricular physiology. HFD was quantified for all simulations to identify the most viable treatment decision regarding redistribution of hepatic blood flow.

Results: For all three patients, the complex TCPC anatomy could be reconstructed. However, due to the presence of metallic stent implants, hybrid models generated from CT as well as CMR data were required. Numerical simulation of pre-interventional HFD agreed well with angiographic assessment and physiologic considerations. One treatment option resulting in improvement of HFD was identified for each patient. In one patient follow-up data after treatment was available. Here, the virtual treatment simulation and the CMR flow measurements differed by 15%.

Conclusion: The combination of modern computational methods as well as imaging methods for assessment of patient-specific anatomy and flow might allow to optimize patient-specific therapy planning in patients with pronounced hepatic flow mismatch and PAVM. In this study, we demonstrate that these methods can also be applied in patients with complex univentricular physiology and extensive prior interventions. However, in those cases, hybrid approaches utilizing information of different image modalities may be required.

KEYWORDS

Fontan, univentricular physiology, 4D flow MRI, computed tomography, image-based modeling, computational fluid dynamics, decision support, hepatic factor

Introduction

Initially introduced in 1971 as physiological repair for tricuspid atresia, the Fontan operation aims at abolishing cyanosis by entirely eliminating right to left shunt in patients with univentricular heart disease (1). Its contemporary modification, the staged total cavopulmonary connection (TCPC), has emerged as the standard procedure in the treatment of these patients (2, 3). However, persisting or reoccurring cyanosis is frequently observed (4) and the development of intrapulmonary capillary arteriovenous malformations (PAVM) is one of the possible underlying reasons. Particularly after superior cavopulmonary connection or Kawashima procedure, where hepatic venous flow is usually not directed into the pulmonary arteries, development of PAVM is reported in up to 25% of patients (5). Affected patients suffer from severe cyanosis and increased risk for morbidity and mortality (4–6).

Usually, regression of PAVM and clinical improvement is observed after completion of TCPC, when hepatic venous blood and thus the hypothesized “hepatic factor” is redirected into the pulmonary arteries again (7–9). In cases of incomplete regression or of development of unilateral PAVM after Fontan completion, an uneven distribution of hepatic venous blood flow (HFD) between both pulmonary arteries has been discussed to be responsible (10–15). This is supported by several case reports and studies that observed a resolution of PAVMs after surgical or interventional redirection of hepatic blood flow in Fontan patients (14, 16–18).

In patients with PAVM, the main challenge is to confidently provide a surgical or interventional strategy that will result in a more balanced HFD. Several treatment strategies in terms of various possible anatomical Fontan connections have yet been analyzed (19) and first approaches emerged, evaluating novel surgical treatment options for Fontan patients and envisaging patient-specific treatment planning using virtual manipulation of the patient-specific anatomy and subsequent calculation of hemodynamic results (20–22).

Computational fluid dynamics (CFD) offer the possibility to simulate different treatment strategies and perform outcome predictions, which might enhance and supplement the preoperative or pre-interventional interdisciplinary decision-making process. This is an evolving field with necessity for further validation, however, it might allow to optimize therapy planning and to achieve the desired hemodynamic result in a patient-specific case (23–25).

The heterogeneity of cardiovascular anatomies in Fontan patients may present a particular challenge to the surgical establishment of a Fontan circuit that results in an optimal HFD to both pulmonary arteries. This is particularly true for anatomies with interrupted inferior vena cava and vena azygos/hemiazygos continuation in which TCPC is usually completed by separately connecting the hepatic veins to the pulmonary arteries with an intracardiac tunnel or an extracardiac conduit (18, 26). Especially in these complex cases, virtual treatment simulations are of exceptional clinical interest.

The purpose of this study is hence to evaluate the potential benefit of virtual treatment planning in patients with

univentricular heart malformations and PAVM development due to uneven hepatic flow distribution and to demonstrate feasible diagnostic algorithms using CFD simulations for individualized patient-specific surgical or catheter-based interventional therapy planning to optimize HFD as causal treatment rationale in these patients.

Materials and methods

Study design

Three patients with Fontan circulation and history of PAVM development were retrospectively analyzed. The presence of macroscopic PAVM was determined angiographically using criteria such as macroscopically identifiable pulmonary capillary bed and rapid pulmonary transit time of contrast agent. If technically possible, also pulmonary venous oxygen saturation was measured in the affected and unaffected lung. Due to severe cyanosis and limited physical capacity (objective and subjective), these patients were considered for catheter-based or surgical intervention to improve HFD. For all patients, cardiovascular magnetic resonance imaging (CMR) as well as computed tomography (CT) data was available. The study was approved by the institutional review board and the institutional ethics committee (decision number EA2/126/15). Individual informed consent was waived.

Cardiovascular magnetic resonance imaging acquisition

Cardiovascular magnetic resonance imaging was performed using a 1.5 Tesla CMR system (Achieva; Philips Medical Systems, Best, Netherlands) with a 5-element cardiac phased-array coil. Balanced 3D steady-state-free-precession (SSFP) imaging during end-diastole (3 signal averages, navigator gated, ECG triggered) and cine-sequences were used for reconstruction of the patient-specific anatomy. Flow volume quantification was performed using 2D free-breathing phase contrast cine CMR sequences of all vessels up- and downstream of the Fontan circulation, i.e., the inferior vena cava (IVC), superior vena cava (SVC), right pulmonary artery (RPA), left pulmonary artery (LPA), azygos/hemiazygos vein, innominate vein as appropriate, as well as the aorta. Acquired and reconstructed voxel resolutions of these measurements were $2.3 \times 3.1 \times 7 \text{ mm}^3$ and $1.1-2.2 \times 1.1-2.2 \times 7 \text{ mm}^3$, respectively. Repetition time, echo time, flip angle were 5.1–5.4 ms, 3.0–3.3 ms, 15°, respectively. The velocity encoding of venous vessels was 100 cm/s, whereas 200–400 cm/s were chosen for arterial vessels as appropriate. Aliasing was ruled out in all measurements. All flow measurements were completed with automatic correction of concomitant phase errors.

Computed tomography imaging acquisition

All CT images were acquired using the same dual-source multi-slice spiral computed tomography (CT) scanner (Somatom Definition Flash, Siemens Healthcare GmbH, Erlangen, Germany). Tube currents were adapted individually, whereas a constant tube voltage of 100 kV was used. Spatial resolution of the CT images varied from $0.48 \times 0.48 \text{ mm}^2$ to $0.62 \times 0.62 \text{ mm}^2$, whereas the slice thickness was 0.7 mm for all three patients.

Image post-processing and generation of pre-interventional anatomical models

The patient-specific, pre-interventional anatomy was reconstructed using ZIBAmira (v. 2015.28; Zuse Institute Berlin, Germany). Here, the CT images were used preferably due to better contrast, resolution, and lesser influence of metallic artifacts caused by implants such as stents. However, the inflow from the SVC, and thus the contrast agent distribution, was often uneven. Whereas some regions were flooded by contrast agent, resulting in artifacts due to strong contrast gradients, other regions were not perfused, resulting in poor contrast between vessels and surrounding tissue. Here, SSFP CMR images were used to reconstruct areas that were insufficiently distinguishable in the CT data.

The same methods for image processing and subsequent reconstruction of the patient-specific Fontan circulation were used for MR as well as CT images. Due to the large heterogeneity of the image data, artifacts from metallic stents and contrast agent, regions of interest were selected mostly manually, however, semiautomatic methods such as threshold-based selection of connected regions were used whenever possible. However, no fixed Hounsfield or grayscale threshold was used, but the threshold had to be adapted to the respective image region due to changes in contrast. In general, Hounsfield units between 150 and 200 were used as threshold, in well-contrasted regions of the CT data. Image data was reconstructed by slicing through all three orientations repeatedly. First, the veins and grafts leading into the Fontan circulation, i.e., the SVC and IVC as well as the azygos/hemiazygos vein were reconstructed, followed by the pulmonary arteries. For the validation of reconstructions, angiographic images were additionally evaluated, as this image modality allows for accurate measurement of diameters as well as visualization of anastomosis sites (**Figure 1**).

Anatomical reconstructions from CT and CMR data were registered using the vessels that were identifiable

within both image modalities, which were usually the SVC and IVC. Then, a joint reconstruction of both image modalities was generated by super-imposition. Subsequently, a surface geometry was generated from this reconstruction using a marching cubes algorithm (27). This surface geometry was smoothed using a volume preserving smoothing algorithm (28). Smaller topological errors, as for example non-manifold vertices that resulted from vessels being close to each other, were corrected using Meshmixer (v. 3.5; Autodesk, Mill Valley, CA, United States). This tool was also used to truncate all vessel endings perpendicularly.

Reconstruction of the patient-specific anatomy of the TCPC was conducted by two engineering researchers with several years of experience in image-based reconstruction. They were supported by surgeons and cardiologists by joint evaluation of information available from previous surgical and other reports to better understand the complex anatomy of the TCPC, respective vessels and to select suitable imaging sequences for reconstruction.

Generating surgical and interventional options

For each case, different surgical, catheter-based interventional, and in some cases combined treatment strategies had been proposed after discussion in the institutional heart team that includes interventional and non-interventional cardiologists, as well as congenital cardiac surgeons. These strategies were then virtually implemented by manipulation of the pre-interventional anatomy. While these virtual manipulations were performed by engineering researchers experienced in cardiovascular simulations, all virtual interventions were performed in attendance of at least one heart team member and finally approved by the whole heart team.

The treatment options varied from implantation of covered and bare metal stents, implantation of vascular grafts, resection of existing vascular connections with re-anastomosis at an altered position as well as vascular patch augmentation or reconstruction. Treatment strategies were performed if they were considered feasible. Assessment of feasibility was mainly based on the experience of the heart team member in favor of the respective strategy and subsequent discussions of the entire heart team. In addition to that, several procedural aspects were evaluated: for vascular grafts a pathway not intersecting any relevant structures had to exist; for stent implantation, vessel diameters had to have the right size allowing anchoring of the stent; for vascular graft implantation, the anastomosis site had to be free from scar tissue and not located to close to

a stent. All treatment options were only performed in a qualitative manner, no constitutive models were used to describe anatomical properties.

To facilitate these virtual treatments, all manipulations were performed using Meshmixer. Here, resection of vessels was performed by selection and removing of surface elements. Similarly, the implantation of a covered stent to redirect blood flow was performed by separation of the connection between vessels to be bridged and subsequent closure of these vessels to facilitate two separate lumina. Vascular grafts were first designed in ZIBAmira using a function to generate and manipulate cubic splines in 3D by movement of the different points of the spline. Thus, the path of the vascular graft could be specified considering the surrounding tissues by superimposition of the CT image information. After the path was specified, a tube with a given diameter was generated following this path. Implantation of the graft to the pre-interventional anatomy was then performed using Meshmixer. For implantation of bare metal stents aiming at straightening of vessel paths and enlarging the vessel cross sectional area, the center line of the stent was determined similarly to the vascular graft implantation. Then, a tube with a given length and diameter was generated following this center line. This tube was used as attractor and the vessel surface was deformed to match the stent orientation. Examples of these different procedures are shown in [Figure 2](#).

Numerical simulation of hepatic blood flow distribution

Simulation of patient-specific blood flow was performed using the finite volume CFD solver STAR-CCM+ (v15.4, Siemens PLM, Plano, TX, United States). The pre-interventional as well as virtually treated surface geometries were imported, and all truncated vessel openings were closed for subsequent definition of boundary conditions. At all vessels except the pulmonary arteries, a mass flow boundary condition was specified. Here, the average mass flow rate measured from the 2D VEC CMR was specified. For the LPA and RPA, outflow boundary conditions were applied, which allow the specification of the percentage of mass flow passing through these vessels. The ratio between LPA and RPA was calculated from the volume flow rate measurements in the respective vessels if available.

The vessel walls were assumed to be rigid, and a no-slip boundary condition was applied. Blood was modeled as non-Newtonian fluid with a shear-dependent viscosity described using a generalized Carreau-Yasuda model (29, 30) and a constant density of 1050 kg/m^3 .

A polyhedral mesh with a base size of 0.6 mm and a boundary layer consisting of four adjacent prism layers was generated. The overall thickness of the boundary layer was 30

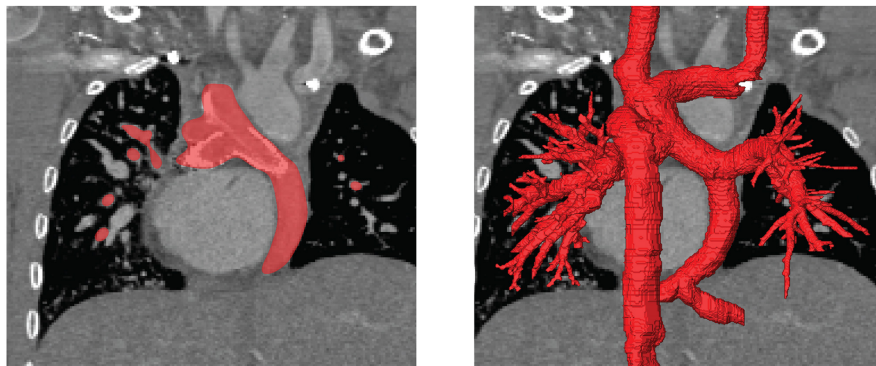


FIGURE 1

Illustration of the image-reconstruction procedure. Image voxels belonging to the region of interest were selected either manually or using semi-automatic approaches as for example region growing algorithms based on image intensity as well as local intensity gradients (**left**). This procedure was performed for all slices and all three reconstruction orientations, to obtain the three-dimensional label mask of the patient-specific anatomy (**right**).

percent of the base size with each prism layer's height being 30 percent larger than the previous one. No specific refinement regions were specified, but the meshing algorithm was able to automatically reduce the base size, as for example in regions featuring high curvatures.

Simulations were considered converged when static pressure values at the pulmonary artery outlets were stable and residuals of momentum and continuity were below 1e-5.

To calculate HFD, massless particles were seeded in the hepatic vein once the simulation was converged. Then, the simulation was continued until a stationary distribution of particles leaving the domain through LPA and RPA was achieved. In this study, HFD will be reported rounded to multiples of 5 percent (**Figure 3**).

Results

Patient characteristics

Patients' characteristics at baseline are depicted in **Table 1**. Due to an interrupted IVC, in two of three patients a Kawashima procedure had been performed. Right ventricular morphology of the systemic ventricle was present in two patients. Oxygen saturation levels were 81–83% at rest. Physical capacity was reduced in all patients according to cardiopulmonary exercise testing and New York Heart Association (NYHA) functional class ranged from II to III.

In one patient, re-routing surgery has already been performed meanwhile. Clinical follow-up examinations for this patient were performed 1 and 6 months after surgery and revealed good results in terms of improved physical capacity (now NYHA I) and oxygen saturation levels (currently 90% at rest).

Patient #1—Anatomy and hemodynamic considerations

This patient has a complex transposition of the great arteries with double outlet right ventricle, right ventricular hypoplasia and coarctation of the aorta. The medical history includes a banding of the pulmonary artery, an aortic arch patch augmentation, the creation of a bidirectional Glenn anastomosis and finally an extracardiac TCPC with fenestration, which has been closed by catheter intervention during follow-up. Due to significantly decline of oxygen saturation, invasive diagnostic assessment was performed revealing that the Fontan conduit with the hepatic venous flow is directed mainly to the left side of the lung and the right lower lobe, whereas the upper and middle right pulmonary lobe is supplied by the SVC alone (see **Figure 5**, top row). Consecutively, relevant macroscopically identifiable PAVM developed in the right upper and middle pulmonary lobe.

Patient #1—Image-based reconstruction of the patient-specific circulation

For this patient, reconstruction of the patient-specific circulation was performed using CT and CMR images (see **Figure 4**). In general, CT images allowed reconstruction of all relevant vessels but the proximal part of the LPA. Similar to the findings during angiography, the contrast agent administered during CT acquisition mainly reached the right upper and middle pulmonary lobe. Due to the lack of contrast agent in the proximal LPA as well as metallic artifacts of the aortic stent, neither the cross-section nor the orientation of the vessel could be discerned with

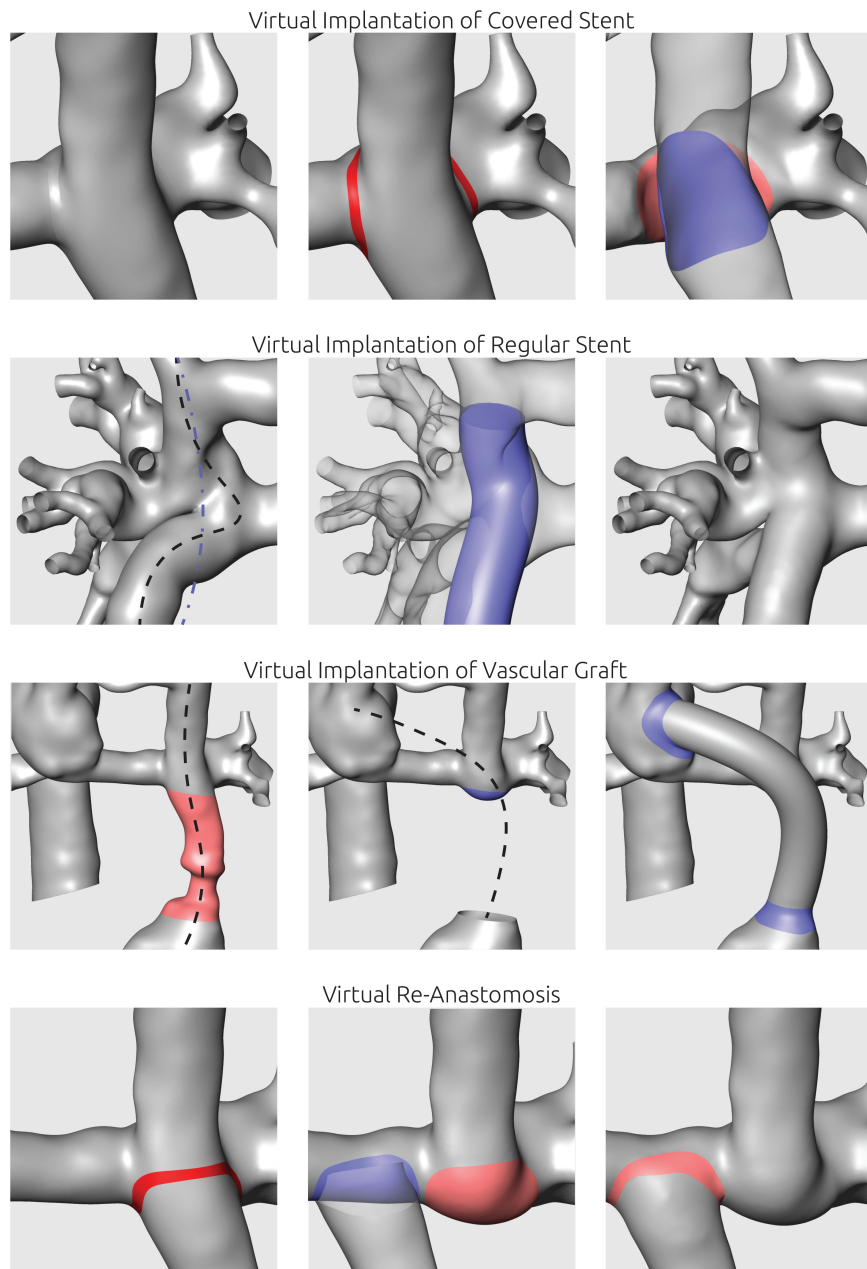


FIGURE 2

Illustration of virtual manipulations to mimic interventional or surgical procedures. Virtual implantation of covered stents was utilized to separate two vessel lumina. Virtual stent implantation aimed at straightening of curved vascular paths using a manually defined spline (blue line). To mimic surgical implantation of vascular grafts, the respective vessel section was replaced using a tube following a manually positioned centerline. For virtual re-anastomosis, vessels were separated and shifted to the new anastomosis site.

confidence. Here, CMR images were used to compensate the lack of information. The complex anatomy of the anastomosis between the Fontan conduit and the RPA could only be discerned from CT images using the Hounsfield unit gradient as orientation (see **Figure 4**, bottom right). Resolution of the CMR images was not sufficient to determine this anatomical detail.

Patient #1—Virtual treatment and hemodynamic simulations

The pre-interventional simulations match the clinical evaluations: 75% of the hepatic blood flow reaches the LPA, with the remaining fraction also perfusing the right lower pulmonary lobe. No perfusion of hepatic blood in the

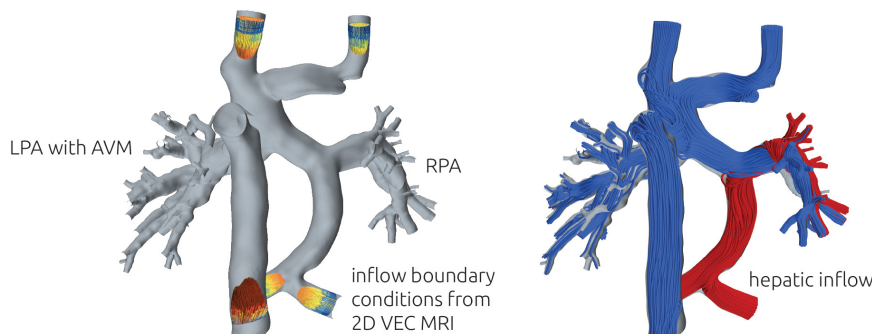


FIGURE 3

Illustration of the numerical setup (left). At all vessels except LPA and RPA, the patient-specific volume flow rate measured using 2D VEC CMR was specified as boundary conditions. 2D VEC CMR measurements at the LPA and RPA were used to specify the relative ratio of blood leaving the domain through each respective vessel. To illustrate the distribution of hepatic blood flow, streamlines of different color were seeded from the respective vessels (right). The example illustrates a total separation, with no hepatic blood (red) reaching the LPA.

right upper and middle pulmonary lobe was observed. The complex shape of the anastomosis between Fontan conduit and RPA seems to divert the blood from the IVC and the hepatic veins directly toward the LPA, while the blood flow from the SVC is oriented perpendicularly onto the wall of the Fontan conduit and directed toward the right upper and middle lobe.

For this patient, two surgical and one interventional treatment options were considered feasible. All options aimed at mitigating the effects of the complex anastomosis between Fontan conduit, the superior cavopulmonary anastomosis and RPA. The virtual changes in the patient-specific anatomy as well as the hemodynamic results in terms of streamlines and HFD mismatch are shown in **Figure 5** for all options.

As the first virtual surgical treatment option a translocation of the hepatic vein conduit toward the LPA was performed. Here, the main focus was to alter the angle and the bend of the anastomosis and to remove the flap-like structure between Fontan conduit and RPA. However, this intervention did not result in any relevant improvement of HFD mismatch, with 70% of the hepatic blood flowing to the LPA and the majority of the remaining hepatic blood still only reaching the right lower pulmonary lobe.

The second surgical option aimed at redirecting the SVC blood flow toward the LPA by re-anastomosis of the SVC to a position closer to the LPA. Thus, the SVC blood would not impinge on the wall of the Fontan conduit. This method resulted in an almost complete reversal of HFD, meaning that the LPA was now mainly perfused by the SVC, whereas the hepatic blood went almost entirely to the RPA, with only 10% reaching the LPA.

The interventional option aimed at straightening the connection from SVC to the Fontan conduit using a stent. Here, the idea was to anchor a stent in both vessels and to stretch the flap-like structure, which orients the hepatic blood flow toward the LPA, to construct a more perpendicular intersection

between the vessels. This intervention resulted in an even HFD toward LPA and RPA.

Patient #2—Anatomy and hemodynamic considerations

The second patient has an unbalanced atrioventricular septal defect, double outlet right ventricle, coarctation of the aorta, left persistent superior vena cava (LSVC), dextrocardia and interruption of the IVC with right-sided azygos continuity. Additionally, the patient has heterotaxy with left atrial isomerism and polysplenia. This complex anatomy was ultimately palliated by creating a bilateral superior cavopulmonary anastomosis (right-sided Kawashima and left-sided bi-directional Glenn anastomosis) with an extracardiac, left-sided hepatic vein conduit. Initially a fenestration was created, that was closed again several months later.

During follow-up, reduced physical capacity and declining oxygen saturation levels were observed and an invasive diagnostic assessment was performed. Next to a pronounced aneurysm that has formed at the junction of the azygos vein with the SVC, a significant stenosis in the central pulmonary artery between the RPA and LPA could be detected. Due to this fact, there was an almost exclusive flow from the left-sided hepatic vein conduit toward the LPA, whereas the RPA was only supplied by the right-sided Kawashima anastomosis (see **Figure 7** top row). Here, angiography revealed significant PAVM with oxygen saturation levels as low as 70% in the right pulmonary veins. However, to the implantation of a stent into the central pulmonary artery did not result in the redirection of hepatic blood toward the right side of the lung. Transcutaneous oxygen saturation levels are 83% at rest and decrease to 63% during physical exercise.

TABLE 1 Clinical summary of all patients.

	Patient #1	Patient #2	Patient #3
Patient characteristics at Fontan operation			
Age (years)	3.4	4.2	2.4
Sex	Female	Male	Male
Anatomical data			
Cardiac morphology	Complex DORV with ventricular imbalance	ubAVSD, DORV, CoA, LSVC, dextrocardia, interruption of the inferior vena cava with right-sided azygos continuity	ubAVSD, d-TGA, PS, LSVC, laevocardia, interruption of the inferior vena cava with left-sided hemiazygos continuity
Morphology of systemic ventricle	LV	RV	RV
Heterotaxy	No	Yes Left atrial isomerism, polysplenia	Yes Left atrial isomerism, polysplenia, situs inversus abdominalis
Surgical data			
Type of Fontan completion	Superior cavopulmonary anastomosis, extracardiac TCPC	Bilateral superior cavopulmonary anastomosis (right-sided Kawashima and bidirectional Glenn anastomosis, extracardiac hepatic vein conduit left-sided)	Bilateral superior cavopulmonary anastomosis (left-sided Kawashima and bidirectional Glenn anastomosis, extracardiac hepatic vein conduit right-sided)
Follow-up data			
FU-duration (years)	19.8	14.2	9.8
Age at last follow-up (years)	23.2	18.4	12.2
Weight at last follow-up (kg)	58	68	44
Height at last follow-up (cm)	163	176	148
BSA at last follow-up	1.6	1.8	1.4
NYHA I-IV at last follow-up	II	III	III
Hemoglobin at last follow-up (g/dl)	17.5	20.1	15.2
Oxygen saturation at rest	81	83	80
Hemodynamic data			
PAP (mmHg)	13	12.5	10
Site of PAVM	Right upper lobe	Right lung	Left lung
Residual shunts	PAVM	small venous collaterals, PAVM	PAVM
Implanted prosthetic material	Coils, Amplatzer septal occluder, CoA Stent	CoA Stent, peripheral stent graft (hepatic vein conduit), LPA-Stent	Coils, Amplatzer septal occluder, CoA Stent, RPA-Stent, LPA Stent

BSA, body surface area; CoA, aortic coarctation; DORV, double outlet right ventricle; d-TGA, right sided transposition of the great arteries; LSVC, left persistent superior vena cava; LV, left ventricle; NYHA, New York Heart Association; PAVM, intrapulmonary arteriovenous malformations; PS, pulmonary valve stenosis; RER, respiratory exchange ratio; RV, right ventricle; TCPC, total cavopulmonary connection; ubAVSD, unbalanced atrioventricular septal defect; VE/VCO₂ slope, slope of ventilation/carbon dioxide production ratio; VO₂ peak, peak oxygen uptake.

Patient #2—Image-based reconstruction of the patient-specific circulation

Similar to patient #1, image data from CT and CMR was required to reconstruct the entire TCPC. The reconstruction approach is shown in [Figure 6](#). During CT, the inflow of the contrast agent *via* the Glenn anastomosis did not reach the right part of the circulation, resulting in very poor contrast of the azygos vein, the SVC as well as the RPA. Especially the aneurysm which formed at the junction from SVC, LPA and azygos was not discernable. In contrast, the connection between the left and right side of the circulation was not discriminable within the CMR images due to susceptibility artifacts caused by the stent in the communicating area between LPA and RPA. However,

contrast in the CMR images allowed reconstruction of the right side of the circulation.

Patient #2—Virtual treatment and hemodynamic simulations

For this patient, two options for a combined surgical and interventional approach as well as one purely surgical approach were discussed. All approaches aimed at redirection of the hepatic blood flow toward the RSVC (right superior vena cava) and RPA. These treatment options as well as their predicted hemodynamic results are shown in [Figure 7](#).

The pre-interventional simulation agreed well with the angiographic assessment of HFD: The entirety of the inflow

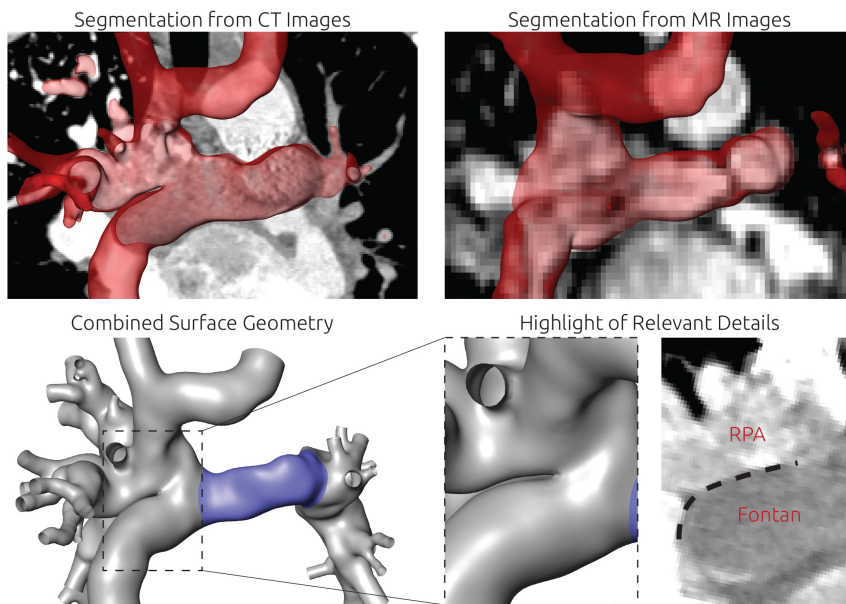


FIGURE 4

Detailed overview of the segmentation strategy for the first patient. The upper left and right panel show the segmentation from CT and CMR images, respectively. The lower left panel shows the final surface geometry that was reconstructed by combination of both segmentations. Tissue highlighted in blue was reconstructed from CMR images, whereas the remaining tissue was reconstructed from CT images. The lower right panel highlights the complex connection between RPA, SVC, and Fontan conduit, which could only be discriminated in CT images due to the distinct Hounsfield gradient from Fontan conduit to RPA.

from the hepatic vein conduit flowed to the LPA. The LPA was also perfused by the majority of the blood deriving from the LSVC. Similarly, the majority of the blood flow from the azygos vein and the RSVC flowed toward the RPA.

Both approaches using surgical as well as interventional techniques were similar in the main approach: using a covered stent, the hepatic vein conduit could be separated from the LPA, resulting in a direct connection between LSVC and the hepatic vein conduit. As the innominate vein connecting LSVC and RSVC in this patient is very hypoplastic, its diameter was considered insufficient to conduct the blood flow coming from LSVC and the hepatic vein conduit toward the RSVC. Thus, the innominate vein was intended to be replaced using a vascular graft with a diameter of 16 mm.

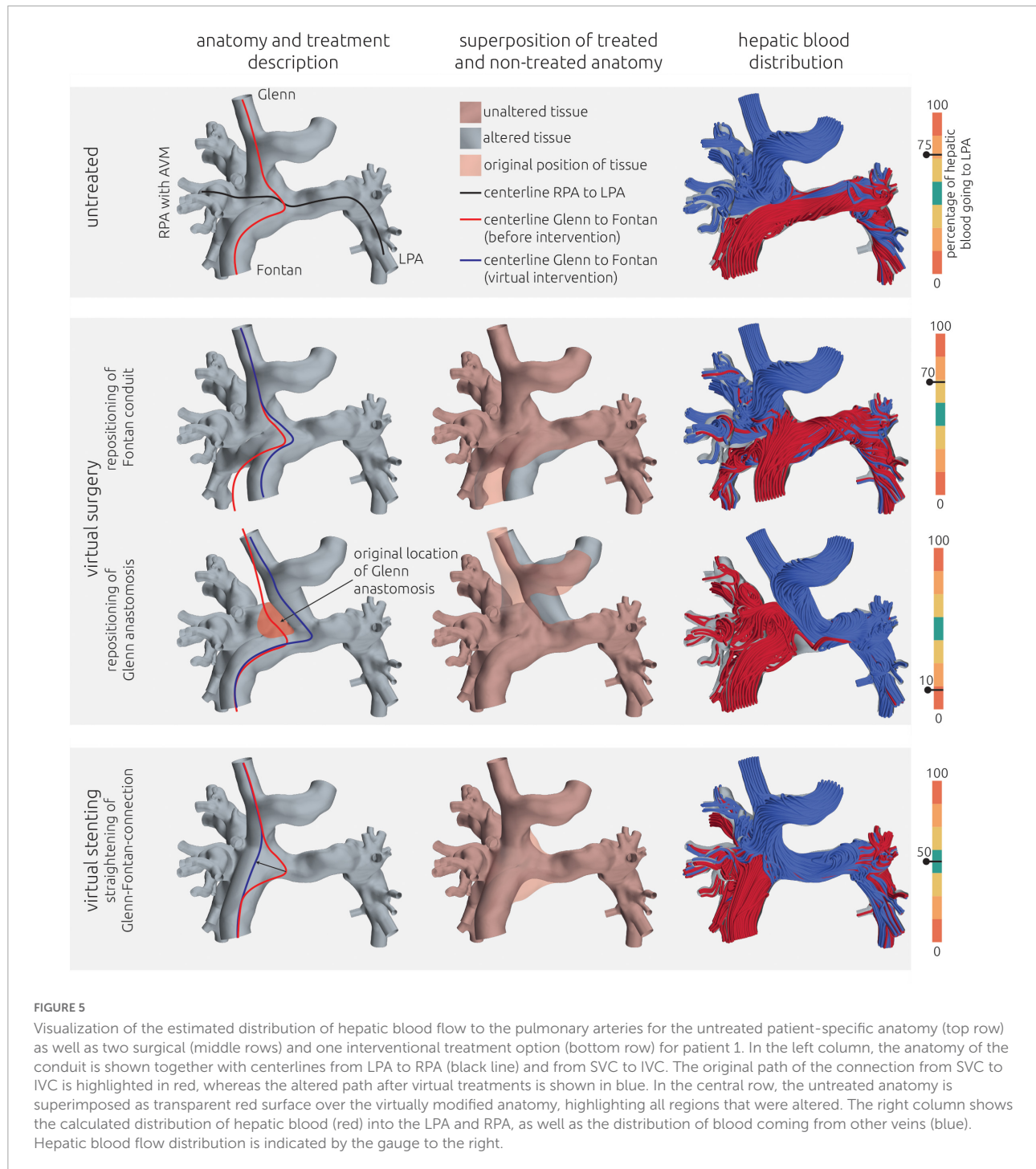
Additionally, a reduction of the aneurysm at the junction of azygos vein, RSVC and RPA was discussed, subsequently modeled, and simulated as second treatment option. The possible flow directions of blood coming from the hepatic vein conduit are depicted in **Figure 7** compared to the original blood flow directions to illustrate the intended redirection of blood flow.

Both methods resulted in similar virtual post-interventional hemodynamics. The HFD was almost entirely reversed, meaning that most of the blood from the hepatic vein conduit was directed toward the RPA. Resizing of the aneurysm further enhanced this effect from 20% of the hepatic blood reaching the LPA to only 5%.

Additionally, an entire surgical approach was discussed. Here the Fontan conduit was to be disconnected from the LPA, whereas the connection between LSVC and LPA remained. Then, a vascular graft with a diameter of 20 mm was intended to be used to connect the hepatic veins directly with the aneurysm at the Kawashima anastomosis. The path of this vascular graft was determined using the volumetric CT information to ensure that neither structures of the heart nor the lungs were compressed. Even though inflow from the LSVC still was directed mainly to the LPA, this strategy resulted in a sufficiently even HFD of 40%.

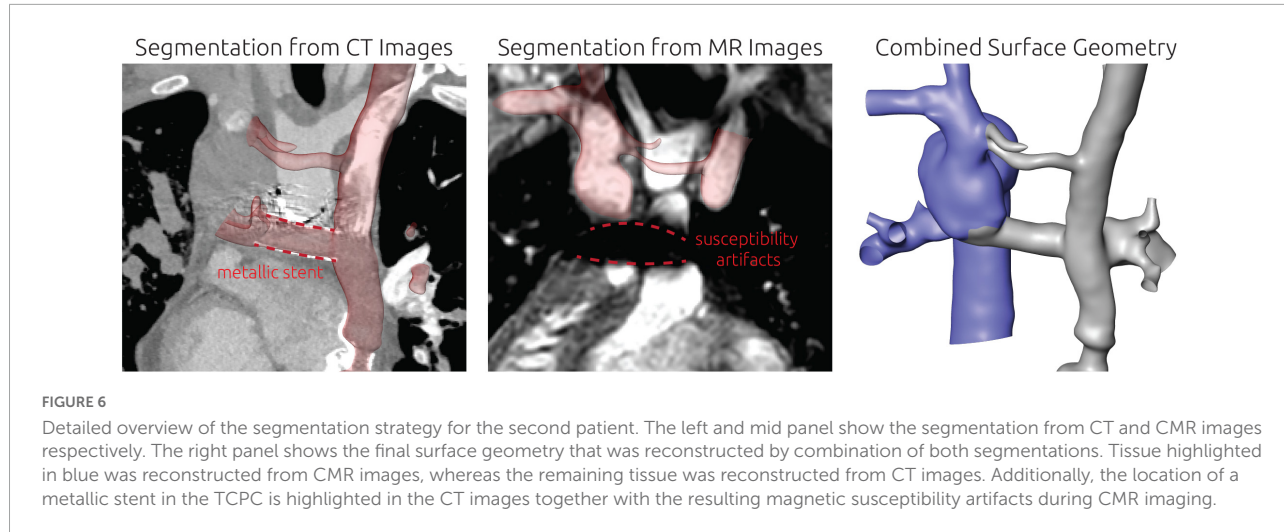
Patient #3—Anatomy and hemodynamic considerations

The third patient has an unbalanced atrioventricular septal defect with dominant right ventricle, d-transposition of the great arteries, pulmonary stenosis, LSVC, and interruption of the IVC with left-sided hemiazygos continuity, heterotaxy with left atrial isomerism, polysplenia and situs inversus abdominalis. This complex anatomy was surgically palliated by creating a bilateral superior cavopulmonary anastomosis (left-sided Kawashima and bidirectional Glenn anastomosis) with an extracardiac right-sided hepatic vein conduit. Several cardiac catheterizations



with embolization of hemodynamic relevant venous collaterals became necessary during follow-up. Additionally, multiple interventions with balloon dilatations and ultimately stent implantations in the RPA and LPA, due to stenoses in both vessels had to be performed. CMR-based flow measurements and angiography showed that the hepatic blood is mainly directed toward the RPA, whereas blood

from the azygos vein, which is connected to the SVC shortly above its junction with the LPA, and blood from the upper half of the body is mainly directed to the LPA (see **Figure 9** top row). Consecutively, relevant left-sided PAVM developed. Transcutaneous oxygen saturation values are approximately 80% at rest and decreased to 72% during physical exercise.



Patient #3—Image-based reconstruction of the patient-specific circulation

For this patient, the entire patient-specific anatomy was reconstructed using CT image data. As metallic stents were present in both LPA and RPA, the majority of the circulation of interest was not discriminated in CMR images due to susceptibility artifacts. While these stents also caused artifacts in the CT images, their contours were perfectly visible, allowing accurate reconstruction of the intricate connection between azygous vein, Glenn, and LPA, which is highlighted in the bottom right panel of [Figure 8](#).

Patient #3—Virtual treatment and hemodynamic simulations

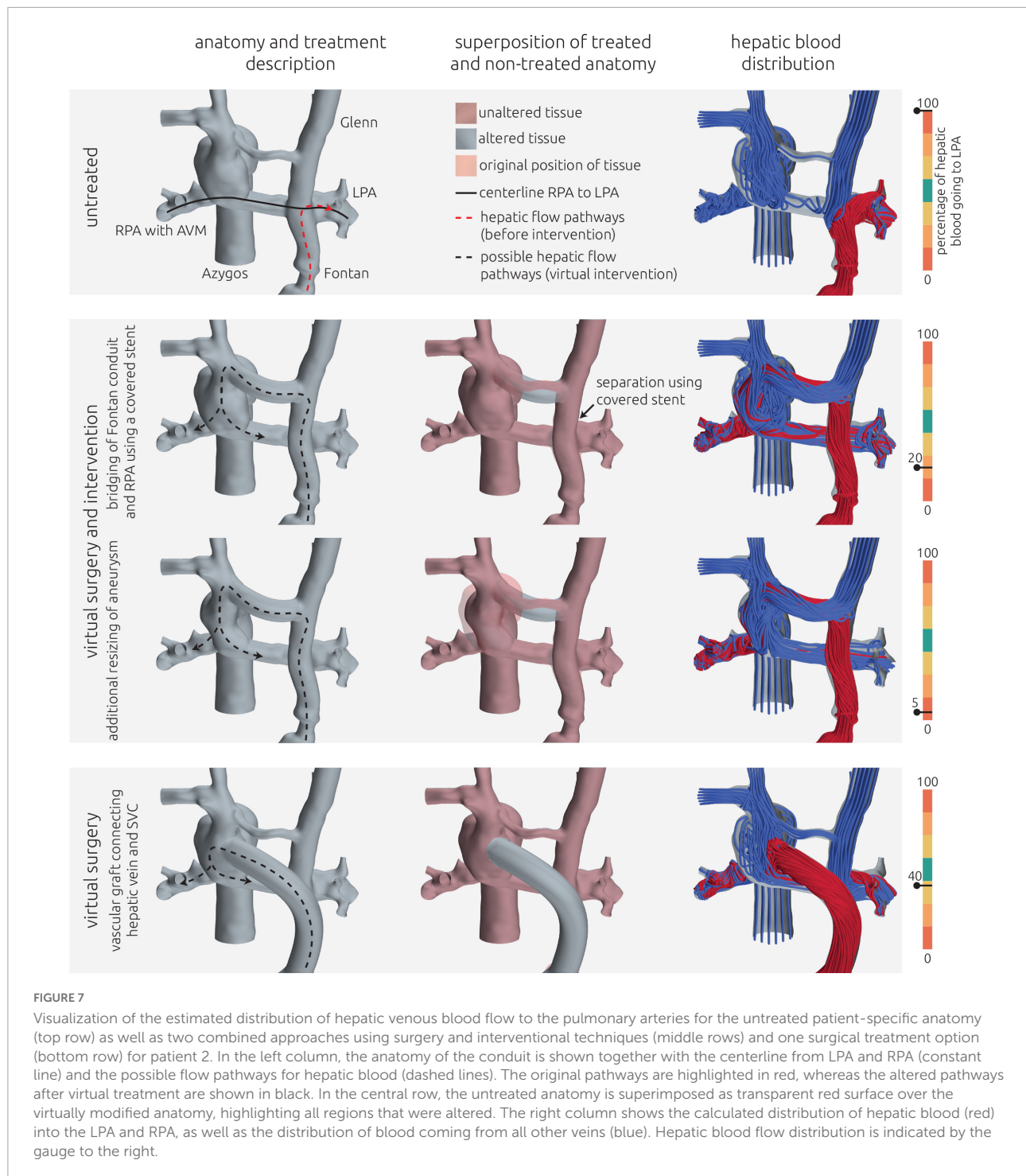
Also in this case, the pre-interventional simulation confirmed angiographic information obtained earlier (see [Figure 9](#), top panel) with regard to distribution of hepatic blood.

Since the patient suffered from pronounced cyanosis and severely limited exercise capacity (NYHA functional class III) with signs of progressive heart failure, the indication for rerouting surgery was made. Due to the anatomical conditions, only one treatment option was considered feasible by the interdisciplinary Heart Team. This option was to re-route the hepatic vein conduit to the innominate vein (see [Figure 9](#) middle and bottom row). The aim of this treatment option was to join all incoming blood flows and allow mixing of the hepatic blood before entering the pulmonary vasculature. While an improvement in HFD could be achieved in the virtual surgery planning, still only 5% of the hepatic blood was predicted to flow toward the LPA by the simulation.

However, in lack of alternative options, this surgical intervention was performed nonetheless on the patient and a 1-month follow-up including CMR assessment was performed. Using this CMR information, a comparison of the postoperative result with the preoperative model was performed. The conduit graft that was implanted to connect the hepatic veins with the innominate vein was reconstructed and merged with the pre-interventional reconstruction to obtain a digital representation of the real intervention. Minor differences in the orientation of the vascular graft as well as its anastomosis site to the innominate vein were observed compared to the virtual treatment. Additionally, 2D VEC CMR measurements were available from the follow-up measurements and were used as boundary conditions for simulation of the real surgical outcome. While the anatomy is very similar between real and virtual surgery, the real surgery resulted in an improved HFD with 20% reaching the LPA. The calculated hemodynamics of the virtual intervention and the real intervention using the follow-up information are shown in [Figure 9](#).

Discussion

In this study, methods for virtual treatment planning for interventional or surgical correction of Fontan patients were evaluated using routine data available for three patients suffering from severe cyanosis due to pronounced PAVM. All patients had a complex treatment history, resulting in multiple metallic implants in the Fontan circulation as well as neighboring vessels. Due to the resulting metallic artifacts as well as the complex anatomy of anastomosis sites, CT data was required to reconstruct the patient-specific anatomy, as it offered well-resolved image information for accurate reconstruction. However, in two cases additional information from CMR images was required to adequately reconstruct the complete Fontan

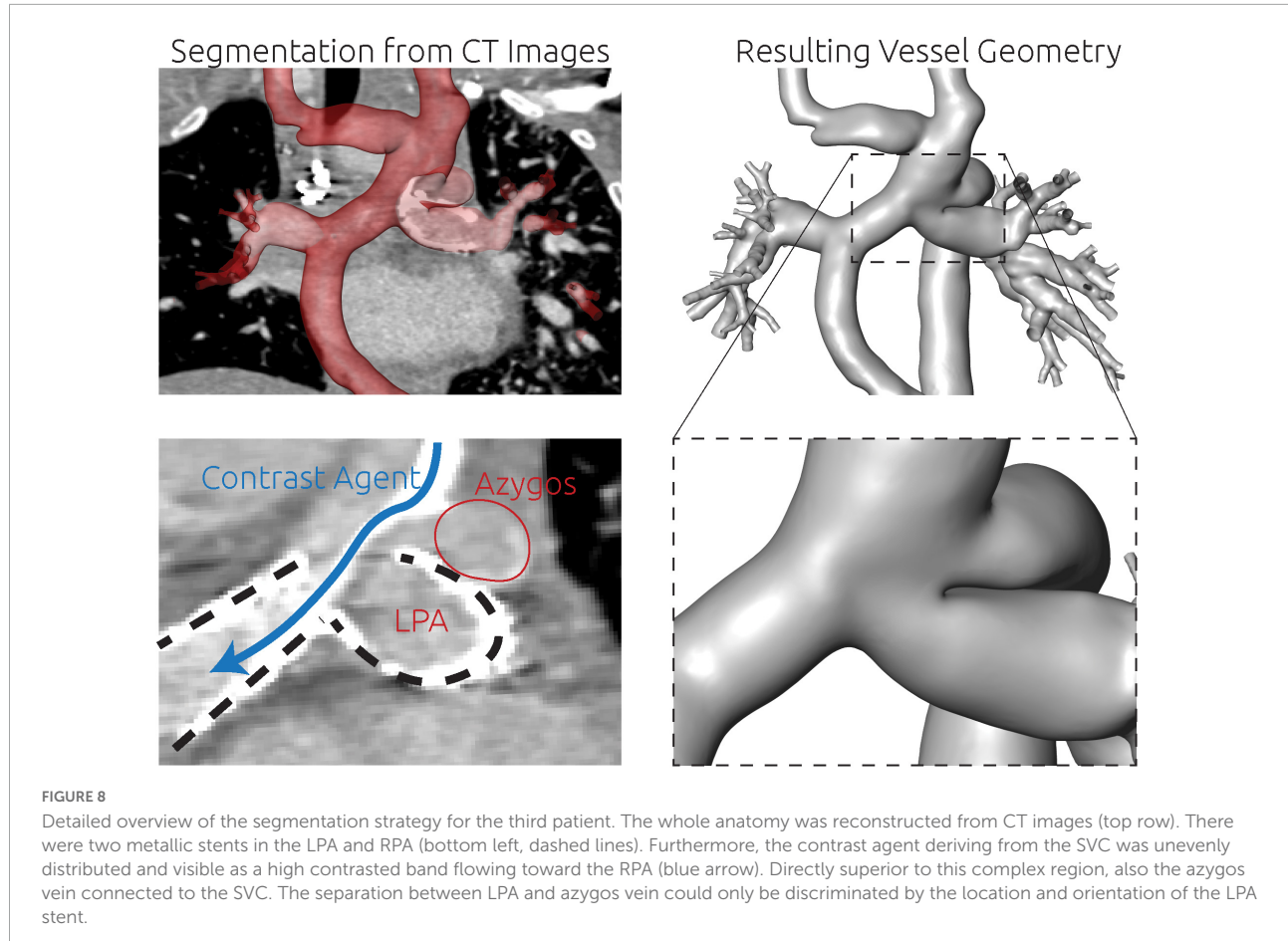


circulation, as CT contrast was poor in some regions due to the uneven distribution of contrast agent as well as artifacts caused by metallic stents.

Simulation of pre-interventional hemodynamics confirmed angiographic assessment in all three cases and revealed hepatic blood flowing entirely to the pulmonary arteries without PAVM. These findings are consistent with the proposed mechanism

between HFD and development of PAVM and further support previous studies, suggesting that numerical assessment of pre-interventional hemodynamics in Fontan circulation is feasible (20).

During interdisciplinary Heart Team meetings, at least one surgical, interventional, or combined treatment option was identified that was considered technically feasible and



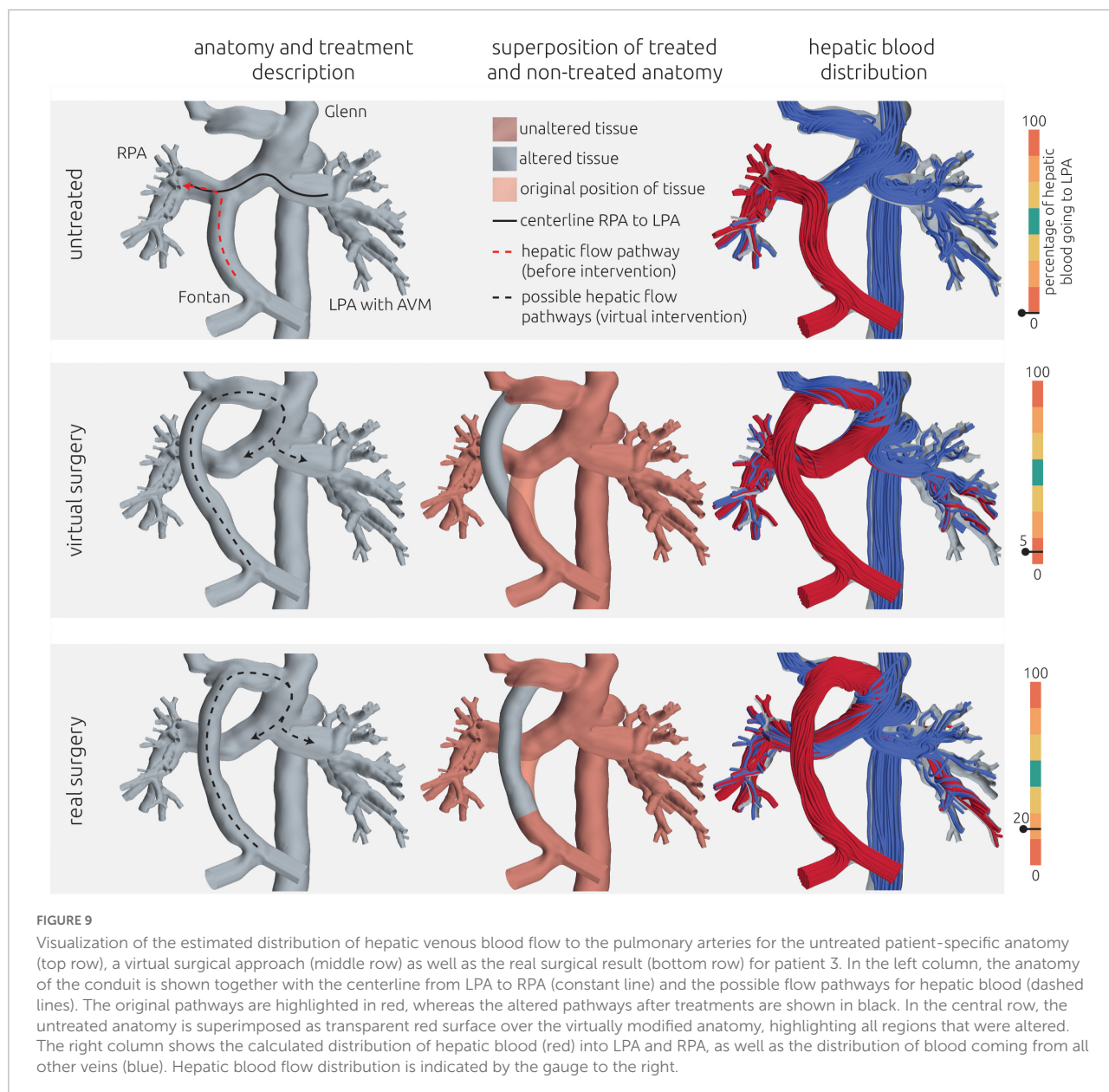
resulted in an improvement of HFD by virtual intervention. However, also treatment options with undesirable outcome, as for example entire reversal of HFD in patient #1 and #2, where the hepatic blood would flow almost exclusively toward the pulmonary arteries with PAVM, were identified. While even in those cases, a fraction of hepatic blood would reach the other pulmonary arteries, these findings highlight the advantages of pre-interventional virtual therapy planning as outcomes cannot be predicted intuitively. In the third patient, the only viable treatment option resulted only in moderate redirection of hepatic blood flow in the virtual and real surgery respectively. Even though the HFD was still predominantly biased toward the LPA, improvement of oxygen saturation could be observed in both follow-up examinations 1 and 6 months postoperatively. This suggests that already small improvements of HFD can be sufficient for regression of PAVM.

Implications for the reliability of surgical planning

To date, there is promising but limited data on experience of virtual Fontan surgical planning. In its current state, virtual

surgical planning was demonstrated to assess preoperative hemodynamic conditions, to identify anatomical constraints for potential surgical options, and to produce descent postoperative predictions if boundary conditions are similar enough between pre- and postoperative anatomy (20, 22, 31–33).

While Sundareswaran et al. were the first describing the use of surgical planning to correct PAVM in 2009, their work focusses on a single case report without postoperative imaging data to validate their simulated predictions (34). In 2012, Haggerty et al. successfully compared HFD between the predicted and post-operative states for four patients (25). Trusty et al. finally conducted the first prospective Fontan surgical follow-up study analyzing the accuracy of surgical planning based on 12 Fontan patients in 2019 (21). They published one of the largest patient cohorts and have many years of experience in this field of research, however, they also emphasize the need for sufficient imaging quality as one of the most essential prerequisites for accurate treatment planning. In this context it is the purpose of our work to demonstrate methodological approaches to also integrate complex cases with artifact-rich imaging as exactly these patients might benefit the most from interdisciplinary virtual therapy planning approaches.



There certainly is the need for further follow-up and thorough validation studies to encourage the translation of virtual therapy planning into the clinical routine. However, our data demonstrates that virtual therapy planning might have the potential to be a useful tool for single ventricle virtual therapy planning with the ability to deliver clinically relevant patient individual treatment options.

A relevant next step is the evaluation of how accurately a virtually planned treatment, either surgical or interventional, can be realized in reality. Several aspects, as for example the skill of the surgeon or cardiologist performing the treatment, intraprocedural complications or model uncertainties can and will affect the virtual and the real treatment. Thus, more data

on how accurately a real intervention can be modeled *in silico* is required, as these uncertainties, such as in the angle or site of an anastomosis, might also have an effect on hemodynamic parameters such as HFD.

Finally, the assessment of viability of a given treatment strategy was mainly based on the experience of the heart team member in favor of the respective treatment, a general discussion, as well as some anatomical aspects as described in the methods section. A quantitative assessment of the procedural risk or chances of success, at least by independent rating by several members of the heart team, should be envisaged to allow to weigh the risks against the expected outcomes of different treatment strategies.

Importance of sufficient image data quality and hybrid imaging approaches

According to Trusty et al., accurate prediction of the anatomy is one of the most important aspects to improve the accuracy of virtual prediction of HFD (21). In this study, accurate assessment of the entire anatomy of the TCPC using cardiovascular imaging was challenging in all three patients due to the presence of metallic artifacts which affected CMR as well as CT images. Furthermore, not only was a pronounced mismatch of HFD observed, but also the contrast agent administered during CT examination went predominantly to the pulmonary segments affected by PAVM, resulting in poor contrast in the unaffected sites. However, in general the CT images were superior for assessment of the patient-specific anatomy especially due to the high resolution and the ability to discern the metallic stents reasonably well. Especially the complex anastomosis sites of the Fontan conduit in patient #1 and of the azygos vein in patient #3 could not have been reconstructed from CMR images alone. Nonetheless, CMR images are mandatory for the approach to work, as patient-specific boundary conditions in all vessels are required to ensure reliable simulation results (20, 32). While most studies rely on CMR images for reconstruction of the patient-specific anatomy as well, these studies often focus on younger patients with less complex anatomical conditions, in whom implantation of different metallic artifacts has not yet been necessary (20). For complex cases as investigated in this study, additional acquisition of CT images might be necessary to assess the entire anatomy of the TCPC. While this procedure comes at the cost of exposure to ionizing radiation, the CT images were already valuable for surgical treatment-planning even without the virtual treatment-planning.

Feedback from the cooperation between heart team members and the biomedical engineers

Even without the simulation of patient-specific hemodynamics before or after virtual intervention, the reconstruction of the patient-specific anatomy of the TCPC was already considered helpful for understanding the anatomical constraints and discussion of possible treatment strategies. Especially for the first two patients, where both image modalities were required to reconstruct the anatomy, the 3D model could be superimposed to either image data, enhancing their interpretability. For example, possible anastomosis sites and conduit orientations could be planned by replacing non-visible regions using the 3D model, which allowed to discriminate the location of the TCPC from surrounding cardiovascular structures or lung tissue.

Also, the pre-interventional simulation results were already seen as helpful for determination of treatment strategies, as they allowed investigation of the overall TCPC hemodynamics rather than investigation of isolated aspects of the flow by means of angiographic videos. These simulations also helped building trust in the general method, as they agreed well with the location of PAVM as well as angiographic findings.

Limitations

This study is based on only three patients with a similar clinical background. While the anatomies and treatment histories of the patients differ widely, this sample size does not allow for general assumptions. However, the aim of this study was to demonstrate a proof-of-concept prediction of HFD in Fontan patients with PAVM and an extensive treatment history.

A quasi-steady numerical model was used, and all vessels were assumed to be rigid. The latter model assumption was chosen because the TCPC in this study featured different materials as vessel tissue, metallic stents, and vascular grafts, as well as scar tissue from previous surgeries, which would require combination of different constitutive models for which no data for parametrization was available. Previous studies suggest that the use of rigid walls is valid for time-averaged assessment of parameters such as HFD (35). However, for other aspects as for example the estimation of the energy or power loss in the TCPC, or the prediction of vascular remodeling at mid- to long-term this assumption might not be sufficient. Thus, identifying methods to parametrize patient-specific tissue properties, or at least assess whether tissue properties can be assumed based on general demographics in a sufficient manner, should be envisaged.

Virtual treatment strategies were only evaluated with regard to HFD optimization. No energetic aspects as pressure, or energy loss were investigated, which might result in conflicting recommendations (36). However, desaturation resulting from PAVM was the major clinical symptom in all patients, thus, optimization of HFD was considered the major aim for surgical or endovascular treatment.

Commonly, lumped parameter models are used to specify boundary conditions for parts of the TCPC. In this study, we only used 2D VEC CMR measurements to specify all boundary conditions. The good agreement between clinical examinations and the pre-interventional simulations support, that this choice of boundary conditions is also viable. However, this model does not allow to predict post-intervention changes in either flow rates or resistances. This becomes apparent by the HFD mismatch between the virtual and real treatment outcome in patient #3. While the anatomies of both simulations were very similar, the predicted HFD was only 5%, whereas the real HFD

was 20%. However, if a treatment results in remodeling of PAVM, significant changes in the vascular resistance are to be expected. As this resistance is usually used for parametrization of lumped parameter models, those approaches might be suitable to assess hemodynamics assuming remodeling of PAVM by increasing vascular resistance accordingly.

Conclusion

In silico assessment of the HFD before and after virtual treatment might allow to optimize patient-specific therapy planning in patients with pronounced hepatic flow mismatch and PAVM. However, this approach still requires intensive efforts with respect to validation and standardization before translation to clinical routine can be envisaged.

Data availability statement

The raw data supporting the conclusions of this article will be made available by the authors, without undue reservation.

Ethics statement

The studies involving human participants were reviewed and approved by Ethikkommission der Charité-Universitätsmedizin Berlin. Written informed consent to participate in this study was provided by the participants or their legal guardian/next of kin.

References

1. Fontan F, Baudet E. Surgical repair of tricuspid atresia. *Thorax*. (1971) 26:240–8. doi: 10.1136/thx.26.3.240
2. Khairy P, Fernandes SM, Mayer JE Jr., Triedman JK, Walsh EP, Lock JE, et al. Long-term survival, modes of death, and predictors of mortality in patients with Fontan surgery. *Circulation*. (2008) 117:85–92. doi: 10.1161/CIRCULATIONAHA.107.738559
3. Kogon B. Is the extracardiac conduit the preferred Fontan approach for patients with univentricular hearts? The extracardiac conduit is the preferred Fontan approach for patients with univentricular hearts. *Circulation*. (2012) 126:2511–5. doi: 10.1161/CIRCULATIONAHA.111.076398
4. Schafstedde M, Nordmeyer S, Schleiger A, Nordmeyer J, Berger F, Kramer P, et al. Persisting and reoccurring cyanosis after Fontan operation is associated with increased late mortality. *Eur J Cardiothorac Surg*. (2021) 61:54–61. doi: 10.1093/ejcts/ezab298
5. Cloutier A, Ash JM, Smallhorn JF, Williams WG, Trusler GA, Rowe RD, et al. Abnormal distribution of pulmonary blood flow after the Glenn shunt or fontan procedure: Risk of development of arteriovenous fistulae. *Circulation*. (1985) 72:471–9. doi: 10.1161/01.CIR.72.3.471
6. Kavarrana MN, Jones JA, Stroud RE, Bradley SM, Ikonomidis JS, Mukherjee R. Pulmonary arteriovenous malformations after the superior cavopulmonary shunt: Mechanisms and clinical implications. *Expert Rev Cardiovasc Ther*. (2014) 12:703–13. doi: 10.1586/14779072.2014.912132
7. Shinohara T, Yokoyama T. Pulmonary arteriovenous malformation in patients with total cavopulmonary shunt: What role does lack of hepatic venous blood flow to the lungs play?. *Pediatr Cardiol*. (2001) 22:343–6. doi: 10.1007/s002460010243
8. Lee J, Menkis AH, Rosenberg HC. Reversal of pulmonary arteriovenous malformation after diversion of anomalous hepatic drainage. *Ann Thorac Surg*. (1998) 65:848–9. doi: 10.1016/S0003-4975(98)00011-3
9. Duncan BW, Desai S. Pulmonary arteriovenous malformations after cavopulmonary anastomosis. *Ann Thorac Surg*. (2003) 76:1759–66. doi: 10.1016/S0003-4975(03)00450-8
10. Srivastava D, Preminger T, Lock JE, Mandell V, Keane JF, Mayer JE Jr., et al. Hepatic venous blood and the development of pulmonary arteriovenous malformations in congenital heart disease. *Circulation*. (1995) 92:1217–22. doi: 10.1161/01.CIR.92.5.1217
11. Knight WB, Mee RB. A cure for pulmonary arteriovenous fistulas?. *Ann Thorac Surg*. (1995) 59:999–1001. doi: 10.1016/0003-4975(94)00735-P
12. Pike NA, Vricella LA, Feinstein JA, Black MD, Reitz BA. Regression of severe pulmonary arteriovenous malformations after fontan revision and "hepatic factor" rerouting. *Ann Thorac Surg*. (2004) 78:697–9. doi: 10.1016/j.athoracsur.2004.02.003

Author contributions

MS, PY, SN, NS, and JB: data curation. MS, PY, and JB: formal analysis. MS, PY, PK, AS, FB, JP, YM, M-YC, SO, and JB: methodology. MS and JB: supervision. JB: visualization. MS, PK, and JB: writing – original draft. All authors contributed to the conceptualization, investigation, writing – review and editing, and approved the submitted version.

Funding

MS was participant in the BIH-Charite Digital Clinician Scientist Program funded by the Charité–Universitätsmedizin Berlin and the Berlin Institute of Health.

Conflict of interest

The authors declare that the research was conducted in the absence of any commercial or financial relationships that could be construed as a potential conflict of interest.

Publisher's note

All claims expressed in this article are solely those of the authors and do not necessarily represent those of their affiliated organizations, or those of the publisher, the editors and the reviewers. Any product that may be evaluated in this article, or claim that may be made by its manufacturer, is not guaranteed or endorsed by the publisher.

13. Justino H, Benson LN, Freedom RM. Development of unilateral pulmonary arteriovenous malformations due to unequal distribution of hepatic venous flow. *Circulation*. (2001) 103:E39–40. doi: 10.1161/01.CIR.103.8.e39
14. Wu IH, Nguyen KH. Redirection of hepatic drainage for treatment of pulmonary arteriovenous malformations following the fontan procedure. *Pediatr Cardiol*. (2006) 27:519–22. doi: 10.1007/s00246-006-1261-z
15. Kim SJ, Bae EJ, Lee JY, Lim HG, Lee C, Lee CH. Inclusion of hepatic venous drainage in patients with pulmonary arteriovenous fistulas. *Ann Thorac Surg*. (2009) 87:548–53. doi: 10.1016/j.athoracsur.2008.10.024
16. Arrigoni SC, van den Heuvel F, Willems TP, Hillege H, Lindberg HL, Berger RM, et al. Off-pump hepatic to azygos connection via thoracotomy for relief of fistulas after a Kawashima procedure: Ten-year results. *J Thorac Cardiovasc Surg*. (2015) 149:1524–30. doi: 10.1016/j.jtcvs.2015.02.049
17. Kaulitz R, Ziemer G, Hofbeck M. Off-pump direct hepatic veins-to-hemiazygos vein anastomosis after primary Kawashima operation: Long-term result. *Cardiol Young*. (2021) 31:1340–2. doi: 10.1017/S1047951121000421
18. de Zélicourt DA, Haggerty CM, Sundareswaran KS, Whited BS, Rossignac JR, Kanter KR, et al. Individualized computer-based surgical planning to address pulmonary arteriovenous malformations in patients with a single ventricle with an interrupted inferior vena cava and azygous continuation. *J Thorac Cardiovasc Surg*. (2011) 141:1170–7. doi: 10.1016/j.jtcvs.2010.11.032
19. Trusty PM, Wei Z, Sales M, Kanter KR, Fogel MA, Yoganathan AP, et al. Y-graft modification to the Fontan procedure: Increasingly balanced flow over time. *J Thorac Cardiovasc Surg*. (2020) 159:652–61. doi: 10.1016/j.jtcvs.2019.06.063
20. Trusty PM, Slesnick TC, Wei ZA, Rossignac J, Kanter KR, Fogel MA, et al. Fontan surgical planning: Previous accomplishments, current challenges, and future directions. *J Cardiovasc Transl Res*. (2018) 11:133–44. doi: 10.1007/s12265-018-9786-0
21. Trusty PM, Wei ZA, Slesnick TC, Kanter KR, Spray TL, Fogel MA, et al. The first cohort of prospective fontan surgical planning patients with follow-up data: How accurate is surgical planning? *J Thorac Cardiovasc Surg*. (2019) 157:1146–55. doi: 10.1016/j.jtcvs.2018.11.102
22. van Bakel TMJ, Lau KD, Hirsch-Romano J, Trimarchi S, Dorfman AL, Figueroa CA. Patient-specific modeling of hemodynamics: Supporting surgical planning in a fontan circulation correction. *J Cardiovasc Transl Res*. (2018) 11:145–55. doi: 10.1007/s12265-017-9781-x
23. Warmerdam E, Krings GJ, Leiner T, Grotenhuis HB. Three-dimensional and four-dimensional flow assessment in congenital heart disease. *Heart*. (2020) 106:421–6. doi: 10.1136/heartjnl-2019-315797
24. Siallagan D, Loke YH, Olivieri L, Opfermann J, Ong CS, de Zélicourt D, et al. Virtual surgical planning, flow simulation, and 3-dimensional electrospinning of patient-specific grafts to optimize Fontan hemodynamics. *J Thorac Cardiovasc Surg*. (2018) 155:1734–42. doi: 10.1016/j.jtcvs.2017.11.068
25. Haggerty CM, de Zélicourt DA, Restrepo M, Rossignac J, Spray TL, Kanter KR, et al. Comparing pre- and post-operative fontan hemodynamic simulations: Implications for the reliability of surgical planning. *Ann Biomed Eng*. (2012) 40:2639–51. doi: 10.1007/s10439-012-0614-4
26. Montesa C, Karamlou T, Ratnayaka K, Pophal SG, Ryan J, Nigro JJ. Hepatic vein incorporation into the azygos system in heterotaxy and interrupted inferior vena cava. *World J Pediatr Congenit Heart Surg*. (2019) 10:330–7. doi: 10.1177/2150135119842869
27. Lorensen WE, Cline HE. Marching cubes: A high resolution 3D surface construction algorithm. *SIGGRAPH Comput Graph*. (1987) 21:163–9. doi: 10.1145/37402.37422
28. Kuprat A, Khamayseh A, George D, Larkey L. Volume conserving smoothing for piecewise linear curves, surfaces, and triple lines. *J Comput Phys*. (2001) 172:99–118. doi: 10.1006/jcph.2001.6816
29. Karimi S, Dabagh M, Vasava P, Dadvar M, Dabir B, Jalali P. Effect of rheological models on the hemodynamics within human aorta: CFD study on CT image-based geometry. *J NonNewton Fluid Mech*. (2014) 207:42–52. doi: 10.1016/j.jnnfm.2014.03.007
30. Guissard N, Reiles F. Effects of static stretching and contract relax methods on the force production and jump performance. *Comput Methods Biomed Eng Biomed Eng*. (2005) 8:127–8. doi: 10.1080/10255840512331388588
31. Fogel MA, Khiabani RH, Yoganathan A. Imaging for preintervention planning: Pre- and post-Fontan procedures. *Circ Cardiovasc Imaging*. (2013) 6:1092–101. doi: 10.1161/CIRCIMAGING.113.000335
32. Slesnick TC, Yoganathan AP. Computational modeling of Fontan physiology: At the crossroads of pediatric cardiology and biomedical engineering. *Int J Cardiovasc Imaging*. (2014) 30:1073–84. doi: 10.1007/s10554-014-0442-8
33. de Zélicourt DA, Marsden A, Fogel MA, Yoganathan AP. Imaging and patient-specific simulations for the Fontan surgery: Current methodologies and clinical applications. *Prog Pediatr Cardiol*. (2010) 30:31–44. doi: 10.1016/j.ppedcard.2010.09.005
34. Sundareswaran KS, de Zélicourt D, Sharma S, Kanter KR, Spray TL, Rossignac J, et al. Correction of pulmonary arteriovenous malformation using image-based surgical planning. *JACC Cardiovasc Imaging*. (2009) 2:1024–30. doi: 10.1016/j.jcmg.2009.03.019
35. Tang E, Wei Z, Fogel MA, Veneziani A, Yoganathan AP. Fluid-structure interaction simulation of an intra-atrial fontan connection. *Biology*. (2020) 9:412. doi: 10.3390/biology9120412
36. de Zélicourt DA, Kurtcuoglu V. Patient-specific surgical planning, where do we stand? The example of the fontan procedure. *Ann Biomed Eng*. (2016) 44:174–86. doi: 10.1007/s10439-015-1381-9

3.4 Optimierung: Einsatz von künstlicher Intelligenz anstelle computergestützter Strömungssimulationen für eine bessere klinische Translation

Dass bildbasierte Simulationsverfahren in der Klinik angewendet werden können und das Potential bieten, die patientenspezifische Therapieplanung zu verbessern, wurde in der zuvor vorgestellten Studie gezeigt. Allerdings erfordern sie eine hohe technische Expertise und sind sehr zeit- und rechenleistungsintensiv. Für eine bessere klinische Translation wurde daher in einem nächsten Schritt ein weiterer Modellierungsansatz vorgestellt, der auf dem Einsatz von Künstlicher Intelligenz (KI) beruht und das Ziel hat, die konkrete Anwendung von bildbasierter Modellierung und Therapieplanung im klinischen Alltag zu erleichtern.

Modelling Blood Flow in Patients with Heart Valve Disease using Deep Learning: A computationally efficient Method to expand diagnostic Capabilities in clinical Routine

Pavlo Yevtushenko, Leonid Goubergrits, Benedikt Franke, Titus Kühne, **Marie Schafstedde**

Der nachfolgende Text entspricht inhaltlich dem Abstrakt der oben genannten Publikation als Übersetzung durch die Autorin:

*„Die computergestützte Modellierung des Blutflusses liefert wichtige hämodynamische Parameter für Diagnose und Therapieplanung von Patient*innen mit Herzklappenerkrankungen. Die meisten der vorgeschlagenen Lösungen zur Diagnose und/oder Behandlungsunterstützung auf der Grundlage von Flusssimulationen verwenden jedoch zeit- und ressourcenintensive computergestützte Simulationsverfahren (CFD) und sind daher in der klinischen Praxis nur schwer zu implementieren. Im Gegensatz dazu liefern Deep-Learning-Algorithmen (DL) ihre Ergebnisse schnell und ohne große Rechenleistung. Daher könnte die Modellierung des Blutflusses mit DL anstelle von CFD die Anwendbarkeit der CFD-basierenden Diagnose- und Behandlungsunterstützung in der klinischen Routine erheblich verbessern.“*

*In dieser Studie schlagen wir einen DL-basierten Ansatz zur Berechnung von Druck und Wandschubspannung (WSS) in der Aorta und über der Aortenklappe von Patient*innen mit Aortenstenose (AS) vor. 103 individuelle Oberflächenmodelle der Aorta und der Aortenklappe wurden aus Computertomographiedaten von Patient*innen mit AS erstellt. Auf der Grundlage dieser Oberflächenmodelle wurden insgesamt 267 patientenspezifische, stationäre CFD-Simulationen der*

Aortenströmung bei verschiedenen Strömungsgeschwindigkeiten durchgeführt. Anhand dieser Simulationsdaten wurde ein künstliches neuronales Netz (ANN) trainiert, um den räumlich aufgelösten Druck und die WSS anhand einer zentrumslinienbasierten Darstellung zu berechnen. Eine ungewöhnliche Testgruppe von 23 Fällen wurde verwendet, um beide Methoden miteinander zu vergleichen.

Die ANN- und CFD-basierten Berechnungen stimmten gut überein, mit einer mittleren relativen Differenz zwischen beiden Methoden von 6.0 % für den Druck und 4.9 % für die Wandschubspannung.

*Diese Arbeit zeigt, dass DL-basierte Simulationsverfahren in der Lage sind, klinisch relevante hämodynamische Parameter für Patient*innen mit AS zu berechnen, und stellt eine mögliche Lösung für eine bessere klinische Translation der modellbasierten Behandlungsunterstützung dar.“*



OPEN ACCESS

EDITED BY

Sergey Karabasov,
Queen Mary University of London,
United Kingdom

REVIEWED BY

David Jean Winkel,
University Hospital of Basel,
Switzerland
Adelaide De Vecchi,
King's College London,
United Kingdom

*CORRESPONDENCE

Marie Schafstedde
✉ marie.schafstedde@dhz-charite.de

SPECIALTY SECTION

This article was submitted to
Cardiovascular Imaging,
a section of the journal
Frontiers in Cardiovascular Medicine

RECEIVED 03 January 2023

ACCEPTED 13 February 2023

PUBLISHED 03 March 2023

CITATION

Yevtushenko P, Goubergrits L, Franke B, Kuehne T and Schafstedde M (2023) Modelling blood flow in patients with heart valve disease using deep learning: A computationally efficient method to expand diagnostic capabilities in clinical routine. *Front. Cardiovasc. Med.* 10:1136935. doi: 10.3389/fcvm.2023.1136935

COPYRIGHT

© 2023 Yevtushenko, Goubergrits, Franke, Kuehne and Schafstedde. This is an open-access article distributed under the terms of the [Creative Commons Attribution License \(CC BY\)](#). The use, distribution or reproduction in other forums is permitted, provided the original author(s) and the copyright owner(s) are credited and that the original publication in this journal is cited, in accordance with accepted academic practice. No use, distribution or reproduction is permitted which does not comply with these terms.

Modelling blood flow in patients with heart valve disease using deep learning: A computationally efficient method to expand diagnostic capabilities in clinical routine

Pavlo Yevtushenko^{1,2}, Leonid Goubergrits^{1,2,3}, Benedikt Franke^{1,2}, Titus Kuehne^{1,2} and Marie Schafstedde^{1,2,4*}

¹Deutsches Herzzentrum der Charité (DHZC), Institute of Computer-assisted Cardiovascular Medicine, Berlin, Germany, ²Institute for Imaging Science and Computational Modelling in Cardiovascular Medicine, Charité – Universitätsmedizin Berlin, Berlin, Germany, ³Einstein Center Digital Future, Berlin, Germany, ⁴Berlin Institute of Health, Berlin, Germany

Introduction: The computational modelling of blood flow is known to provide vital hemodynamic parameters for diagnosis and treatment-support for patients with valvular heart disease. However, most diagnosis/treatment-support solutions based on flow modelling proposed utilize time- and resource-intensive computational fluid dynamics (CFD) and are therefore difficult to implement into clinical practice. In contrast, deep learning (DL) algorithms provide results quickly with little need for computational power. Thus, modelling blood flow with DL instead of CFD may substantially enhance the usability of flow modelling-based diagnosis/treatment support in clinical routine. In this study, we propose a DL-based approach to compute pressure and wall-shear-stress (WSS) in the aorta and aortic valve of patients with aortic stenosis (AS).

Methods: A total of 103 individual surface models of the aorta and aortic valve were constructed from computed tomography data of AS patients. Based on these surface models, a total of 267 patient-specific, steady-state CFD simulations of aortic flow under various flow rates were performed. Using this simulation data, an artificial neural network (ANN) was trained to compute spatially resolved pressure and WSS using a centerline-based representation. An unseen test subset of 23 cases was used to compare both methods.

Results: ANN and CFD-based computations agreed well with a median relative difference between both methods of 6.0% for pressure and 4.9% for wall-shear-stress. Demonstrating the ability of DL to compute clinically relevant hemodynamic parameters for AS patients, this work presents a possible solution to facilitate the introduction of modelling-based treatment support into clinical practice.

KEYWORDS

deep learning, computational fluid dynamics, heart valve disease, aortic stenosis, in-silico modelling, artificial neural network, image-based modelling

1. Introduction

In the medical health sector, the impact of artificial intelligence (AI)-based technologies is steadily increasing. While automated medical image analysis is arguably the most successful domain of medical AI applications (1–4), its use becomes conceivable in almost all medical fields, such as diagnostic assessments (5), prediction of patients' prognoses (6, 7), assistance in surgical interventions (8) and many more.

On the other hand, hemodynamic modelling, i.e., the computational modelling of blood flow using computational fluid dynamics (CFD) simulations, is also gaining more and more attention as the availability of computational power steadily increases. Having the potential to improve, facilitate and complement current diagnostic and therapy decision-making processes (9–14), CFD simulations are increasingly applied in cardiovascular research (15–17). In the case of aortic valve disease specifically, CFD simulations are used to predict hemodynamic parameters which may be critical to clinical outcome. These include, but are not limited to, paravalvular leakage (18–20), pressure and wall-shear-stress (WSS) in the aorta after aortic valve replacement for different valve types and sizes (21, 22) as well as flow patterns generated by different valve diseases and prosthesis types (15, 23).

However, translation of these models into clinical routine remains cumbersome. Not only are CFD simulations very demanding with respect to time and computational costs (several hours on high-end workstations), they also often require expertise in both engineering and medicine. As a result, diagnosis and/or treatment support solutions based on cardiovascular modelling rarely find their way into clinical practice (24–26). Although there are examples of a successful translation [e.g., HeartFlow® (14)], there is a strong discrepancy between the amount of proposed cardiovascular modelling applications and actual clinical applications.

In this regard, deep learning (DL)-based algorithms are potentially suited to overcome the problem of computational demand for higher order cardiovascular modelling. Once trained, a DL algorithm can provide results quickly with little need for computational power or user experience. Considering that clinicians rarely have access to high-end workstations on the one hand and need to perform diagnosis and treatment planning quickly on the other, the above mentioned advantages of a DL-based method may substantially increase the clinical feasibility of hemodynamic modelling. Several studies already showcased the potential of DL-based methods to accurately predict hemodynamic parameters. Examples of application include coronary arteries (27), aortic coarctation (28) and abdominal aortic aneurysms (29). In this study, we investigate the ability of DL-based methods to model hemodynamics of patients with aortic valve stenosis (AS).

AS represents the leading valvular heart disease with surgical (aortic valve reconstruction or replacement) and interventional (transcatheter aortic valve implantation, TAVI) treatment options that are increasingly applied also in elderly patients. It is thus a pathology with a considerable socio-economic burden. Accurate diagnostic assessment including either echocardiographic or catheter-based pressure measurements is mandatory to quantify AS severity degree and to define treatment indication (30). Given the complex nature of the pathological patterns of aortic flow and WSS encountered in AS patients, a more detailed and multimodal diagnostic assessment is desirable and necessary to identify the best patient-individual treatment strategy and the benefits of patient-specific modelling of hemodynamics in that context are widely recognized (15, 21–24, 31).

In this study, we use CFD generated hemodynamic data to develop an artificial neural network (ANN) which computes clinically relevant hemodynamic parameters for AS patients. Using high resolution computed tomography (CT) image data, a large set of patient-specific hemodynamic CFD simulations is built based on a workflow developed earlier (22). Using these simulation results, an ANN is trained to predict pressure and WSS from patient specific geometry in a compact, centerline-based representation. Additionally, the centerline-based pressure and WSS is computed for a separate set of test cases using ANN and CFD to assess the ANN's ability to compete with CFD simulations.

2. Materials and methods

2.1. Clinical data acquisition

Temporally resolved CT image data sets of 103 patients with AS who were treated in two different centers between February 2019 and October 2020 were retrospectively analyzed.

Inclusion criteria were the presence of aortic valve stenosis with indication for aortic valve replacement according to the European Society for Cardiology (ESC) guidelines and the interdisciplinary decision of the Heart Team and the availability of temporally resolved, high-resolution CT images for each patient. No further exclusion criteria were defined. The study was registered at [ClinicalTrials.gov](#) (NCT04600739) and was approved by the internal review board (EA2/174/19). Individual informed consent was waived due to the retrospective nature of this study. Patient's characteristics at baseline are depicted in [Table 1](#).

Computed tomography image data sets of the entire heart were acquired prior to the TAVI-procedure. The detailed protocol was previously published (32). An electrocardiogram-synchronized scan was conducted using either a wide area-detector volume CT scanner (Aquilion One Vision, Canon Medical 79 Systems, or Revolution CT, GE Healthcare) or a dual-source multi slice spiral CT scanner (Somatom Definition Flash, Siemens 78 Healthcare). Intravenous contrast medium was injected prior to each examination in order to improve image data contrast.

To allow the exact identification of the systolic phase with the widest aortic valve opening area, a multiphase data set, i.e., multiple scans at different time points, was reconstructed for each patient. All images were reconstructed with a soft-tissue convolution kernel and with the use of a dedicated noise reduction software. The spatial resolution used for segmentation was (0.39–0.648 mm) x (0.39–0.648 mm) in-plane resolution and (0.5–1 mm) slice thickness. The temporal resolution ranged from 70 ms to 140 ms.

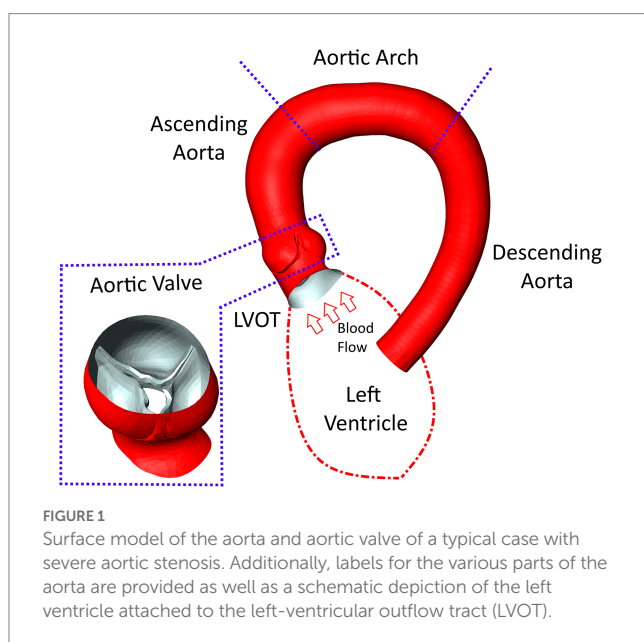
Baseline echocardiographic evaluation results are additionally presented in [Table 1](#). The echocardiographic data shows a wide range of aortic valve area (AVA) within the patient cohort, including cases with healthy AVA ($>1 \text{ cm}^2$), moderately (up to 0.7 cm^2) and highly stenosed ($<0.5 \text{ cm}^2$) cases.

2.2. Image data segmentation

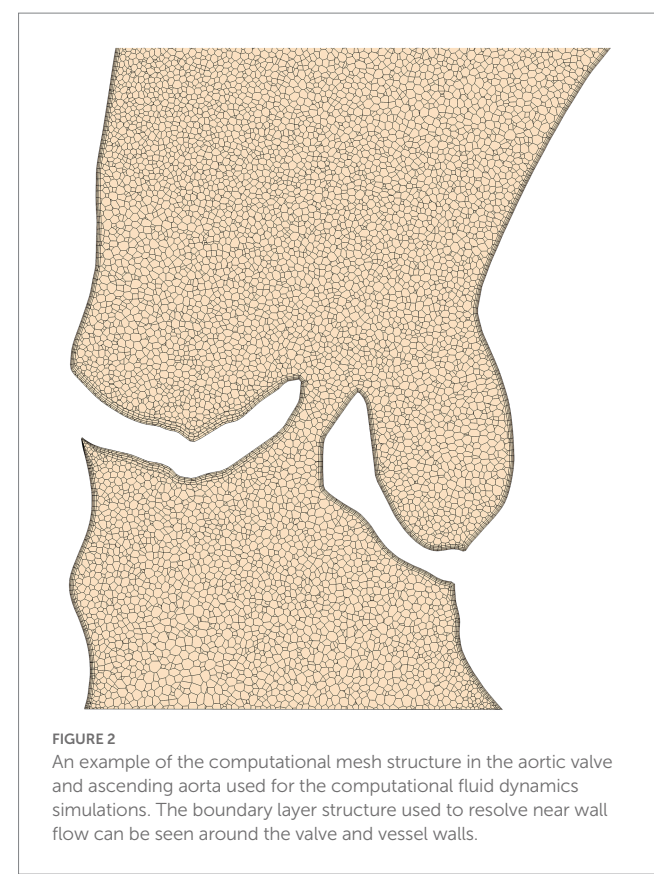
Based on the acquired CT data, the patient-specific surfaces of the aorta and aortic valve were segmented semi-automatically

TABLE 1 Patient characteristics.

Patient characteristic	Mean \pm SD	Range
General patient information		
Age [years]	82 \pm 5	61–94
Height [cm]	168 \pm 10	145–195
Weight [kg]	77 \pm 19	35–135
Echocardiographic assessment		
TPG [mmHg]	61.9 \pm 22.0	20–118
AVA [cm^2]	0.74 \pm 0.17	0.4–1.1
Stroke volume [ml]	52.2 \pm 16.7	17–97
Ejection fraction [%]	57.3 \pm 8.9	25–73



using a shape-constrained deformable model that was described earlier (32). Briefly, a parametric surface model of the aorta and aortic valve (33) is automatically adjusted to fit a given set of patient-specific CT images. Since the aortic valve is expected to be fully opened during the ejection phase simulated here, the valve is reconstructed in its fully-opened position using the respective CT images from the multiphasic dataset. An additional manual adjustment of the leaflet surfaces ensures an accurate representation of the aortic valve, which is critical for calculating transvalvular and aortic hemodynamics. Aorta and aortic valve surfaces are then combined into a single surface that defines the flow domain for the CFD simulation and the ANN input. The final model includes the left-ventricular outflow tract (LVOT), the open valve as seen at the time of peak systolic flow and the ascending aorta, aortic arch and descending aorta. Aortic branching vessels are not included in the model since their impact on hemodynamics in the valve region is considered negligible. Figure 1 shows a typical surface geometry with a labelling of the different parts (LVOT, valve, ascending, arch, descending aorta) as well as a close-up of the aortic valve.



2.3. Numerical simulation

Numerical flow simulations were performed using Siemens StarCCM+ v.15.04 (Siemens PLM, Plano, Texas). StarCCM+ uses the finite volume method to numerically solve the incompressible Navier-Stokes governing equations for the pressure and velocity fields. Given the high Reynolds number expected, a k-omega SST was used to account for turbulence. Blood was considered incompressible with a shear rate dependent viscosity based on the works of Abraham et al. (34) to account for the non-Newtonian behavior of blood (density = 1,050 kg/m³, zero/infinite-shear viscosity = 0.16/0.0035 Pa·s).

Discretization of the flow domain was performed using StarCCM+'s built in polyhedral meshing algorithm with five boundary layers to improve near wall flow resolution. Mesh size and structure is based on experience from similar studies made previously (22) for which mesh independency was analyzed. The analysis compared centerline-based pressure and WSS between four different mesh sizes ranging from very fine (10 million cells) to coarse (0.5 million cells) meshes. Medium sized meshes containing approximately 1.5–3 million cell/ 5–15 million nodes (depending on the size of the flow domain) yielded the best balance between accuracy and runtime showing a mean difference of 1–2 mmHg/2–4 Pa for pressure and WSS, respectively, compared to the reference solution. Figure 2 shows a longitudinal cross section of the mesh in the LVOT, aortic valve and ascending aorta.

Owed the complex nature of three-dimensional viscous fluid flow on the one hand and the limited amount of clinical data on the other, some simplifications regarding the numerical modelling process were necessary however. Simulations were therefore performed with steady

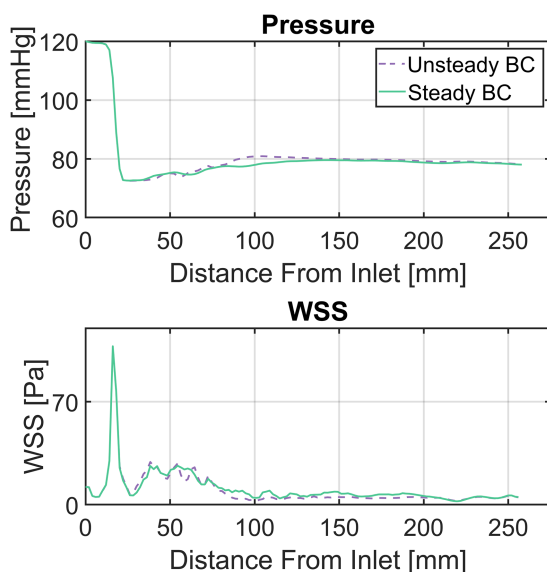


FIGURE 3

Comparison between a simulation with unsteady flow boundary conditions (BC) and a steady flow BC at peak systolic flow rate for a patient with a severe aortic stenosis. Top diagram compares pressure, bottom diagram wall-shear-stress (WSS). The flow curve for the ejection phase as well as the peak-systolic flow rate were derived from left-ventricular volumetry data.

flow boundary conditions at peak systolic flow rates, i.e., the maximum flow rate achieved during the ejection phase of the cardiac cycle. Furthermore, vessel wall and valve leaflets were considered rigid. Thus, the simulations model peak-systolic, instantaneous hemodynamics only, where the AS induced transvalvular pressure gradient (TPG) is expected to have the highest relevance. A transient solver (second order backward, 0.001 s time step) was used however to capture small-scaled unsteady flow effects such as flow separation and the valve jet mixture layer. The time step size of 1 ms ensures that the CFL-number remains at the order of one for a sufficient numerical stability and temporal resolution of the aforementioned unsteady effects.

Peak systolic flow rates were derived from left-ventricular volumetry (LVV) (32), which computes flow rate from the change of ventricular volume over time. However, multiphasic imagery suitable for LVV was available for only 67 of the 103 patients. For the remaining 36 patients, flow rates were drawn from a normal distribution whose mean and standard deviation were shifted based on case-specific AVA. This provided physiologically plausible flow rates with a certain degree of randomness, thus avoiding any deterministic relationships between geometry and flow rate which might harm the ANNs ability to generalize. Inlet boundary pressure was not prescribed since the pressure level has no influence on the solution of incompressible flow. However, pressure values were shifted to match an outlet pressure of 130 mmHg during post-processing for improved presentability. This value is based on the average of systolic pressure found in our patient cohort (Table 1).

Although the ability of the quasi-steady approach utilized here to accurately compute peak-systolic hemodynamics was investigated in earlier work (21, 22, 35), an additional analysis was performed for this study. Here, a flow rate curve was derived from LVV data for one

patient with a severe stenosis and an unsteady simulation was performed containing the entire ejection phase. The centerline based values for pressure and WSS (as described in the next section) were compared between the unsteady and the quasi-steady simulation. The results of this comparison are shown in Figure 3 with centerline based pressure and WSS plotted for both simulations. The mean absolute and relative errors for pressure and WSS were found to be 0.7 mmHg/1.2% and 1.8 Pa/1.6% respectively, further supporting the validity of the peak-systolic simulation approach.

In addition to the baseline peak-systolic flow rates, simulations with varied flow rates were also performed to increase the amount of training data for the ANN. Flow rates were varied by $\pm 25\%$ of the respective base peak-systolic flow. This flow variation produces a desired substantial change in hemodynamics and corresponds with literature data on exercise-induced peak systolic flow change (36–39). This increased the total amount of simulations from 103 to 309.

2.4. Computational fluid dynamics post-processing

Although it is technically possible to use the three-dimensional data fields to train the ANN, a more compact representation of the simulation results becomes necessary considering the limited amount of training data available. This compact representation is constructed by locally averaging pressure and WSS along the aortic centerline using cross-section planes. This centerline-based representation substantially reduces input data dimensionality while retaining key spatial information. Moreover, this representation has shown to be more feasible for clinical use in our experience than three-dimensional data fields. Constructing the centerline-based representation of static pressure is performed in three steps:

- Generation of a discrete (2 mm point spacing) aortic centerline from the case-specific surface model.
- Creation of centerline-orthogonal vessel cross-sections at each centerline point.
- Calculating the average of static pressure on each cross-section and assigning the resulting value to the respective centerline point.

In the valve region, only the area bound by the valve leaflets is used to calculate cross-section averaged pressure.

For WSS, the process is identical except that WSS is not averaged on the cross-sections planes but on vessel segments between two adjacent cross sections. For WSS in the valve region, only the inner leaflet surfaces are used to compute local WSS. Figure 4 illustrates the creation of the centerline-based representation from the CFD simulations.

2.5. Artificial neural network architecture

A recurrent neural network (RNN) is used to compute the hemodynamic parameters of pressure and WSS in the compact representation described above from a sequence of input features. These two hemodynamic parameters are chosen based on their clinical relevance. Static pressure derived TPG is the primary parameter for AS diagnostic and treatment (30) whereas aortic WSS

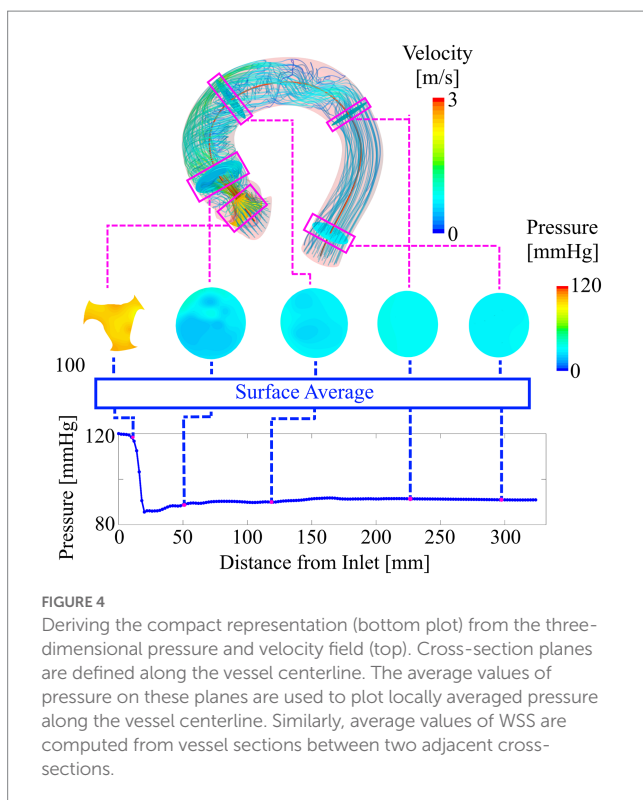


FIGURE 4

Deriving the compact representation (bottom plot) from the three-dimensional pressure and velocity field (top). Cross-section planes are defined along the vessel centerline. The average values of pressure on these planes are used to plot locally averaged pressure along the vessel centerline. Similarly, average values of WSS are computed from vessel sections between two adjacent cross-sections.

is known to be a factor for aneurysm growth and other vessel degradation mechanisms (40–43).

A bi-directional long short-term memory (LSTM) RNN is used. This choice of architecture is well suited to work with the sequence-like data provided by the centerline-based representation and has proven successful in a similar study published earlier (28). The RNN is built using Matlab's Deep Learning Toolbox R2020a (MathWorks, Natick, MA, United States).

The LSTM uses a sequence of input features derived from the case-specific surface model and flow rate and outputs a sequence of state vectors. From these state vectors, a fully connected layer computes the values of pressure and WSS along the vessel centerline. Figure 5 illustrates the various components of the network as well as the data flow through the components. Both input and output sequences are centerline-based, meaning their values are defined at their respective centerline points. The following input features are used:

- Centerline point coordinates ($n \times 3$).
- Cross-section area ($n \times 1$).
- Cross-section area normalized flow rate ($n \times 1$).
- m -dimensional encoded cross-section shape ($n \times m$).

Where n denotes the number of centerline points for a given case (usually 110–130, depending on the length of the aorta).

The last feature is provided by an auto encoder (AE) which is trained separately. Using the AE, information on cross-section shape can be passed to the LSTM using only a few parameters of size m instead of complex polygons or triangulations. This information is deemed necessary since valve geometry varies substantially between individual cases and using cross-section area alone might not suffice to account for this geometrical variation.

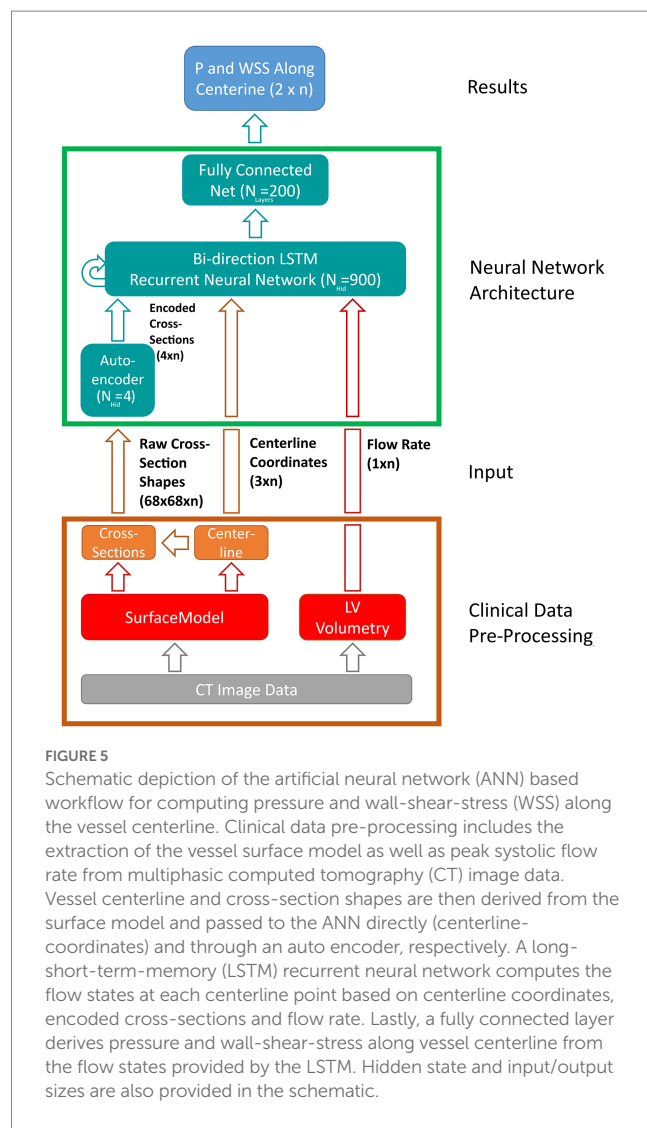


FIGURE 5

Schematic depiction of the artificial neural network (ANN) based workflow for computing pressure and wall-shear-stress (WSS) along the vessel centerline. Clinical data pre-processing includes the extraction of the vessel surface model as well as peak systolic flow rate from multiphasic computed tomography (CT) image data. Vessel centerline and cross-section shapes are then derived from the surface model and passed to the ANN directly (centerline-coordinates) and through an auto encoder, respectively. A long-short-term-memory (LSTM) recurrent neural network computes the flow states at each centerline point based on centerline coordinates, encoded cross-sections and flow rate. Lastly, a fully connected layer derives pressure and wall-shear-stress along vessel centerline from the flow states provided by the LSTM. Hidden state and input/output sizes are also provided in the schematic.

The AE used here is part of Matlab's Deep Learning toolbox and consists of a single-layer neural network (the encoder) that maps an input of size n to a hidden state of size m . From this hidden state, a second neural network (the decoder) reconstructs the original input data. The error between original and reconstructed input allows to define a cost function which is used to extract information critical to ANN accuracy from the original input (in this case cross-section shape), thereby allowing to substantially reduce input dimensionality without compromising accuracy. The size of the encoded state m (i.e., the amount of 'essential' information contained in the raw cross-section shapes) is determined during hyperparameter optimization. Further reference on the AE used in this study can be found in the respective Matlab documentation (44).

2.6. Artificial neural network training and hyperparameter optimization

A total of 309 simulation results were available for training and validation. This dataset was reduced to 267 cases based on a maximum pressure drop (MPD), defined as the difference between inlet pressure

and the lowest pressure found within the vessel, of 120 mmHg. This removed cases with an unphysiologically high pressure drop caused by either an excessive flow rate (+25% or modelled flow), an underestimation of valve area (i.e., segmentation errors) or a combination of both. The threshold of 120 mmHg is based on clinical guidelines, where TPG of 60 mmHg is already considered severe (30). Thus, an MPD in excess of twice this value is believed to be beyond what is found in the vast majority of AS patients. This is further supported by the echocardiographic TPG data obtained for this cohort (Table 1). Although this retains cases with a TPG that is well above any value considered critical for an intervention, it is believed that retaining this data is beneficial for the ANN's accuracy in the clinically relevant range.

The remaining 267 cases were split into 11 datasets, one for testing and the other 10 for training and validation/optimization. Stratification was achieved by ensuring that each subset covers the whole range of allowable MPD (approx. 0–120 mmHg). Moreover, individual geometries were not distributed across subsets, meaning that a particular case will have all of its flow variations (baseline ±25%) within one subset. Thus, it is ensured that validation/test data remains fully unknown during training/testing. The test subset contained 23 cases, leaving 244 cases for training and hyperparameter optimization.

Network training was performed using adaptive moment estimation, a stochastic gradient descend algorithm that aims at minimizing the loss function (i.e., the difference between desired and actual network output). Hyperparameter optimization was performed using grid search. For each configuration, a 10-fold cross validation was performed. The configuration with the highest average accuracy was chosen as the final model. The following hyperparameters were considered (optimum values in brackets):

- AE input size (68 × 68).
- AE hidden size (4).
- LSTM hidden size (900).
- Fully connected layer size (200).

ANN robustness and explainability was analyzed using a local feature perturbation approach used earlier (28). This method locally changes the input feature sequences around a given centerline point by ± one standard deviation and measures the output RMSE between the altered and original input.

2.7. Artificial neural network accuracy assessment

ANN accuracy was assessed by computing the root-mean-square-error (RMSE) between CFD- and ANN-based pressure/WSS on the test dataset. The pressure RMSE for a specific case is defined as:

$$RMSE_P = \sqrt{\frac{\sum_{i=1}^N (P_{i,ANN} - P_{i,CFD})^2}{N}} \quad (1)$$

Where $P_{i,ANN}$ and $P_{i,CFD}$ are the ANN/CFD-based values of pressure at the i -th centerline point and N is the number of centerline points.

RMSEs for pressure and WSS were furthermore normalized to provide a relative measure of accuracy. Pressure RMSE was normalized with CFD-based MPD whereas WSS was normalized with the maximum WSS observed in the respective CFD result.

$$NRMSE_P = \sqrt{\frac{\sum_{i=1}^N \left(\frac{P_{i,ANN} - P_{i,CFD}}{P_{i,CFD} - \inf\{P_{i,CFD}, \dots, P_{N,CFD}\}} \right)^2}{N}} \quad (2)$$

$$NRMSE_{WSS} = \sqrt{\frac{\sum_{i=1}^N \left(\frac{WSS_{i,ANN} - WSS_{i,CFD}}{\sup\{WSS_{i,CFD}, \dots, WSS_{N,CFD}\}} \right)^2}{N}} \quad (3)$$

Additionally, a test for statistical equivalence is performed using a two one-sided tests (TOST) procedure. TOST based equivalence tests decide whether two different measuring methods applied on a set of subjects can be considered statistically equivalent within some bounds ε_L and ε_U . In this study, the ANN- and CFD-based computation of TPG, which is the primary clinical parameters for AS assessment, are tested for equivalence as follows:

Let μ_{CFD} and μ_{ANN} be the median values of the CFD and ANN-based TPG values. Then the median difference:

$$\Theta = \mu_{CFD} - \mu_{ANN} \quad (4)$$

is hypothesized to be outside of a reference value $\Theta_0 \pm \text{an equivalence margin } \varepsilon$ using two separate null-hypotheses as:

$$H_1^0 : \Theta < \Theta_0 - \varepsilon \quad (5)$$

$$H_2^0 : \Theta > \Theta_0 + \varepsilon \quad (6)$$

Hypotheses (5) and (6) are tested using a signed rank test, since the TPG values are not normally distributed in our data. If both (5) and (6) can be rejected at some significance level α , it follows that both methods are equivalent in computing TPG within the bounds provided by ε (45, 46).

For this study, an equivalence margin ε of ±5 mmHg is used which corresponds to the accuracy of current clinical catheter-based pressure measurements (47). TPG is defined as the difference between inlet pressure and the pressure at the point of highest pressure recovery downstream of the aortic valve, exemplary depicted in Figure 6 (bottom).

3. Results

3.1. Computational fluid dynamics results

A total of 309 simulations were performed using 103 patient-specific geometries (baseline flow ±25%). 42 simulations were

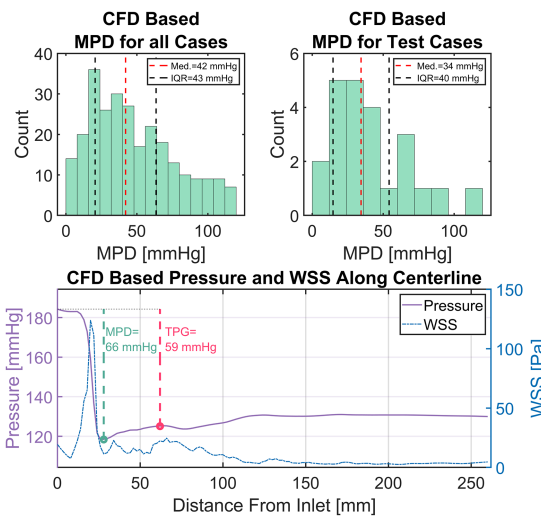


FIGURE 6

Top left: Distribution of maximum pressure drop (MPD) within the entire simulation data. Top right: Distribution of MPD within the set of test cases. Bottom: An exemplary depiction of CFD-based pressure and wall-shear-stress (WSS) in the compact representation (i.e., average along centerline). Additionally, the measurement points for transvalvular pressure gradient (TPG) and MPD (green and red) are shown with their respective values.

excluded based on an MPD of 120 mmHg as mentioned previously, leaving 267 simulations results. Figure 6 (top left) shows a histogram of the MPD distribution found in the simulation results. MPDs were not normally distributed with low to moderate MPD values (<40 mmHg) dominating the distribution. Median of MPD is 42 mmHg with an inter-quartile range (IQR) of 43 mmHg. The MPD distribution within the set test cases (Figure 6, top right) is equal to that of all cases (Wilcoxon rank sum test, $p < 0.05$) with a median of 34 mmHg and an IQR of 40 mmHg. The available training data is therefore biased towards moderate MPD values/stenosis severity. However, low and high MPD values appear sufficiently represented.

Figure 6 (bottom) provides an example of a typical case with a high pressure drop. The plot shows the simulation results in the compact representation described earlier, depicting locally averaged values for pressure and WSS along the vessel centerline. Additionally, the points defining MPD and TPG are shown with a green and red circle, respectively.

The characteristic rapid pressure drop and increase of WSS in the valve region can be seen as well as a slight pressure recovery in the ascending aorta along with a reduction of WSS. Moreover, a slight fluctuation of WSS with local maxima in the ascending aorta are observed, which is a result of secondary flow structures in that region generated by the valve jet.

3.2. Artificial neural network explainability and robustness

The explainability and robustness analysis revealed that the network is most sensitive to perturbations in the valve region while changes to the input downstream of the aortic valve have little effect on output (RMSE < 1 mmHg). Moreover, the input parameters of flow

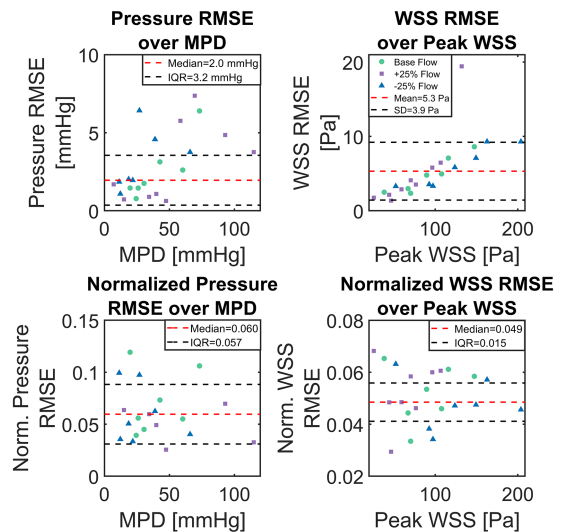


FIGURE 7

Scatter plots of absolute and normalized root-mean-square-errors (RMSE), calculated between computational fluid dynamics (CFD) simulations and artificial neural network (ANN)-based results for the set of 23 test cases. Top shows absolute pressure and wall-shear-stress (WSS) RMSE over CFD computed maximum pressure drop and maximum WSS, respectively. Bottom shows pressure and WSS RMSE normalized with TPG and maximum WSS, respectively.

and encoded cross-section shape appear to have the most influence on the hemodynamic results provided by the ANN. Reducing cross-section area/shape and/or increasing flow-rate results in an increase of TPG and *vice-versa* (RMSE 10–20 mmHg). These finding are in line with the fluid dynamic behavior expected for such a configuration, i.e., pressure drop over a local constriction as a function orifice area and flow velocity.

3.3. Artificial neural network accuracy

Median of absolute pressure RMSE for all 23 test cases was 2.0 mmHg with an IQR of 3.2 mmHg. Absolute WSS RMSE was normally distributed (Lilliefors test at $p < 0.05$) with a mean of 5.3 ± 3.9 Pa. Normalized pressure and WSS RMSE were not normally distributed with a normalized pressure RMSE median of 6.0% (IQR 5.7%) and a normalized WSS RMSE median of 4.9% (IQR 1.5%). A significant ($p < 0.001$) correlation between case-specific RMSE and MPD/peak WSS was observed, with correlations of 0.53 and 0.71, respectively. Neither geometric parameters such as AVA or aortic diameter/length nor the type of flow boundary condition (i.e., LVV based or modelled flow rate) were found to correlate with ANN accuracy.

Figure 7 shows scatter-plots of absolute (top) and relative (bottom) pressure and WSS RMSE over MPD and peak WSS for the 23 test cases. Data points in Figure 7 are color and shape coded to discriminate cases with baseline flow from those with reduced/increased flow. The absolute RMSE plots visually confirm the tendency of higher absolute RMSE with higher MPD. Moreover, an increased dispersion of absolute pressure RMSE can be seen at higher MPD whereas absolute WSS RMSE increases along a narrow band. A sole outlier with a comparably high WSS RMSE of 19.4 Pa is present

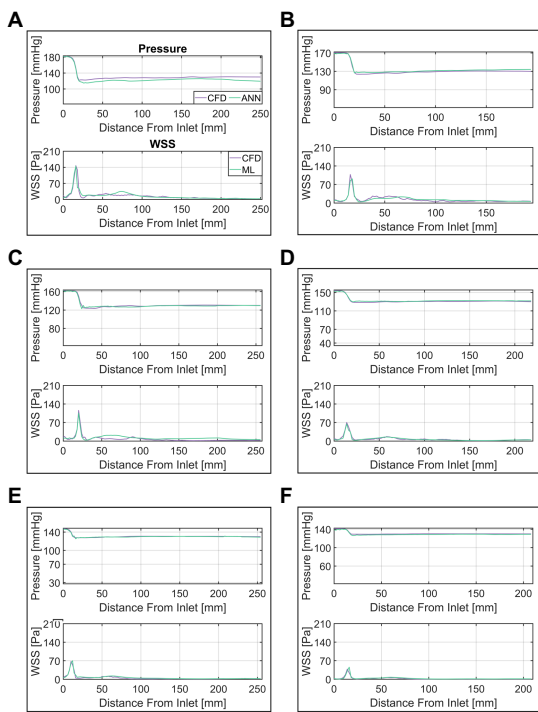


FIGURE 8
Comparison of ANN and CFD-based pressure and wall-shear-stress (WSS) along vessel centerline. Cases (A–F) are ordered by descending transvalvular-pressure-gradient.

though. A tendency of either baseline or $\pm 25\%$ flow to produce particularly large RMSE for pressure or WSS could not be observed.

A more detailed presentation of the ANN's performance is provided in Figure 8. In this figure, a selection of six cases (A through F) of various MPD/TPG levels are shown with their respective CFD and ANN-based pressure/WSS along vessel centerline. ANN and CFD computed pressure match closely throughout the whole vessel except for case A, where the pressure drop in the valve region is overestimated by approximately 8 mmHg. This error propagates further downstream resulting in an overall discrepancy between ANN- and CFD-based pressure. Moreover, a slight fluctuation of pressure can be seen in cases B, C and E at the point of lowest pressure which is not present in the CFD data.

WSS appears to match similarly well between CFD and ANN, however, notable differences occur in the ascending aorta. In that region, the ANN either overestimates WSS (case C) or fails to capture local fluctuations (case B) or a combination of both (case A). WSS in the valve region on the other hand matches well between ANN and CFD.

Finally, the TOST for TPG measurement equivalency between CFD (median 32 mmHg, IQR 37 mmHg) and ANN (median 34 mmHg, IQR 33 mmHg) resulted in both methods being equivalent within the equivalency bounds of ± 5 mmHg ($p < 0.001$).

4. Discussion

In this pilot study, we presented a deep ANN computing spatially resolved, compact hemodynamics in the aorta and aortic valve of AS patients as an alternative to traditional numerical modelling. The

network was trained using 244 patient-specific CFD simulations of the aorta and aortic valve while 23 simulation were used for the evaluation of the ANN's performance. Modelling hemodynamics using AI has been undertaken by several studies earlier (27, 28, 48, 49). However, this kind of application is still rather underrepresented in the medical field (50–52), although it appears worthwhile exploring given the potential benefits outlined in the introduction.

The comparison between ANN- and CFD-based pressure computations provided in the results section showed good agreement between both methods with differences being at the order of a few mmHg. Considering that clinically relevant TPG values are at the order of 20 mmHg and upwards (30), the observed pressure error can be considered rather low. For the computation of TPG, both methods can even be considered equivalent within current clinical pressure measurement margins.

Assessing the accuracy of ANN-based WSS computation is more difficult, since no current clinical guidelines for WSS measurement or evaluation exist. Thus, the mean error of approx. 5 Pa is difficult to put into a meaningful clinical perspective. However, judging by the normalized accuracy, WSS and pressure computations are similarly accurate, although some test cases showed substantial errors in the ascending aorta. Another interesting finding is that ANN accuracy does not suffer from altering the flow rate given any particular geometry. This may provide an important capability for clinical use, as outlined further below.

All in all, an ANN-based modelling of aortic hemodynamics of AS patients appears to be a viable alternative to CFD. Considering the enormously lower computational time required (hours for CFD vs. seconds for ANN), ANN-based methods may facilitate the translation of hemodynamic modelling into clinical practice, something that CFD-based methods struggle with, despite their potential (15, 21–23, 53).

4.1. Potential clinical application

In the context of the use case of AS discussed here, such an ANN could be embedded into a CT or magnetic resonance imaging (MRI) scanner, expanding the diagnostic capability of the device to provide treatment-critical hemodynamic information (e.g., pressure, TPG) along with image data in real-time. This could in turn reduce the requirement for invasive diagnostics of TPG and thus reduce costs and patient risk. Furthermore, the change in TPG under increased cardiac output (i.e., flow) could be simulated for borderline-symptomatic patients, thus reducing or even replacing the current practice of measuring pressure under drug or exercise induced stress for such patients (54, 55). Finally, the ANN presented here can be expanded to model aortic hemodynamics for bicuspid aortic valves, prosthetic valves such as TAVI, biological or mechanical valve replacement, thereby providing treatment planning and hemodynamic outcome prediction capabilities (21, 22).

4.2. Error analysis and potential improvement

Although the results are promising, the work presented here does not fully provide the potential capabilities outlined above yet and several factors need to be considered for a successful clinical translation. First of all, the ANN and CFD-based results show notable

differences for cases with high MPD/TPG. Especially WSS appears to diverge substantially between the two methods in the ascending aorta, as seen in [Figure 8](#). These errors indicate that the ANN does not fully capture the relationship between geometry, flow rate and pressure/WSS distribution inside the vessel.

For both pressure and WSS, an increase in ANN pressure and WSS RMSE was observed with an increase of MPD and max WSS, respectively. This was more pronounced for WSS, where maximum WSS and WSS RMSE were notably correlated. This suggests that the overall error can be viewed as a combination of a systematic error which depends on some parameter/feature and a random error. The systematic error may be explained by the fact that with higher MPD/maximum WSS, the ANN struggles to capture the resulting high spatial variation of these parameters along the centerline since the distance between the centerline points is fixed to 2 mm. Moreover, the loss of spatial information from the cross-section averaging process has a greater impact on cases with a severe stenosis and thus high MPD/maximum WSS. For such cases, the pressure/WSS on a single cross section plane may vary by up to 20 mmHg/50 Pa, which appears mostly in the region where the valve jet impinges the vessel wall. The cases displayed in [Figures 8A–C](#) confirm this, since the largest differences ANN and CFD-based WSS are seen downstream of the valve at the end of the ascending aorta (50–75 mm downstream). For cases with a less severe stenosis and thus weaker valve-jet, the differences are far lower making the cross-section averaged representation more true to the actual distribution of pressure and WSS.

In this context, the correlation between RMSE and MPD/max WSS may be seen as an indicator which of the two error sources, constant or random, dominates the overall error. Hence, the random error appears more influential for pressure RMSE than it is for WSS RMSE, where it supposedly accounts for half of the variance in the WSS RMSE (R^2 of 0.5). This appears reasonable given the fact that the local variation of WSS across the vessel wall is higher than the local variation of pressure on the cross sections (with respect to the overall level of pressure/WSS). The random error, on the other hand, is likely the result of uncertainties in the input data, as will be discussed further below. All in all, the differences observed between CFD and ANN based solutions can be attributed to the following factors:

1. Uncertainty in the input data.
2. Random numerical errors in the training data (i.e., CFD).
3. Comparably low amount of training data/biased training data.
4. Input data pre-processing.

The first two factors mostly contribute to the random error described earlier. The uncertainty in the input data for instance, which results from inconsistencies in the definitions of the cross-sections/vessel segments in the valve region, may omit pressure/WSS data in some cases, leading to an erroneous input and thus result. The random numerical errors are the result of the discretization error inherent to the CFD method on the one hand and the fact that the pressure and velocity fields fluctuate slightly during runtime on the other. These are at the order of 1–2 mmHg based on the mesh independency study as well as the convergence behavior observed in our simulations.

The last two points are likely to influence both the systematic and the random error. More training data would provide a denser sampling of the parameter space (both geometric and hemodynamic parameters) and allow for more sophisticated inputs to be used, thus

potentially reducing the random error. Moreover, additional cases in the high MPD range would remove the bias in the training data which could be another factor contributing to the systematic error besides the ones discussed earlier.

The pre-processing of input data plays a key role in how information is passed to the network. Currently, the raw simulation as well as the shape data are substantially reduced using the centerline-based representation. This was deemed necessary to efficiently utilize the clinical data available for this study. However, it creates the aforementioned problems of spatial discretization as well as the mismatch between average and actual pressure/WSS distributions. Furthermore, the auto encoder-based reduction of the cross section shape dimensionality is also likely to introduce errors into the input data and hence the results. Increasing input data dimensionality with a denser centerline sampling, a larger AE hidden-state size and more distribution parameters for pressure and WSS are likely to reduce both the systematic error as well as the random error through input data uncertainty. However, the possibility of providing additional input data is closely tied to clinical data availability.

Finally, the choice of ANN architecture itself is worth evaluating, although the question of optimal ANN architecture cannot be definitely answered within the scope of this study. While the choice of architecture used here appears reasonable given the underlying physical modelling problem, it is not necessarily the best one. Other ANN types such as convolutional neural networks, which are highly successful in working with image data, may produce even better results depending on available input data and required output. Evaluating different types of architectures should therefore be another key aspect of future studies.

4.3. Limitations

An important concern regarding the translatability of the ANN into clinical practice is the underlying CFD method, on which the ANN is trained. Since the ANN can only be as good as the training data it uses (i.e., the CFD data), it must be ensured that the CFD-based hemodynamic modelling is accurate and validated against clinical data. Although CFD simulations of aortic flow in AS patients using the setup employed here showed good agreement with clinical data in earlier studies ([15, 21, 22, 32](#)), a thorough validation under controlled conditions is necessary. This was not possible in this study since the CT imaging on which the CFD is based and echocardiographic measurements were performed on different appointments. This potentially introduces a number of unknown errors. In addition, echocardiographic TPG measurements are suspected to systematically overestimate TPG ([56](#)) making the clinical TPG data available here unsuitable for validation purposes. The above however does not necessarily impact the potential of an ANN to substitute CFD modelling, since CFD simulation inaccuracies often result from inaccurate input data (segmentation, flow boundary conditions) rather than from a lack of modelling complexity.

The steady-state, peak systolic computational model employed in this study is another limitation worth mentioning. This simplification was deemed necessary to find a good balance between modelling complexity and clinical relevance for this initial work. And while this approach may already provide clinically relevant data ([15, 21, 35, 57](#)), obtaining hemodynamic information from a whole cardiac cycle is certainly desirable. In particular, the time averaged TPG, which is

another important factor in AS diagnosis and treatment decision (30), cannot be calculated using the quasi steady-state approach used here. Other clinically relevant hemodynamic parameters such as time-averaged WSS and the oscillatory shear index, which are hypothesized to influence aortic valve and aortic wall degeneration (58–61), also fall outside of the current capabilities of the ANN. Therefore, extending the CFD and the ANN to model unsteady hemodynamics is necessary to fully evaluate the potential of ANN-based hemodynamic modelling.

Finally, an important aspect necessary to realize an application of an ANN-based hemodynamic computation as outlined earlier in the section is the pre-processing of clinical input data. Although the ANN presented here partially uses image data for the input, this image data is not raw CT or MRI data and all input sequences are derived from a segmented surface of the aorta and valve. This surface is currently the result of a lengthy semi-manual segmentation of CT data, which negates the ANN's primary benefits of low computational times and user interaction. Therefore, a fast segmentation algorithm capable of automatically extracting aortic centerline, aortic- and valve-surfaces from cardiac CT or MRI is necessary. The development of such algorithms is ongoing and several promising methods exist, however, automatic segmentation of cardiac image data remains a challenging task (62).

5. Conclusion

The ANN-based computation of pressure and WSS in patients with AS is a viable alternative to time- and resource-intensive CFD-based modelling. Requiring very little computational power or user interaction, ANN-based hemodynamic modelling can become a key part in the integration of hemodynamic modelling into clinical practice, thereby expanding diagnostic capabilities, reducing costs and improving outcome. However, in its current state, the ANN presented here needs further improvement to be suitable for a clinical application. Apart from improving the ANN's accuracy as outlined in section 4.2, further work is required to validate ANN accuracy against clinical data as well as provide an automatic image segmentation tool in order to derive a hemodynamic outcome from raw image data in a clinical setting. Nevertheless, the suitability of ML-based methods to perform hemodynamic modelling has been demonstrated.

Data availability statement

The datasets presented in this study can be found in online repositories. The names of the repository/repositories and accession number(s) can be found at: <https://figshare.com>, DOI: 10.6084/m9.figshare.19478117.

References

- Park, A; Chute, C; Rajpurkar, P; Lou, J; Ball, RL; Shpanskaya, K, et al. Deep learning-assisted diagnosis of cerebral aneurysms using the HeadXNet model, (in eng). *JAMA Netw Open*. (2019) 2:e195600. doi: 10.1001/jamanetworkopen.2019.5600
- Chan, HP; Samala, RK; Hadjiiski, LM; and Zhou, C. Deep learning in medical image analysis, (in eng). *Adv Exp Med Biol*. (2020) 1213:3–21. doi: 10.1007/978-3-030-33128-3_1
- Litjens, G; Ciompi, F; Wolterink, JM; de Vos, BD; Leiner, T; Teuwen, J, et al. State-of-the-art deep learning in cardiovascular image analysis, (in eng). *JACC Cardiovascular Imaging*. (2019) 12:1549–65. doi: 10.1016/j.jcmg.2019.06.009
- IVANTSITS, M; GOUBERGRITS, L; KUHNIGK, JM; HUELLEBRAND, M; BRUENING, J; KOSSEN, T, et al. Detection and analysis of cerebral aneurysms based on X-ray rotational angiography - the CADA 2020 challenge, (in eng). *Med Image Anal*. (2022) 77:102333. doi: 10.1016/j.media.2021.102333
- Esteva, A; Kuprel, B; Novoa, RA; Ko, J; Swetter, SM; Blau, HM, et al. Dermatologist-level classification of skin cancer with deep neural networks, (in eng). *Nature*. (2017) 542:115–8. doi: 10.1038/nature21056
- Yu, KH; Zhang, C; Berry, GJ; Altman, RB; Ré, C; Rubin, DL, et al. Predicting non-small cell lung cancer prognosis by fully automated microscopic pathology image features, (in eng). *Nat Commun*. (2016) 7:12474. doi: 10.1038/ncomms12474
- Meyer, A; Zverinski, D; Pfahringer, B; Kempfert, J; Kuehne, T; Sündermann, SH, et al. Machine learning for real-time prediction of complications in critical care: a

Ethics statement

The study was registered at ClinicalTrials.gov (NCT04600739) and was approved by the internal review board (EA2/174/19). Written informed consent for participation was not required for this study in accordance with national legislation and the institutional requirements.

Author contributions

PY and BF: data curation. PY and LG: formal analysis. LG, TK, and MS: funding acquisition. PY, LG, and MS: investigation and writing-original draft. PY: methodology and visualization. MS and LG: supervision. All: writing-review and editing, conceptualization, and contributed to the article and approved the submitted version.

Funding

The work presented here is largely built on the “ArtiCardio” project, which was funded by the German Federal Ministry of Education and Research (BMBF), grant number 13GW0208B. MS is a participant in the BIH Charité Digital Clinician Scientist Program funded by the Charité – Universitätsmedizin Berlin, and Berlin Institute of Health at Charité (BIH). Additional funding was provided through professor Goubergrits by the Einstein Center Digital Future (ECDF). Finally, we would like to acknowledge financial support from the Open Access Publication Fund of Charité – Universitätsmedizin Berlin and the German Research Foundation (DFG).

Conflict of interest

The authors declare that the research was conducted in the absence of any commercial or financial relationships that could be construed as a potential conflict of interest.

Publisher's note

All claims expressed in this article are solely those of the authors and do not necessarily represent those of their affiliated organizations, or those of the publisher, the editors and the reviewers. Any product that may be evaluated in this article, or claim that may be made by its manufacturer, is not guaranteed or endorsed by the publisher.

- retrospective study, (in eng). *Lancet Respir Med.* (2018) 6:905–14. doi: 10.1016/s2213-2600(18)30300-x
8. Shademan, A, Decker, RS, Opfermann, JD, Leonard, S, Krieger, A, and Kim, PC. Supervised autonomous robotic soft tissue surgery, (in eng). *Sci Transl Med.* (2016) 8:337ra64. doi: 10.1126/scitranslmed.aad9398
9. Al'Aref, SJ, Anchouche, K, Singh, G, Slomka, PJ, Kolli, KK, Kumar, A, et al. Clinical applications of machine learning in cardiovascular disease and its relevance to cardiac imaging, (in eng). *Eur Heart J.* (2019) 40:1975–86. doi: 10.1093/euroheartj/ehy404
10. Motwani, M, Dey, D, Berman, DS, Germano, G, Achenbach, S, al-Mallah, MH, et al. Machine learning for prediction of all-cause mortality in patients with suspected coronary artery disease: a 5-year multicentre prospective registry analysis, (in eng). *Eur Heart J.* (2017) 38:500–7. doi: 10.1093/euroheartj/ehw188
11. Ong, CW, Wee, I, Syn, N, Ng, S, Leo, HL, Richards, AM, et al. Computational fluid dynamics modeling of hemodynamic parameters in the human diseased aorta: a systematic review, (in eng). *Ann Vasc Surg.* (2020) 63:336–81. doi: 10.1016/j.avsg.2019.04.032
12. Samad, MD, Ulloa, A, Wehner, GJ, Jing, L, Hartzel, D, Good, CW, et al. Predicting survival from large echocardiography and electronic health record datasets: optimization with machine learning, (in eng). *JACC Cardiovasc Imaging.* (2019) 12:681–9. doi: 10.1016/j.jcmg.2018.04.026
13. Tabassian, M, Sunderji, I, Erdei, T, Sanchez-Martinez, S, Degiovanni, A, Marino, P, et al. Diagnosis of heart failure with preserved ejection fraction: machine learning of spatiotemporal variations in left ventricular deformation, (in eng). *J Am Soc Echocardiogr.* (2018) 31:1272–1284.e9. doi: 10.1016/j.echo.2018.07.013
14. Taylor, CA, Fonte, TA, and Min, JK. Computational fluid dynamics applied to cardiac computed tomography for non-invasive quantification of fractional flow reserve: scientific basis, (in eng). *J Am Coll Cardiol.* (2013) 61:2233–41. doi: 10.1016/j.jacc.2012.11.083
15. Hellmeier, F, Nordmeyer, S, Yevtushenko, P, Bruening, J, Berger, F, Kuehne, T, et al. Hemodynamic evaluation of a biological and mechanical aortic valve prosthesis using patient-specific MRI-based CFD, (in eng). *Artif Organs.* (2018) 42:49–57. doi: 10.1111/arr.12955
16. Neugebauer, M, Glöckler, M, Goubergrits, L, Kelm, M, Kuehne, T, and Hennemuth, A. Interactive virtual stent planning for the treatment of coarctation of the aorta, (in eng). *Int J Comput Assist Radiol Surg.* (2016) 11:133–44. doi: 10.1007/s11548-015-1220-3
17. Vellguth, K, Brüning, J, Goubergrits, L, Tautz, L, Hennemuth, A, Kertzscher, U, et al. Development of a modeling pipeline for the prediction of hemodynamic outcome after virtual mitral valve repair using image-based CFD, (in eng). *Int J Comput Assist Radiol Surg.* (2018) 13:1795–805. doi: 10.1007/s11548-018-1821-8
18. Anam, SB, Kovarovic, BJ, Ghosh, RP, Bianchi, M, Hamdan, A, Haj-Ali, R, et al. Assessment of paravalvular leak severity and thrombogenic potential in transcatheter bicuspid aortic valve replacements using patient-specific computational modeling, (in eng). *J Cardiovasc Transl Res.* (2022) 15:834–44. doi: 10.1007/s12265-021-10191-z
19. Bianchi, M, Marom, G, Ghosh, RP, Rotman, OM, Parikh, P, Gruberg, L, et al. Patient-specific simulation of transcatheter aortic valve replacement: impact of deployment options on paravalvular leakage, (in eng). *Biomech Model Mechanobiol.* (2019) 18:435–51. doi: 10.1007/s10237-018-1094-8
20. Dowling, C, Gooley, R, McCormick, L, Firooz, S, and Brecker, SJ. Patient-specific computer simulation to predict long-term outcomes after transcatheter aortic valve replacement, (in eng). *J Cardiovasc Comput Tomogr.* (2022) 16:254–61. doi: 10.1016/j.jct.2021.11.014
21. Hellmeier, F, Brüning, J, Sündermann, S, Jarmatz, L, Schafstedde, M, Goubergrits, L, et al. Hemodynamic modeling of biological aortic valve replacement using preoperative data only, (in eng). *Front Cardiovasc Med.* (2020) 7:593709. doi: 10.3389/fcvm.2020.593709
22. Yevtushenko, P, Hellmeier, F, Bruening, J, Nordmeyer, S, Falk, V, Knosalla, C, et al. Surgical aortic valve replacement: are we able to improve hemodynamic outcome?, (in eng). *Biophys J.* (2019) 117:2324–36. doi: 10.1016/j.bpj.2019.07.025
23. Youssefi, P, Gomez, A, He, T, Anderson, L, Bunce, N, Sharma, R, et al. Patient-specific computational fluid dynamics-assessment of aortic hemodynamics in a spectrum of aortic valve pathologies, (in eng). *J Thorac Cardiovasc Surg.* (2017) 153:8–20.e3. doi: 10.1016/j.jtcvs.2016.09.040
24. Doost, SN, Ghista, D, Su, B, Zhong, L, and Morsi, YS. Heart blood flow simulation: a perspective review, (in eng). *Biomed Eng Online.* (2016) 15:101. doi: 10.1186/s12938-016-0224-8
25. Frauenfelder, T, Boutsianis, E, Alkadhi, H, Marincek, B, and Schertler, T. Simulation of blood flow within the abdominal aorta computational fluid dynamics in abdominal aortic aneurysms before and after interventions. *Radiologe.* (2007) 47:1021–8. doi: 10.1007/s00117-007-1576-7
26. Gerrah, R, and Haller, SJ. Computational fluid dynamics: a primer for congenital heart disease clinicians, (in eng). *Asian Cardiovasc Thorac Ann.* (2020) 28:520–32. doi: 10.1177/0218492320957163
27. Su, B, Zhang, JM, Zou, H, Ghista, D, Le, TT, and Chin, C. Generating wall shear stress for coronary artery in real-time using neural networks: feasibility and initial results based on idealized models, (in eng). *Comput Biol Med.* (2020) 126:104038. doi: 10.1016/j.combiomed.2020.104038
28. Yevtushenko, P, Goubergrits, L, Gundelwein, L, Setio, A, Ramm, H, Lamecker, H, et al. Deep learning based centerline-aggregated aortic hemodynamics: an efficient alternative to numerical Modelling of hemodynamics, (in eng). *IEEE J Biomed Health Inform.* (2021) 26:1815–25. doi: 10.1109/jbhi.2021.3116764
29. Jordanski, M, Radovic, M, Milosevic, Z, Filipovic, N, and Obradovic, Z. Machine learning approach for predicting wall shear distribution for abdominal aortic aneurysm and carotid bifurcation models, (in eng). *IEEE J Biomed Health Inform.* (2018) 22:537–44. doi: 10.1109/jbhi.2016.2639818
30. Vahanian, A, Beyersdorf, F, Praz, F, Milojevic, M, Baldus, S, Bauersachs, J, et al. 2021 ESC/EACTS guidelines for the management of valvular heart disease, (in eng). *EuroIntervention.* (2022) 17:e1126–96. doi: 10.4244/eij-e-21-00009
31. Hoeijmakers, M, Waechter-Stehle, I, Weese, J, and Van de Vosse, FN. Combining statistical shape modeling, CFD, and meta-modeling to approximate the patient-specific pressure-drop across the aortic valve in real-time, (in eng). *Int J Numer Method Biomed Eng.* (2020) 36:e3387. doi: 10.1002/cnm.3387
32. Franke, B, Brüning, J, Yevtushenko, P, Dreger, H, Brand, A, Juri, B, et al. Computed tomography-based assessment of Transvalvular pressure gradient in aortic stenosis, (in eng). *Front Cardiovasc Med.* (2021) 8:706628. doi: 10.3389/fcvm.2021.706628
33. Bernoulli-based pressure drop estimates: a comparison using patient anatomies from heart and aortic valve segmentation of CT images, (in eng). *Med Phys.* (2017) 44:2281–92. doi: 10.1002/mp.12203
34. Abraham, F, Behr, M, and Heinkenschloss, M. Shape optimization in steady blood flow: a numerical study of non-Newtonian effects. *Comput Methods Biomech Biomed Engin.* (2005) 8:127–37. doi: 10.1080/10255840500180799
35. Goubergrits, L, Riesenkampff, E, Yevtushenko, P, Schaller, J, Kertzscher, U, Hennemuth, A, et al. MRI-based computational fluid dynamics for diagnosis and treatment prediction: clinical validation study in patients with coarctation of aorta, (in eng). *J Magn Reson Imaging.* (2015) 41:909–16. doi: 10.1002/jmri.24639
36. Daley, PJ, Sagar, KB, and Wann, LS. Doppler echocardiographic measurement of flow velocity in the ascending aorta during supine and upright exercise, (in eng). *Br Heart J.* (1985) 54:562–7. doi: 10.1136/hrt.54.6.562
37. Ennezat, PV, Maréchaux, S, Iung, B, Chauvel, C, Lejemtel, TH, and Pibarot, P. Exercise testing and exercise stress echocardiography in asymptomatic aortic valve stenosis, (in eng). *Heart.* (2009) 95:877–84. doi: 10.1136/hrt.2008.150011
38. Gardin, JM, Kozlowski, J, Dabestani, A, Murphy, M, Kusnick, C, Allie, A, et al. Studies of Doppler aortic flow velocity during supine bicycle exercise, (in eng). *Am J Cardiol.* (1986) 57:327–32. doi: 10.1016/0002-9149(86)90913-6
39. Maréchaux, S, Hachicha, Z, Bellouin, A, Dumesnil, JG, Meimoun, P, Pasquet, A, et al. Usefulness of exercise-stress echocardiography for risk stratification of true asymptomatic patients with aortic valve stenosis, (in eng). *Eur Heart J.* (2010) 31:1390–7. doi: 10.1093/eurheartj/ehq076
40. Bollache, E, Fedak, PWM, van Ooij, P, Rahman, O, Malaisrie, SC, McCarthy, PM, et al. Perioperative evaluation of regional aortic wall shear stress patterns in patients undergoing aortic valve and/or proximal thoracic aortic replacement, (in eng). *J Thorac Cardiovasc Surg.* (2018) 155:2277–2286.e2. doi: 10.1016/j.jtcvs.2017.11.007
41. McClarty, D, Ouzounian, M, Tang, M, Eliathamby, D, Romero, D, Nguyen, E, et al. Ascending aortic aneurysm haemodynamics are associated with aortic wall biomechanical properties, (in eng). *Eur J Cardiothorac Surg.* (2022) 61:367–75. doi: 10.1093/ejcts/ezab471
42. Salmasi, MY, Pirola, S, Sasidharan, S, Fisichella, SM, Redaelli, A, Jarrai, OA, et al. High Wall shear stress can Predict Wall degradation in ascending aortic aneurysms: an integrated biomechanics study, (in eng). *Front Bioeng Biotechnol.* (2021) 9:750656. doi: 10.3389/fbioe.2021.750656
43. van Ooij, P, Markl, M, Collins, JD, Carr, JC, Rigsby, C, Bonow, RO, et al. Aortic valve stenosis alters expression of regional Aortic Wall shear stress: new insights from a 4-dimensional flow magnetic resonance imaging study of 571 subjects (in eng). *J Am Heart Assoc.* (2017) 6:5959. doi: 10.1161/jaha.117.005959
44. The MathWorks. *trainAutoencoder.* (2023). Available at: <https://www.mathworks.com/help/deeplearning/ref/trainautoencoder.html>.
45. Wellek, S. Introduction In: R Calver, editor. *Testing statistical hypotheses of equivalence and noninferiority*, Vol. 1. London: Chapman & Hall/CRC (2010). 10–1.
46. Wellek, S. Equivalence tests for paired observations In: R Calver, editor. *Testing statistical hypotheses of equivalence and noninferiority*, vol. 5. London: Chapman & Hall/CRC (2010). 99–106.
47. Medical electrical equipment - part 2-34: Particular requirements for the basic safety and essential performance of invasive blood pressure monitoring equipment IEC (2011).
48. Kutz, JN. Deep learning in fluid dynamics. *J Fluid Mech.* (2017) 814:1–4. doi: 10.1017/jfm.2016.803
49. Liang, L, Mao, W, and Sun, W. A feasibility study of deep learning for predicting hemodynamics of human thoracic aorta, (in eng). *J Biomech.* (2020) 99:109544. doi: 10.1016/j.biomech.2019.109544
50. Dey, D, Slomka, PJ, Leeson, P, Comaniciu, D, Shrestha, S, Sengupta, PP, et al. Artificial intelligence in cardiovascular imaging: JACC state-of-the-art review, (in eng). *J Am Coll Cardiol.* (2019) 73:1317–35. doi: 10.1016/j.jacc.2018.12.054

51. Kim, Y, Park, JY, Hwang, EJ, Lee, SM, and Park, CM. Applications of artificial intelligence in the thorax: a narrative review focusing on thoracic radiology, (in eng). *J Thorac Dis.* (2021) 13:6943–62. doi: 10.21037/jtd-21-1342
52. Otaki, Y, Miller, RJH, and Slomka, PJ. The application of artificial intelligence in nuclear cardiology, (in eng). *Ann Nucl Med.* (2022) 36:111–22. doi: 10.1007/s12149-021-01708-2
53. Tomov, ML, Perez, L, Ning, L, Chen, H, Jing, B, Minge, A, et al. A 3D bioprinted in vitro model of pulmonary artery atresia to evaluate endothelial cell response to microenvironment, (in eng). *Adv Healthc Mater.* (2021) 10:e2100968. doi: 10.1002/adhm.202100968
54. Annabi, MS, Touboul, E, Dahou, A, Burwash, IG, Bergler-Klein, J, Enriquez-Sarano, M, et al. Dobutamine stress echocardiography for Management of low-flow, low-gradient aortic stenosis, (in eng). *J Am Coll Cardiol.* (2018) 71:475–85. doi: 10.1016/j.jacc.2017.11.052
55. Picano, E, Pibarot, P, Lancellotti, P, Monin, JL, and Bonow, RO. The emerging role of exercise testing and stress echocardiography in valvular heart disease, (in eng). *J Am Coll Cardiol.* (2009) 54:2251–60. doi: 10.1016/j.jacc.2009.07.046
56. Baumgartner, H, Stefenelli, T, Niederberger, J, Schima, H, and Maurer, G. “Overestimation” of catheter gradients by Doppler ultrasound in patients with aortic stenosis: a predictable manifestation of pressure recovery, (in eng). *J Am Coll Cardiol.* (1999) 33:1655–61. doi: 10.1016/s0735-1097(99)00066-2
57. Nordmeyer, S, Hellmeier, F, Yevtushenko, P, Kelm, M, Lee, CB, Lehmann, D, et al. Abnormal aortic flow profiles persist after aortic valve replacement in the majority of patients with aortic valve disease: how model-based personalized therapy planning could improve results. A pilot study approach, (in eng). *Eur J Cardiothorac Surg.* (2020) 57:133–41. doi: 10.1093/ejcts/ezz149
58. Johnston, L, Allen, R, Hall Barrientos, P, Mason, A, and Kazakidi, A. Hemodynamic abnormalities in the aorta of turner syndrome girls, (in eng). *Front Cardiovasc Med.* (2021) 8:670841. doi: 10.3389/fcvm.2021.670841
59. Kobsa, S, Akiyama, K, Nemeth, SK, Kurlansky, PA, Naka, Y, Takeda, K, et al. Correlation between aortic valve protein levels and vector flow mapping of wall shear stress and oscillatory shear index in patients supported with continuous-flow left ventricular assist devices, (in eng). *J Heart Lung Transplant.* (2023) 42:64–75. doi: 10.1016/j.healun.2022.09.017
60. Liu, J, Shar, JA, and Sucosky, P. Wall shear stress directional abnormalities in BAV aortas: toward a new hemodynamic predictor of aortopathy?, (in eng). *Front Physiol.* (2018) 9:993. doi: 10.3389/fphys.2018.00993
61. Petuchova, A, and Maknickas, A. Computational analysis of aortic haemodynamics in the presence of ascending aortic aneurysm, (in eng). *Technol Health Care.* (2022) 30:187–200. doi: 10.3233/thc-219002
62. Chen, C, Qin, C, Qiu, H, Tarroni, G, Duan, J, Bai, W, et al. Deep learning for cardiac image segmentation: a review, (in eng). *Front Cardiovasc Med.* (2020) 7:25. doi: 10.3389/fcvm.2020.00025

3.5 Optimierung: Nutzen synthetischer Patientenkollektive zum Überwinden existierender klinischer Datenlücken

Um ein künstliches neuronales Netz erfolgreich zu trainieren, bedarf es einer großen Menge an klinischen Daten, auf deren Grundlage der Algorithmus „lernen“ kann. Diese steht jedoch, insbesondere in der Kinderkardiologie, häufig nicht zur Verfügung. Die nachfolgende Arbeit stellt daher einen methodischen Ansatz zur Augmentierung verfügbarer klinischer Daten vor. Sie zeigt unter anderem, wie mit Hilfe von synthetischen Trainingsdaten die Vorhersagegenauigkeit des künstlichen neuronalen Netzes erhöht werden kann.

Deep Learning Based Centerline-Aggregated Aortic Hemodynamics: An Efficient Alternative to Numerical Modeling of Hemodynamics

Pavlo Yevtushenko, Leonid Goubergrits, Lina Gundelwein, Arnaud Setio, Heiko Ramm, Heiko Lamecker, Tobias Heimann, Alexander Meyer, Titus Kühne, **Marie Schafstedde**

Der nachfolgende Text entspricht inhaltlich dem Abstrakt der oben genannten Publikation als Übersetzung durch die Autorin:

„Die bildgestützte patientenspezifische Modellierung der Hämodynamik wird zunehmend häufig als Lösung für Diagnostik und Ergebnisvorhersage bei einer Vielzahl von Herz-Kreislauf-Erkrankungen angewandt. Ihr Potential zur Verbesserung der diagnostischen Möglichkeiten und damit der klinischen Ergebnisse ist zwar weithin anerkannt, dennoch erfordern diese Methoden beträchtliche Rechenressourcen, da sie meist auf konventionellen numerischen Methoden wie der computergestützten Strömungssimulation (CFD) beruhen.“

*Als Alternative zu den numerischen Methoden schlagen wir einen auf maschinellem Lernen (ML) basierenden Ansatz zur Berechnung patientenspezifischer hämodynamischer Parameter vor. Im Vergleich zu CFD-basierten Methoden hat dieser Ansatz den Vorteil, dass er mit geringem Rechen- und Zeitaufwand ein patientenspezifisches hämodynamisches Ergebnis berechnen kann. In dieser „Proof-of-Concept“ Studie stellen wir ein künstliches neuronales Netz (ANN) vor, das in der Lage ist, die aortale Hämodynamik von Patient*innen mit Aortenisthmusstenose in Echtzeit zu berechnen.“*

In Anbetracht des komplexen Zusammenhangs zwischen Gefäßform und Hämodynamik einerseits und der begrenzten Verfügbarkeit geeigneter klinischer Daten andererseits, kann eine ausreichende Genauigkeit des ANN mit den verfügbaren Daten allein jedoch nicht erreicht werden. Ein weiterer

Schlüsselaspekt dieser Studie ist daher die erfolgreiche Augmentierung der verfügbaren klinischen Daten. Mit Hilfe eines statistischen Formmodells wurden zusätzliche, „synthetische“ Trainingsdaten generiert, die die Genauigkeit des ANN deutlich erhöhten.

Dies zeigt die Fähigkeit ML-basierter Methoden, in silico Modellierungsaufgaben in Echtzeit durchzuführen, die zuvor ressourcenintensive CFD-Simulationen erforderten.“

Verweis auf Originalarbeit 5 (Seiten 72 - 84 der Habilitationsschrift)

IEEE Journal of Biomedical and Health Informatics 2022 Apr;26(4):1815-1825.

<https://doi.org/10.1109/jbhi.2021.3116764>

**Deep Learning Based Centerline-Aggregated Aortic Hemodynamics: An Efficient Alternative to
Numerical Modeling of Hemodynamics**

Yevtushenko P, Goubergrits L, Gundelwein L, Setio A, Ramm H, Lamecker H, Heimann T, Meyer A,
Kuehne T, **Schafstedde M**

4. Diskussion

Die Ziele der in dieser Habilitationsschrift vorgelegten wissenschaftlichen Arbeiten waren die Vorstellung möglicher Ansätze zur bildbasierten *in silico* Modellierung der patientenindividuellen Hämodynamik^{9,19} sowie deren klinische Validierung.¹⁹ Am Beispiel von kinderkardiologischen Patient*innen mit komplexer univentrikulärer Physiologie folgte sodann eine erste klinische Anwendung der virtuellen Therapieplanung.²⁰ Zuletzt wurden zwei Ansätze für eine bessere klinische Translation vorgestellt: 1) der Einsatz von künstlicher Intelligenz als Alternative zu computergestützten Strömungssimulationen²¹ und 2) der Nutzen synthetischer Patientenkollektive zum Überwinden existierender klinischer Datenlücken.²²

4.1 Bildbasierte *in silico* Modellierung hämodynamischer Parameter

Die erste Originalarbeit beschreibt einen Arbeitsablauf, mit dessen Hilfe es möglich ist, basierend auf rein präoperativer Bildgebung Parameter der postoperativen Hämodynamik vorherzusagen. Grundlage hierfür waren präoperative 4D-Fluss MRT-Daten, aus denen Informationen zu Geometrie und Flussbedingungen abgeleitet werden konnten. Als Patientenkollektiv wurden 10 Patient*innen mit AS und Indikation zum biologischen AKE gewählt. Für all diese Patient*innen wurde neben der tatsächlich durchgeföhrten Operation zusätzlich ein virtueller AKE durchgeföhrte. Der virtuelle AKE wurde dabei von einem erfahrenen Kardiochirurgen durchgeföhrte. Er hatte die Aufgabe, die Aortenklappe einerseits an ihren Nadir-Punkten und Kommissuren innerhalb des Aortenbogens richtig zu positionieren, andererseits aber auch für jede Patient*in eine passende Prothesengröße auszuwählen. Basierend auf der nun geschaffenen Anatomie wurde sodann eine numerische Strömungssimulation durchgeföhrte und verschiedene Parameter der aortalen Hämodynamik quantifiziert. Diese Ergebnisse wurden verglichen mit der tatsächlichen postoperativen Hämodynamik.

Wir konnten zeigen, dass zwischen den Parametern der maximalen Geschwindigkeit und des Druckgradienten eine gute Übereinstimmung bestand. Im klinischen Kontext wäre man damit also ggf. in der Lage, die postoperative Klappenprothesenleistung abzuschätzen und so bereits präoperativ Patient*innen mit einem erhöhten Risiko für ein PPM zu identifizieren.

Wie eingangs erwähnt ist es insbesondere die Kombination aus einer kleinen Prothesengröße und einer großen Körperoberfläche der Patient*in, die durch eine niedrige indizierte

Klappenöffnungsfläche gekennzeichnet ist, welche zu einem besonders ausgeprägten PPM führt. Eine zu kleine Prothesengröße wird dabei als entscheidende Stellschraube zur Verbesserung des PPM diskutiert.⁴² Es existieren bereits erste Empfehlungen für die optimale Klappenöffnungsfläche der zu implantierenden Aortenklappe, die mit möglichst niedrigen postoperativen Druckgradienten und Flussgeschwindigkeiten einhergeht.⁶⁷⁻⁶⁹

Unsere Studie zeigte jedoch ebenfalls, dass sich der Chirurg im Rahmen des virtuell durchgeföhrten AKE häufiger für eine größere, als in der tatsächlichen Operation gewählten, Klappenprothese entschieden hat. Da die Implantation einer größeren Aortenklappe in der Regel jedoch mit einer Erweiterung des operativen Eingriffes einhergeht (Aortenarulus und -ascendenserweiterung, längere Operationszeiten) gilt es die Risiken einer längeren und größeren Operation gegen das Risiko eines postoperativ bestehenden PPM abzuwägen.

Entscheidungsunterstützungssysteme wie zum Beispiel ein in klinische Bildgebungssysteme integriertes Tool zur bildbasierten *in silico* Modellierung verschiedener Therapieoptionen könnten hier in jedem Fall helfen, ein fundiertes Therapiekonzept mit möglichst geringem Risiko und gutem Resultat zu erarbeiten.

Aufgrund einiger technischer Vereinfachungen innerhalb der numerischen Strömungssimulation ist es uns gelungen, einen Arbeitsablauf zu entwickeln, der innerhalb eines akzeptablen Zeitraumes (ca. eine Woche pro Patient*in für die Segmentierung der individuellen Geometrie, die virtuelle Intervention und die Simulation der Hämodynamik) durchgeführt werden kann. Allerdings ist dieser Arbeitsablauf für komplexere Blutflussprofile, wie zum Beispiel die Wandparallelität des aortalen Blutflusses oder die Flussexzentrizität, welche ebenfalls nach operativem AKE persistieren können³⁴, nicht ideal.

Für die klinische Translation ist zudem eine Validierung gegen deutlich größere klinische Kohorten notwendig, um die Robustheit und Zuverlässigkeit der entwickelten Methoden zu belegen und so für die Klinik ein größeres Vertrauen zu schaffen.

4.2 Validierung gegen den klinischen Goldstandard des Herzkatheters

Die Motivation für die zweite Originalarbeit war eine solche klinische Validierung. Es erfolgte ein Vergleich der bildbasierten *in silico* Modellierung mit dem klinischen Goldstandard des Herzkatheters. Konkret wurde dabei der transvalvuläre Druckgradient (TPG) auf Grundlage von CT-Daten simuliert und im Anschluss mit invasiv (Herzkatheter) gemessenen Druckgradienten verglichen.

Die Validierung erfolgte an insgesamt 84 Patient*innen mit Aortenstenose, die vor einer geplanten Transkatheter Aortenklappenimplantation (TAVI) eine CT-Bildgebung sowie eine diagnostische Herzkatheteruntersuchung und eine Echokardiographie erhielten. Es zeigte sich eine gute Übereinstimmung (mittlerer Unterschied von 2.6 ± 19.3 mmHg) sowie eine gute Korrelation ($r=0.72$, $p<0.001$) zwischen der bildbasierten Modellierung des TPG und dem klinischen Goldstandard der invasiven Druckmessung.

Das Besondere der bildbasierten Modellierung war hierbei die Tatsache, dass auf Grundlage von CT-Daten, welche in der Regel für die Beurteilung anatomischer Strukturen genutzt werden, funktionelle Parameter der aortalen Hämodynamik quantifiziert wurden. Anders als in der ersten Originalarbeit, in der aus 4D Fluss MRT-Daten Informationen über Geometrie und Flussvolumina gewonnen wurden, wurden in der zweiten Originalarbeit dynamische CT-Untersuchungen verwendet. Dabei wurde das linksventrikuläre Volumen für jede aufgenommene Zeitsequenz segmentiert und der spitzensystolische Volumenfluss dann durch Berechnung der linksventrikulären Volumenänderung zwischen den jeweiligen Zeitsequenzen und Division der Differenz durch die zeitliche Auflösung der CT-Bilder quantifiziert. So waren wir in der Lage, auch aus CT-Daten Informationen über Geometrie und Hämodynamik zu gewinnen und damit eine bildbasierte Modellierung des transvalvulären Druckgradienten über eine stenotische Aortenklappe zu realisieren. Das CT könnte so als universales Diagnostikum genutzt werden, sowohl zur Bestimmung anatomischer Gegebenheiten (Zugangsweg, Klappenöffnungsfläche) als auch zur Quantifizierung hämodynamischer Parameter (TPG) vor einem geplanten AKE, wodurch sich die diagnostische Aussagekraft dieser Bildgebungsmethode in der präoperativen Therapieplanung erhöht. In diesem Kontext sind auch weitere CT-basierte Funktionsmessungen zu erwähnen, die in den letzten Jahren für kardiovaskuläre Anwendungen etabliert wurden: die bildbasierte Messung der myokardialen Perfusion^{70,71} oder die Berechnung der fraktionellen Flussreserve bei Patient*innen mit koronarer Herzkrankheit.^{2,72}

Nichts desto trotz bleibt die nichtinvasive und ubiquitär verfügbare Untersuchungsmethode der Echokardiographie das Mittel der ersten Wahl im diagnostischen Abklärungsprozess von Patient*innen mit AS.⁷³ Dabei ist es insbesondere die Einteilung der Stenose in verschiedene Schweregrade, die für die weitere klinischen Planung essentiell ist.⁵⁵ Diese Einteilung basiert derzeit entweder auf der Aortenklappenöffnungsfläche (AVA) oder dem transvalvulären Druckgradienten (TPG). Außer für die planimetrische Quantifizierung der AVA werden zur Kalkulation dieser Parameter verschiedene mathematische Gleichungen zu Grunde gelegt: Die Bernoulli-Gleichung zur Berechnung des TPG oder die Kontinuitätsgleichung zur Berechnung der AVA.

Während die Anwendung der Bernoulli-Gleichung für ihre systematische Überschätzung im Vergleich zur invasiven Druckmessung bekannt ist⁷⁴, erfordert die Anwendung der Kontinuitätsgleichung zusätzlich die Messung der Querschnittsflächen des linksventrikulären Ausflusstraktes und der Aorta Ascendens, wodurch die Ungenauigkeit dieser Methode ebenfalls steigt. Unsicherheiten von bis zu 30% werden im Rahmen der echobasierten Schweregradeinteilung der AS berichtet.^{75,76} Darüber hinaus ist auch die Untersucherabhängigkeit ein nicht zu vernachlässigendes Problem.⁷⁷ Ein weiterer Aspekt der in der zweiten Originalarbeit vorgestellten Studie war ein Vergleich zwischen Herzkatheter- und Echokardiographie-basierter Druckmessung. Auch wir konnten eine leichte Überschätzung in der Echokardiographie-basierten Druckmessung verzeichnen bei einer insgesamt akzeptablen Korrelation mit den Herzkatheter-basierten Druckmessungen. Dieses Ergebnis ist kongruent mit anderen Studien, die sich auf den Vergleich dieser beiden Untersuchungsmethoden konzentrieren.⁷⁸

Aufgrund der methodischen Ungenauigkeiten innerhalb der Echokardiographie einerseits, und der Tatsache, dass es die Herzkatheteruntersuchung ist, die als klinischer Goldstandard für die exakte Bestimmung des transvalvulären Druckgradienten anerkannt ist andererseits, erfolgte die Validierung unserer CT-basierten TPG-Quantifizierung ausschließlich gegen die invasiv gemessenen Druckwerte. Mit einer konsistenten Einstufung des AS-Schweregrads in 92% aller Fälle schnitt der CT-basierte Modellierungsansatz in dieser Hinsicht sogar außergewöhnlich gut ab.

4.3 Klinische Anwendung der virtuellen Therapieplanung

An einem gänzlich unterschiedlichen Patientenkollektiv aus dem Bereich der Kinderkardiologie erfolgte in der dritten Originalarbeit eine erste konkrete klinische Anwendung der bildbasierten *in silico* Modellierung.

Dabei wurden konkrete Patientenfälle aus der Klinik vorgestellt, für die im Rahmen interdisziplinärer Teamsitzungen bestehend aus Kinderkardiolog*innen, Kinderkardiochirurg*innen und Ingenieur*innen individuelle Behandlungsoptionen erarbeitet wurden.

Fontan-Patient*innen sind ein sehr heterogenes Patientenkollektiv mit unterschiedlichen, jedoch immer sehr komplexen angeborenen Herzfehlern. Diese Herzfehler sind so schwer, dass es keine kurativen Behandlungsansätze gibt, sondern lediglich eine Palliation nach dem Fontan-Prinzip. Dabei wird, wie in der Einleitung bereits kurz erläutert, eine Kreislaufsituation geschaffen, bei der sowohl der Lungen als auch der Systemkreislauf nicht mehr parallel zueinander, sondern in Serie geschaltet

sind. Die pulmonale Perfusion wird also nicht mehr durch den rechten Ventrikel gewährleistet, sondern es wird eine Verbindung zwischen dem systemvenösen Blut und den Pulmonalarterien geschaffen, sodass das Blut passiv am rechten Herzen vorbei direkt in die Lunge geleitet wird. Diese sogenannte totale kavopulmonale Verbindung (englisch total cavopulmonary connection, TCPC) hat zum Ziel, die Volumenbelastung des Univentrikels zu reduzieren sowie die Zyanose zu beseitigen, die aufgrund bestehender Rechts-Links Shuntverbindungen zwangsläufig existiert.⁷⁹

In Folge einer kontinuierlichen Verbesserung der chirurgischen Techniken sowie der perioperativen Betreuung erreichen Fontan-Patient*innen heute immer häufiger das Erwachsenenalter. Allerdings nehmen damit auch die Langzeitkomplikationen zu. Ein Beispiel ist die Entwicklung sogenannter pulmonaler arteriovenöser Malformationen (PAVM), die vermutlich aufgrund eines fehlenden oder ungleich verteilten hepatovenösen Blutflusses in die Lungenarterien entstehen. Sind solche PAVM erst einmal entstanden, leiden die Patient*innen unter einer Zyanose, wodurch ihre körperliche Belastbarkeit und letztlich auch ihre Lebenserwartung eingeschränkt sind.

Die besondere Herausforderung ist hier, chirurgische oder interventionelle Behandlungsoptionen zu identifizieren, die in einer gleichmäßigeren Verteilung des hepatovenösen Blutes resultieren. Dabei sind es insbesondere die sehr komplexen anatomischen Gegebenheiten, für die virtuelle Behandlungssimulationen von außerordentlich hohem klinischem Interesse sind.

Grundlage der dritten Originalarbeit war die Erarbeitung und Simulation verschiedener interventioneller und/ oder chirurgischer Behandlungsoptionen für drei Patient*innen mit PAVM. Dafür wurden sowohl MRT- als auch CT-Daten genutzt und die patientenindividuelle Anatomie segmentiert. Sodann wurden verschiedene Therapieoptionen simuliert, die im Rahmen einer chirurgischen Besprechung als möglich identifiziert wurden. Jede Option wurde mittels CFD simuliert und die Flussverteilung des hepatovenösen Blutes quantifiziert. Die methodischen Ansätze variierten dabei von virtuellem Stenting über virtuelle Implantation von Gefäßgrafts bis hin zu virtuellen Re-Anastomosierungen. Zum Teil wurde sogar eine hybride Modellierung mit Überlagerung von MRT- und CT-Daten angewandt, da es aufgrund metallischer Implantate zum Teil zu erheblichen Auslöschen oder Artefakten sowohl in der einen als auch in der anderen Bildgebungsmodalität kam.

Die virtuelle Simulation der präinterventionellen Blutflussverteilung stimmte in allen drei Fällen gut mit der tatsächlichen angiografischen Quantifizierung der hepatovenösen Blutflussverteilung überein. Dies unterstreicht die Aussage anderer Forschungsgruppen, dass die numerische Simulation der präinterventionellen Hämodynamik im Fontan-Kreislauf prinzipiell möglich ist.⁸⁰

Für eine der drei Patient*innen lagen uns zusätzlich postoperative Daten vor, sodass eine Art Validierung zwischen der präoperativ virtuell geplanten und der tatsächlich durchgeführten Therapie möglich war. Die virtuelle Strömungssimulation und die MRT-basierte Flussmessung nach durchgeföhrter Operation wichen hierbei um 15% voneinander ab.

Für eine bessere Einordnung dieser Ergebnisse ist ein Vergleich zu anderen Forschungsgruppen und eine Darstellung der aktuellen Wissenschaftslage nötig: Während es heutzutage zwar vielversprechende Berichte zur virtuellen Fontan-Therapieplanung gibt, sind diese Erfahrungen doch sehr begrenzt, insbesondere was die zugrunde liegende Patientenzahl betrifft.

Insgesamt konnten bereits der Nutzen der virtuellen Therapieplanung für die Beurteilung der präoperativen hämodynamischen Bedingungen und zur Identifizierung anatomischer Einschränkung innerhalb des Operationsfeldes gezeigt sowie zurückhaltende Vorhersagen über die postoperative Hämodynamik getroffen werden, wenn prä- und postoperative Anatomie nicht zu stark voneinander abwichen.^{13,81-83} Sundareswaran et al. waren dabei die Ersten, die die Durchführbarkeit der virtuellen chirurgischen Therapieplanung zur Korrektur von PAVM im Jahr 2009 beschrieben, konzentrierten sich in ihrer Arbeit jedoch auf einen einzigen Fallbericht ohne postoperative Bildgebungsdaten zur Validierung ihrer simulierten Vorhersagen.⁸⁴ 2012 verglichen Haggerty et al. anhand von vier Patient*innen erfolgreich die Flussverteilung des hepatovenösen Blutes zwischen dem vorhergesagten und dem postoperativen Zustand.⁶⁶ Trusty et al. führten 2019 schließlich die erste prospektive chirurgische Follow-Up Studie an 12 Fontan-Patient*innen durch, in der die Vorhersagegenauigkeit der virtuellen Flussquantifizierung des Lebervenenblutes im Vergleich zum realen postoperativen Operationsergebnis analysiert wurde.⁸⁵ Sie veröffentlichten dabei eine der größten Patientenkohorten und verfügen sicherlich über eine große und langjährige Expertise auf diesem Forschungsgebiet, betonen aber auch die Notwendigkeit einer ausreichend guten Bildqualität als eine der wichtigsten Voraussetzungen für die Durchführbarkeit der virtuellen Therapieplanung.

Die methodische Stärke der hier vorgelegten dritten Originalarbeit ist dabei die Vorstellung eines Ansatzes, mit dessen Hilfe es möglich ist, auch komplexe Fontan-Fälle mit artefaktreicher Bildqualität zu integrieren, da es insbesondere diese Patient*innen sind, die von individuellen virtuellen Therapieplanungsansätzen am meisten profitieren.

Während es sicherlich noch einiger Verbesserungen bedarf, insbesondere einer Validierung anhand größerer Patientenkohorten sowie einer besseren Standardisierung des Prozesses, um den hier präsentierten Ansatz der virtuellen Therapieplanung in die klinische Routine zu integrieren, hat die Kombination moderner Simulationsmethoden mit bildgebenden Verfahren bereits jetzt das Potential,

die patientenspezifische Therapieplanung bei Patient*innen mit ausgeprägtem hepatovenösem Flussmismatch und PAVM zu verbessern.

4.4 Einsatz von künstlicher Intelligenz anstelle numerischer Strömungssimulationen für eine bessere klinische Translation

Die Durchführbarkeit, die Vorteile und der klinische Bedarf an bildbasierter *in silico* Modellierung wurden in den ersten drei Originalarbeiten gezeigt. Unterschiedliche methodische Ansätze wurden dabei vorgestellt, validiert und im klinischen Kontext angewendet. Allen Ansätzen gemein ist jedoch die Tatsache, dass sie eine hohe technische Expertise verlangen und zusätzlich sehr zeit- und rechenleistungsintensiv sind. So gut wie kein numerisches Strömungssimulationsverfahren zur Berechnung häodynamischer Parameter hat es bislang geschafft, in ein Medizinprodukt umgesetzt und damit für den klinischen Gebrauch nutzbar gemacht zu werden. Die bekannteste Ausnahme ist das Medizintechnik-Unternehmen HeartFlow®, welches mit seinem Ansatz, die patientenspezifische Flussrate in erkrankten Herzkranzgefäßen aus Computer-Tomographie Daten zu berechnen, die Hürde der klinischen Translation für die modellbasierte Präzisionsmedizin genommen hat.

Hintergrund der vierten in dieser Habilitationsschrift vorgestellten Originalarbeit ist der Einsatz von künstlicher Intelligenz (KI) anstelle numerischer Strömungssimulationen für eine bessere klinische Translation der modellbasierten Behandlungsunterstützung. Wenn einmal trainiert, haben KI-basierte Algorithmen das Potential, häodynamische Ergebnisse schnell zu berechnen, ohne dass dafür eine hohe technische Expertise oder außergewöhnliche Rechenkapazitäten vorausgesetzt wären. In Anbetracht der Tatsache, dass in der Klinik nur selten ein Zugang zu High-End Computern besteht und Diagnose- sowie Behandlungsplanung in der Regel schnell erfolgen müssen, haben die genannten Vorteile ein besonderes Gewicht.

Im Rahmen der vierten Originalarbeit haben wir daher ein künstliches neuronales Netz (ANN) zur Vorhersage verschiedener Parameter der aortalen Häodynamik am Anwendungsfall der Aortenklappenstenose (AS) entwickelt und validiert.

Grundlage hierfür waren 103 zeitlich aufgelöste CT-Datensätze von Patient*innen mit AS und Indikation zum AKE. Aus den CT-Datensätzen wurden dann patientenspezifische Oberflächen des linksventrikulären Ausflusstraktes, der Aortenklappe und des Aortenbogens mittels eines semi-automatisierten Segmentierungsablaufes erstellt, der bereits im Rahmen der zweiten Originalarbeit für die Segmentierung angewendet wurde.¹⁹ Basierend auf den segmentierten Geometrien und den vorhandenen Flussinformationen der dynamischen CT-Untersuchung wurden dann computergestützte

Strömungssimulationen durchgeführt und der Druckgradient sowie die Wandschubspannung (WSS) über der Aortenklappe quantifiziert.

Da für ein erfolgreiches Trainieren eines ANN in der Regel viele Daten benötigt werden, wurden zusätzliche CFD-Simulationen mit verändertem Volumenfluss durchgeführt. Der Volumenfluss wurde hierbei um $\pm 25\%$ des jeweiligen spitzensystolischen Flusses variiert. Dies entspricht den Literaturdaten über belastungsinduzierte Veränderungen des systolischen Spitzenflusses.^{86,87} Durch die Varianz des Volumenflusses waren wir in der Lage, aus den initialen 103 Datensätzen, 309 Strömungssimulationen zu erzeugen.

Diese 309 Simulationen wurden in einem weiteren Schritt in 11 Datensätze aufgeteilt, von denen zehn zum Trainieren, Validieren und Optimieren des ANN genutzt wurden und einer zum letztendlichen Testen des Algorithmus. Die Vorhersagegenauigkeit des entwickelten ANN wurde dann durch Ermittlung der Wurzel der mittleren Fehlerquadratsumme (englisch root-mean-square error, RMSE), ein Maß zur Beurteilung der Prognosegüte, geprüft. Dabei wurden die CFD- und ANN-basierten Simulationsergebnisse von TPG und WSS miteinander verglichen. Insgesamt konnten wir eine gute Übereinstimmung beider Methoden mit einer guten Vorhersagegenauigkeit des trainierten ANN zeigen. In absoluten Werten ergab sich ein RMSE von 2 mmHg (IQR 3.2 mmHg) für den Druckgradienten sowie 5.3 Pa (IQR 3.9 Pa) für die Wandschubspannung mit einer mittleren relativen Differenz zwischen beiden Methoden von 6.0 % für den Druckgradienten und 4.9 % für die Wandschubspannung.

Verschiedene Forschungsgruppen haben bereits das Potential KI-basierter Modellierungsmethoden zur Vorhersage funktioneller und hämodynamischer Parameter gezeigt. Als Beispiele seien die KI-basierte Bestimmung der WSS innerhalb von Koronararterien⁸⁸ oder abdominalen Aortenaneurysmen⁸⁹ oder aber die Quantifizierung von Druckgradienten und Geschwindigkeiten innerhalb der thorakalen Aorta⁹⁰ genannt. In der hier vorgestellten Originalarbeit haben wir den möglichen Einsatz von KI zur Modellierung hämodynamischer Parameter am Beispiel der Aortenklappenstenose gezeigt.

Integriert in ein CT oder ein MRT könnte ein solches ANN die diagnostische Aussagekraft der jeweiligen Bildgebungsmethode um behandlungskritische hämodynamische Informationen (wie zum Beispiel den Druckgradienten oder die Wandschubspannung) zusammen mit den Bilddaten in Echtzeit liefern. Dies könnte wiederum den Bedarf an invasiver Herzkatheterdiagnostik reduzieren und damit Kosten und Patientenrisiko senken. Außerdem könnte die Veränderung des Druckgradienten unter körperlicher Belastung simuliert werden, was insbesondere für Patienten mit Boderline-Symptomen

von großem klinischem Interesse wäre und ihnen eine zusätzliche Dobutamin-Stress Echokardiographie ersparen könnte.^{91,92}

4.5 Nutzen synthetischer Patientenkohorten zum Überwinden existierender klinischer Datenlücken

Ein weiteres Problem der klinischen Translation KI-basierter Modellierungsansätze ist das Fehlen ausreichend großer Patientenkohorten, um ein ANN zu trainieren. Kleinere klinische Bereiche, wie zum Beispiel die Kinderkardiologie, sind hiervon besonders schwer betroffen.

Das Hauptaugenmerk der letzten in dieser Habilitationsschrift vorgestellten Originalarbeit liegt auf dem Erzeugen synthetischer Patientenkohorten zur Augmentierung verfügbarer klinischer Daten. Klinisches Anwendungsbeispiel sind hierbei Patient*innen mit Aortenisthmusstenose.

Wie in der Einleitung bereits erwähnt, basiert das Erzeugen synthetischer Kohorten auf statistischen Formmodellen, welche zur systematischen Quantifizierung von Formvarianten genutzt werden. Mithilfe der Hauptkomponentenanalyse (principal component analysis, PCA) wurde der Trainingsdatensatz analysiert und die Richtungen der größten Formvariation definiert, sodass ein statistisches Formmodell entwickelt werden konnte, welches in der Lage war, jede Geometrie als eine Kombination aus der mittleren Form und den formspezifischen Parametern zu beschreiben. Dabei wurden etwaige Zusammenhänge zwischen verschiedenen Formparametern wie zum Beispiel dem Aortendurchmesser und der Aortenlänge, aber auch viele weniger offensichtliche geometrische Zusammenhänge vom statistischen Formmodell durch Korrelation ermittelt. Durch zufällige Kombination verschiedener Formparametervektoren entstanden so beliebig viele synthetische Geometrien. Dabei wurde gewährleistet, dass diese sich innerhalb der geometrischen Zusammenhänge befanden, die der realen Patientenkohorte zugrunde lagen. Zusätzlich wurde im Rahmen der fünften Originalarbeit eine statistische Analyse durchgeführt, mit der sichergestellt wurde, dass sich die generierten synthetischen Geometrien in einem realistischen Rahmen bezüglich des zugrunde liegenden Krankheitsbildes befanden. Es wurden Grenzwerte für bestimmte Formparameter definiert, wie zum Beispiel für den Stenosegrad der Aortenisthmusstenose oder die Länge der Stenose.

In einer Umfrage unter Kardiolog*innen, Kinderkardiolog*innen und Ingenieur*innen, denen wir insgesamt 20 verschiedene Aortenbogen-Geometrien vorgelegt haben, von denen etwa die Hälfte real und die andere Hälfte synthetisch waren, konnten wir zeigen, dass selbst die erfahrensten Kliniker*innen nicht in der Lage waren, die realen von den synthetischen Anatomien zu unterscheiden.

Mit einer „Trefferquote“ von durchschnittlich 55% glich das Ergebnis annähernd dem reinen Zufall. Auch ein statistischer Vergleich einzelner Formparameter ergab eine gute Übereinstimmung der realen mit der synthetischen Kohorte mit vergleichbaren Medianen und interquartile range- (IQR) Werten sowie eine niedrige relative Kullback-Leibler Divergenz (RKLD), ein Maß zur Beurteilung der Ähnlichkeit zwischen zwei Verteilungen.

Durch das Erzeugen der synthetischen Kohorte waren wir in der Lage, unseren realen Datensatz von 228 Patient*innen auf 3190 Geometrien zu erweitern. Dabei bestand die reale Patientenkollektion aus 143 Patient*innen mit ISTA sowie 85 gesunden Patient*innen, sodass das SSM auf einer breiten Ausgangsbasis lernen konnte. 37 reale Datensätze wurden dabei für das finale Testen des ANN zurückgehalten, während 3153 Datensätze demnach zum Trainieren des ANN zur Verfügung standen.

Neben der Tatsache, dass die synthetische Kohorte der realen in ihren geometrischen Eigenschaften sehr ähnlich war, konnten wir außerdem zeigen, dass sich die Vorhersagegenauigkeit des ANN erhöht, wenn es zum Trainieren sowohl auf reale als auch auf synthetische Daten zurückreifen kann. Um dies zu untersuchen, haben wir die Vorhersagegenauigkeit des ANN verglichen, nachdem es einmal ausschließlich mit realen Datensätzen trainiert worden war („Basis-ANN“) und in einem weiteren Schritt sowohl mit realen als auch mit synthetischen Daten („augmentiertes ANN“). Hämodynamische Parameter der aortalen Hämodynamik (wie zum Beispiel der Druckverlust über der Isthmusstenose oder die Wandschubspannung, WSS), welche mittels der zwei verschiedenen ANNs berechnet wurden, wurden gegen CFD-basierte Quantifizierungen verglichen. Die CFD-basierte Simulation fungierte hier also als sogenannte „ground truth“.

Der mittlere Vorhersagefehler des Druckverlustes für das Basis-ANN betrug 1.7 mmHg bei einer Standardabweichung (SD) von 14.7 mmHg, während der mittlere WSS-Verlaufsfehler 0.5 ± 4.6 Pa betrug. Durch Anwendung des augmentierten ANNs verbesserte sich die Standardabweichung des Gefäßdruckverlustfehlers auf 5.6 mmHg, obwohl der Mittelwert gleichblieb, beziehungsweise sogar auf 1.8 mmHg leicht anstieg. Der mittlere WSS-Verlaufsfehler verbesserte sich ebenfalls auf 0.2 ± 3.6 Pa.

Insgesamt lässt sich die erreichte Modellierungsgenauigkeit als gut bewerten und gleicht der in der Literatur beschriebenen Genauigkeit der invasiven Druckmessung von ca. ± 5 mmHg.^{93,94} Für die Genauigkeit der WSS gibt es leider keine konkreten Vergleichswerte. Vor dem Hintergrund jedoch, dass WSS im Bereich von 15-30 Pa erst zu Gefäßschäden führen^{95,96}, lässt sich die hier berechnete Genauigkeit von 0.2 ± 3.6 Pa ebenfalls als gut einschätzen.

Eine mögliche Limitation, die zu der doch nur moderaten Verbesserung der Vorhersagegenauigkeit des augmentierten ANNs geführt haben könnte, ist die gewählte Methode zur Erzeugung des SSM selbst. Durch Kombination der verschiedenen Formvektoren ergaben sich zwar neue Geometrien, allerdings wurde darauf geachtet, dass sich all diese innerhalb der geometrischen Zusammenhänge der realen Patientenkohorte befanden. Die „Andersartigkeit“ der synthetischen Kohorte wurde somit begrenzt, sodass das ANN aus den synthetischen Trainingsdaten ggf. nicht ausreichend viel Neues lernen konnte. Unser Hintergedanke dabei war das Bestreben, die synthetische Kohorte möglichst realitätsnah abzubilden. Die Analyse zur Vorhersagegenauigkeit des augmentierten ANN zeigte allerdings auch, dass es gerade bei geometrischen Grenz- bzw. Extremfällen schlechte Ergebnisse lieferte. Hätte man innerhalb der synthetischen Kohorte nicht auf eine gewisse Normalverteilung geachtet, sondern erlaubt, dass auch viele extreme Geometrien entstanden wären, so wäre ggf. eine höhere Genauigkeit entstanden.

Für die Zukunft wäre es zudem interessant zu schauen, ob durch das Verwenden anderer Methoden aus dem Bereich der KI, die zur Erzeugung von synthetischen Bilddaten bereits erfolgreich eingesetzt wurden, noch bessere Ergebnisse zu erzielen wären. Ein Beispiel wären sogenannte „generative adversarial networks“ (GAN), die sich durch eine noch höhere Flexibilität im Vergleich zum hier gewählten SSM auszeichnen, da sie sich nicht auf Formparametervektoren entlang definierter Hauptachsen begrenzen.^{97,98}

5. Zusammenfassung und Ausblick

In der vorliegenden Habilitationsschrift wurden die Inhalte von fünf wissenschaftlichen Arbeiten zum Thema Präzisionsmedizin in der Kinder- und Erwachsenenkardiologie auf Grundlage bildbasierter in silico Modellierung vorgestellt. Dabei wurde in Form einer Proof of Concept Studie die prinzipielle Durchführbarkeit der bildbasierten in silico Modellierung am Beispiel verschiedener Parameter der aortalen Hämodynamik gezeigt⁹ sowie die Validierung der Methodik gegen den klinischen Goldstandard des Herzkatheters präsentiert.¹⁹ An komplexen Patient*innen aus dem Bereich der Kinderkardiologie wurde die bildbasierte in silico Modellierung für eine konkrete klinische Fragestellung angewandt.²⁰ Zuletzt wurden zwei Optimierungsansätze vorgestellt, die einerseits den komplexen Arbeitsablauf der bildbasierten in silico Modellierung mittels KI vereinfachen^{21,22} sowie andererseits das Problem der existierenden klinischen Datenlücken überwinden sollen.²²

Zusammenfassend konnte gezeigt werden, dass bildbasierte in silico Modellierung des kardiovaskulären Systems das Potential hat, wichtige Informationen für Diagnostik und Behandlungsplanung nichtinvasiv und ohne jegliche Belastung für die Patient*in zu liefern. An verschiedenen Krankheitsbildern, wie den Herzklappenerkrankungen, Erkrankungen der thorakalen Aorta sowie angeborenen, univentrikulären Herzfehlern wurde ihre konkrete Anwendbarkeit gezeigt. Allerdings wurde auch das Problem des hohen Zeitaufwands sowie der erforderlichen, hohen Zeit- und Rechenleistungskapazität der numerischen Strömungssimulation für die klinische Translation beleuchtet. Als mögliche Optimierungsansätze wurden der Einsatz Künstlicher Intelligenz sowie synthetischer Patientenkollektive diskutiert.

Die Integration von KI-basierten Technologien in die verschiedenen Bildgebungsmodalitäten könnte in Zukunft nicht nur die diagnostische Aussagekraft der entsprechenden Untersuchungsmethode erweitern, sondern auch die Möglichkeit bieten, verschiedene Therapieoptionen noch während der Untersuchung selbst zu simulieren, um so diejenige Strategie zu identifizieren, die das beste postoperative oder -interventionelle Ergebnis zu liefern verspricht. Eine zusätzliche Repräsentanz der patientenindividuellen Herz- und Gefäßanatomie in Form eines sogenannten digitalen Zwillinges könnte einen weiteren Schritt in Richtung angewandte personalisierte Medizin darstellen.

Da es für eine erfolgreiche Anwendung KI-basierter Algorithmen in der Regel jedoch großer Datenmengen bedarf, welche insbesondere in kleineren Fachgebieten aber auch aufgrund immer strengerer Datenschutzrichtlinien und höherer Anforderungen an den individuellen Personenschutz häufig nicht zur Verfügung stehen, wird das Konzept der Datenaugmentierung durch synthetische Patientenkollektive in der Zukunft eine ebenso wichtige Rolle spielen. Dass synthetische

Patientenkohorten hilfreich sein können, existierende Datenlücken zu schließen, ist heute unumstritten. Für welche klinische Fragestellung jedoch dabei welche Methode der Kohortengenerierung die besten Ergebnisse liefert, wissen wir in vielen Fällen noch nicht. Hier gibt es gewiss noch eine Menge offener Fragen zu klären.

Das Gesundheitssystem der Zukunft ist ohne KI undenkbar. Ein verantwortungsvoller Einsatz KI-basierter Technologien wird den Ärzt*innen nicht nur bei der Entscheidungsfindung helfen, sondern auch zur Vorhersage von patientenindividuellen Behandlungsergebnissen beitragen und die Ära der Präzisionsmedizin in der kardiovaskulären Medizin einläuten.

Literaturverzeichnis

1. Currie G, Delles C. Precision Medicine and Personalized Medicine in Cardiovascular Disease. *Adv Exp Med Biol* 2018;1065:589-605.
2. Taylor CA, Fonte TA, Min JK. Computational fluid dynamics applied to cardiac computed tomography for noninvasive quantification of fractional flow reserve: scientific basis. *J Am Coll Cardiol* 2013;61:2233-41.
3. Morris PD, Narracott A, von Tengg-Kobligk H, et al. Computational fluid dynamics modelling in cardiovascular medicine. *Heart* 2016;102:18-28.
4. Yu KH, Beam AL, Kohane IS. Artificial intelligence in healthcare. *Nat Biomed Eng* 2018;2:719-31.
5. Ong CW, Wee I, Syn N, et al. Computational Fluid Dynamics Modeling of Hemodynamic Parameters in the Human Diseased Aorta: A Systematic Review. *Ann Vasc Surg* 2020;63:336-81.
6. Youssefi P, Gomez A, He T, et al. Patient-specific computational fluid dynamics-assessment of aortic hemodynamics in a spectrum of aortic valve pathologies. *J Thorac Cardiovasc Surg* 2017;153:8-20.e3.
7. Itu L, Neumann D, Mihalef V, et al. Non-invasive assessment of patient-specific aortic haemodynamics from four-dimensional flow MRI data. *Interface Focus* 2018;8:20170006.
8. Neugebauer M, Glöckler M, Goubergrits L, Kelm M, Kuehne T, Hennemuth A. Interactive virtual stent planning for the treatment of coarctation of the aorta. *Int J Comput Assist Radiol Surg* 2016;11:133-44.
9. Hellmeier F, Brüning J, Sündermann S, et al. Hemodynamic Modeling of Biological Aortic Valve Replacement Using Preoperative Data Only. *Front Cardiovasc Med* 2020;7:593709.
10. Hellmeier F, Nordmeyer S, Yevtushenko P, et al. Hemodynamic Evaluation of a Biological and Mechanical Aortic Valve Prosthesis Using Patient-Specific MRI-Based CFD. *Artif Organs* 2018;42:49-57.
11. Vellguth K, Brüning J, Goubergrits L, et al. Development of a modeling pipeline for the prediction of hemodynamic outcome after virtual mitral valve repair using image-based CFD. *Int J Comput Assist Radiol Surg* 2018;13:1795-805.
12. Rausch MK, Zöllner AM, Genet M, Baillargeon B, Bothe W, Kuhl E. A virtual sizing tool for mitral valve annuloplasty. *Int J Numer Method Biomed Eng* 2017;33.
13. van Bakel TMJ, Lau KD, Hirsch-Romano J, Trimarchi S, Dorfman AL, Figueroa CA. Patient-Specific Modeling of Hemodynamics: Supporting Surgical Planning in a Fontan Circulation Correction. *J Cardiovasc Transl Res* 2018;11:145-55.
14. Siallagan D, Loke YH, Olivieri L, et al. Virtual surgical planning, flow simulation, and 3-dimensional electrospinning of patient-specific grafts to optimize Fontan hemodynamics. *J Thorac Cardiovasc Surg* 2018;155:1734-42.

15. Rigatelli G, Chiastra C, Pennati G, Dubini G, Migliavacca F, Zuin M. Applications of computational fluid dynamics to congenital heart diseases: a practical review for cardiovascular professionals. *Expert Rev Cardiovasc Ther* 2021;19:907-16.
16. Peirlinck M, Costabal FS, Yao J, et al. Precision medicine in human heart modeling : Perspectives, challenges, and opportunities. *Biomech Model Mechanobiol* 2021;20:803-31.
17. Biglino G, Capelli C, Bruse J, Bosi GM, Taylor AM, Schievano S. Computational modelling for congenital heart disease: how far are we from clinical translation? *Heart* 2017;103:98-103.
18. Krittawong C, Zhang H, Wang Z, Aydar M, Kitai T. Artificial Intelligence in Precision Cardiovascular Medicine. *J Am Coll Cardiol* 2017;69:2657-64.
19. Franke B, Brüning J, Yevtushenko P, et al. Computed Tomography-Based Assessment of Transvalvular Pressure Gradient in Aortic Stenosis. *Front Cardiovasc Med* 2021;8:706628.
20. Schafstedde M, Yevtushenko P, Nordmeyer S, et al. Virtual treatment planning in three patients with univentricular physiology using computational fluid dynamics-Pitfalls and strategies. *Front Cardiovasc Med* 2022;9:898701.
21. Yevtushenko P, Goubergrits L, Franke B, Kuehne T, Schafstedde M. Modelling blood flow in patients with heart valve disease using deep learning: A computationally efficient method to expand diagnostic capabilities in clinical routine. *Frontiers in Cardiovascular Medicine* 2023;10.
22. Yevtushenko P, Goubergrits L, Gundelwein L, et al. Deep Learning Based Centerline-Aggregated Aortic Hemodynamics: An Efficient Alternative to Numerical Modelling of Hemodynamics. *IEEE J Biomed Health Inform* 2021;Pp.
23. Vadakkumpadan F, Arevalo H, Prassl AJ, et al. Image-based models of cardiac structure in health and disease. *Wiley Interdiscip Rev Syst Biol Med* 2010;2:489-506.
24. Chnafa C, Mendez S, Nicoud F, Moreno R, Nottin S, Schuster I. Image-based patient-specific simulation: a computational modelling of the human left heart haemodynamics. *Comput Methods Biomech Biomed Engin* 2012;15 Suppl 1:74-5.
25. Thamsen B, Yevtushenko P, Gundelwein L, et al. Synthetic Database of Aortic Morphometry and Hemodynamics: Overcoming Medical Imaging Data Availability. *IEEE Trans Med Imaging* 2021;40:1438-49.
26. Bruse JL, Zuluaga MA, Khushnood A, et al. Detecting Clinically Meaningful Shape Clusters in Medical Image Data: Metrics Analysis for Hierarchical Clustering Applied to Healthy and Pathological Aortic Arches. *IEEE Trans Biomed Eng* 2017;64:2373-83.
27. Casciaro ME, Craiem D, Chironi G, et al. Identifying the principal modes of variation in human thoracic aorta morphology. *J Thorac Imaging* 2014;29:224-32.
28. Lindroos M, Kupari M, Heikkilä J, Tilvis R. Prevalence of aortic valve abnormalities in the elderly: an echocardiographic study of a random population sample. *J Am Coll Cardiol* 1993;21:1220-5.

29. Nkomo VT, Gardin JM, Skelton TN, Gottdiener JS, Scott CG, Enriquez-Sarano M. Burden of valvular heart diseases: a population-based study. *Lancet* 2006;368:1005-11.
30. Horstkotte D, Loogen F. The natural history of aortic valve stenosis. *Eur Heart J* 1988;9 Suppl E:57-64.
31. Varadarajan P, Kapoor N, Bansal RC, Pai RG. Clinical profile and natural history of 453 nonsurgically managed patients with severe aortic stenosis. *Ann Thorac Surg* 2006;82:2111-5.
32. Kanwar A, Thaden JJ, Nkomo VT. Management of Patients With Aortic Valve Stenosis. *Mayo Clin Proc* 2018;93:488-508.
33. Vahanian A, Beyersdorf F, Praz F, et al. 2021 ESC/EACTS Guidelines for the management of valvular heart disease. *Eur Heart J* 2022;43:561-632.
34. Nordmeyer S, Hellmeier F, Yevtushenko P, et al. Abnormal aortic flow profiles persist after aortic valve replacement in the majority of patients with aortic valve disease: how model-based personalized therapy planning could improve results. A pilot study approach. *Eur J Cardiothorac Surg* 2020;57:133-41.
35. van Ooij P, Potters WV, Nederveen AJ, et al. A methodology to detect abnormal relative wall shear stress on the full surface of the thoracic aorta using four-dimensional flow MRI. *Magn Reson Med* 2015;73:1216-27.
36. Guzzardi DG, Barker AJ, van Ooij P, et al. Valve-Related Hemodynamics Mediate Human Bicuspid Aortopathy: Insights From Wall Shear Stress Mapping. *J Am Coll Cardiol* 2015;66:892-900.
37. Kari FA, Kocher N, Beyersdorf F, et al. Four-dimensional magnetic resonance imaging-derived ascending aortic flow eccentricity and flow compression are linked to aneurysm morphology†. *Interact Cardiovasc Thorac Surg* 2015;20:582-7; discussion 7-8.
38. Mahadevia R, Barker AJ, Schnell S, et al. Bicuspid aortic cusp fusion morphology alters aortic three-dimensional outflow patterns, wall shear stress, and expression of aortopathy. *Circulation* 2014;129:673-82.
39. Bilkh R, Jahangiri M, Otto CM. Patient-prosthesis mismatch following aortic valve replacement. *Heart* 2019;105:s28-s33.
40. Head SJ, Mokhles MM, Osnabrugge RL, et al. The impact of prosthesis-patient mismatch on long-term survival after aortic valve replacement: a systematic review and meta-analysis of 34 observational studies comprising 27 186 patients with 133 141 patient-years. *Eur Heart J* 2012;33:1518-29.
41. Dayan V, Vignolo G, Soca G, Paganini JJ, Brusich D, Pibarot P. Predictors and Outcomes of Prosthesis-Patient Mismatch After Aortic Valve Replacement. *JACC Cardiovasc Imaging* 2016;9:924-33.
42. Pibarot P, Dumesnil JG. Hemodynamic and clinical impact of prosthesis-patient mismatch in the aortic valve position and its prevention. *J Am Coll Cardiol* 2000;36:1131-41.

43. Fallon JM, DeSimone JP, Brennan JM, et al. The Incidence and Consequence of Prosthesis-Patient Mismatch After Surgical Aortic Valve Replacement. *Ann Thorac Surg* 2018;106:14-22.
44. Pibarot P, Weissman NJ, Stewart WJ, et al. Incidence and sequelae of prosthesis-patient mismatch in transcatheter versus surgical valve replacement in high-risk patients with severe aortic stenosis: a PARTNER trial cohort--a analysis. *J Am Coll Cardiol* 2014;64:1323-34.
45. Sá M, de Carvalho MMB, Sobral Filho DC, et al. Surgical aortic valve replacement and patient-prosthesis mismatch: a meta-analysis of 108 182 patients. *Eur J Cardiothorac Surg* 2019;56:44-54.
46. Chen J, Lin Y, Kang B, Wang Z. Indexed effective orifice area is a significant predictor of higher mid- and long-term mortality rates following aortic valve replacement in patients with prosthesis-patient mismatch. *Eur J Cardiothorac Surg* 2014;45:234-40.
47. Karmonik C, Partovi S, Davies MG, et al. Integration of the computational fluid dynamics technique with MRI in aortic dissections. *Magn Reson Med* 2013;69:1438-42.
48. Numata S, Itatani K, Kanda K, et al. Blood flow analysis of the aortic arch using computational fluid dynamics. *Eur J Cardiothorac Surg* 2016;49:1578-85.
49. Kelm M, Goubergrits L, Bruening J, et al. Model-Based Therapy Planning Allows Prediction of Haemodynamic Outcome after Aortic Valve Replacement. *Sci Rep* 2017;7:9897.
50. Brown ML, Burkhart HM, Connolly HM, et al. Coarctation of the aorta: lifelong surveillance is mandatory following surgical repair. *J Am Coll Cardiol* 2013;62:1020-5.
51. Kenny D, Hijazi ZM. Coarctation of the aorta: from fetal life to adulthood. *Cardiol J* 2011;18:487-95.
52. Tanous D, Benson LN, Horlick EM. Coarctation of the aorta: evaluation and management. *Curr Opin Cardiol* 2009;24:509-15.
53. Suradi H, Hijazi ZM. Current management of coarctation of the aorta. *Glob Cardiol Sci Pract* 2015;2015:44.
54. Erben Y, Oderich GS, Verhagen HJM, et al. Multicenter experience with endovascular treatment of aortic coarctation in adults. *J Vasc Surg* 2019;69:671-9.e1.
55. Baumgartner H, Bonhoeffer P, De Groot NM, et al. ESC Guidelines for the management of grown-up congenital heart disease (new version 2010). *Eur Heart J* 2010;31:2915-57.
56. Goubergrits L, Riesenkampff E, Yevtushenko P, et al. Is MRI-based CFD able to improve clinical treatment of coarctations of aorta? *Ann Biomed Eng* 2015;43:168-76.
57. Goubergrits L, Riesenkampff E, Yevtushenko P, et al. MRI-based computational fluid dynamics for diagnosis and treatment prediction: clinical validation study in patients with coarctation of aorta. *J Magn Reson Imaging* 2015;41:909-16.

58. Kverneland LS, Kramer P, Ovroutski S. Five decades of the Fontan operation: A systematic review of international reports on outcomes after univentricular palliation. *Congenit Heart Dis* 2018;13:181-93.
59. Elias P, Poh CL, du Plessis K, et al. Long-term outcomes of single-ventricle palliation for pulmonary atresia with intact ventricular septum: Fontan survivors remain at risk of late myocardial ischaemia and death. *Eur J Cardiothorac Surg* 2018;53:1230-6.
60. Schafstedde M, Nordmeyer S, Schleiger A, et al. Persisting and reoccurring cyanosis after Fontan operation is associated with increased late mortality. *Eur J Cardiothorac Surg* 2021;61:54-61.
61. Srivastava D, Preminger T, Lock JE, et al. Hepatic venous blood and the development of pulmonary arteriovenous malformations in congenital heart disease. *Circulation* 1995;92:1217-22.
62. Justino H, Benson LN, Freedom RM. Development of unilateral pulmonary arteriovenous malformations due to unequal distribution of hepatic venous flow. *Circulation* 2001;103:E39-40.
63. Shinohara T, Yokoyama T. Pulmonary arteriovenous malformation in patients with total cavopulmonary shunt: what role does lack of hepatic venous blood flow to the lungs play? *Pediatr Cardiol* 2001;22:343-6.
64. Lee J, Menkis AH, Rosenberg HC. Reversal of pulmonary arteriovenous malformation after diversion of anomalous hepatic drainage. *Ann Thorac Surg* 1998;65:848-9.
65. Warmerdam E, Krings GJ, Leiner T, Grotenhuis HB. Three-dimensional and four-dimensional flow assessment in congenital heart disease. *Heart* 2020;106:421-6.
66. Haggerty CM, de Zélicourt DA, Restrepo M, et al. Comparing pre- and post-operative Fontan hemodynamic simulations: implications for the reliability of surgical planning. *Ann Biomed Eng* 2012;40:2639-51.
67. Dumesnil JG, Honos GN, Lemieux M, Beauchemin J. Validation and applications of indexed aortic prosthetic valve areas calculated by Doppler echocardiography. *J Am Coll Cardiol* 1990;16:637-43.
68. Pibarot P, Dumesnil JG, Jobin J, Lemieux M, Honos G, Durand LG. Usefulness of the indexed effective orifice area at rest in predicting an increase in gradient during maximum exercise in patients with a bioprosthesis in the aortic valve position. *Am J Cardiol* 1999;83:542-6.
69. Lancellotti P, Pibarot P, Chambers J, et al. Recommendations for the imaging assessment of prosthetic heart valves: a report from the European Association of Cardiovascular Imaging endorsed by the Chinese Society of Echocardiography, the Inter-American Society of Echocardiography, and the Brazilian Department of Cardiovascular Imaging. *Eur Heart J Cardiovasc Imaging* 2016;17:589-90.
70. Taron J, Foldyna B, Eslami P, Hoffmann U, Nikolaou K, Bamberg F. Cardiac Computed Tomography - More Than Coronary Arteries? A Clinical Update. *Rofo* 2019;191:817-26.

71. Nakahara T, Toyama T, Jinzaki M, et al. Quantitative Analysis of Iodine Image of Dual-energy Computed Tomography at Rest: Comparison With 99mTc-Tetrofosmin Stress-rest Single-photon Emission Computed Tomography Myocardial Perfusion Imaging as the Reference Standard. *J Thorac Imaging* 2018;33:97-104.
72. Coenen A, Rossi A, Lubbers MM, et al. Integrating CT Myocardial Perfusion and CT-FFR in the Work-Up of Coronary Artery Disease. *JACC Cardiovasc Imaging* 2017;10:760-70.
73. Zoghbi WA, Enriquez-Sarano M, Foster E, et al. Recommendations for evaluation of the severity of native valvular regurgitation with two-dimensional and Doppler echocardiography. *J Am Soc Echocardiogr* 2003;16:777-802.
74. Baumgartner H, Stefenelli T, Niederberger J, Schima H, Maurer G. "Overestimation" of catheter gradients by Doppler ultrasound in patients with aortic stenosis: a predictable manifestation of pressure recovery. *J Am Coll Cardiol* 1999;33:1655-61.
75. Minners J, Allgeier M, Gohlke-Baerwolf C, Kienzle RP, Neumann FJ, Jander N. Inconsistencies of echocardiographic criteria for the grading of aortic valve stenosis. *Eur Heart J* 2008;29:1043-8.
76. Minners J, Allgeier M, Gohlke-Baerwolf C, Kienzle RP, Neumann FJ, Jander N. Inconsistent grading of aortic valve stenosis by current guidelines: haemodynamic studies in patients with apparently normal left ventricular function. *Heart* 2010;96:1463-8.
77. Wong S, Spina R, Toemoe S, Dhital K. Is cardiac magnetic resonance imaging as accurate as echocardiography in the assessment of aortic valve stenosis? *Interact Cardiovasc Thorac Surg* 2016;22:480-6.
78. Lafanechère A, Albaladejo P, Raux M, et al. Cardiac output measurement during infrarenal aortic surgery: echo-esophageal Doppler versus thermodilution catheter. *J Cardiothorac Vasc Anesth* 2006;20:26-30.
79. Fontan F, Baudet E. Surgical repair of tricuspid atresia. *Thorax* 1971;26:240-8.
80. Trusty PM, Slesnick TC, Wei ZA, et al. Fontan Surgical Planning: Previous Accomplishments, Current Challenges, and Future Directions. *J Cardiovasc Transl Res* 2018;11:133-44.
81. Fogel MA, Khiabani RH, Yoganathan A. Imaging for preintervention planning: pre- and post-Fontan procedures. *Circ Cardiovasc Imaging* 2013;6:1092-101.
82. Slesnick TC, Yoganathan AP. Computational modeling of Fontan physiology: at the crossroads of pediatric cardiology and biomedical engineering. *Int J Cardiovasc Imaging* 2014;30:1073-84.
83. de Zélicourt DA, Marsden A, Fogel MA, Yoganathan AP. Imaging and patient-specific simulations for the Fontan surgery: current methodologies and clinical applications. *Prog Pediatr Cardiol* 2010;30:31-44.
84. Sundareswaran KS, de Zélicourt D, Sharma S, et al. Correction of pulmonary arteriovenous malformation using image-based surgical planning. *JACC Cardiovasc Imaging* 2009;2:1024-30.

85. Trusty PM, Wei ZA, Slesnick TC, et al. The first cohort of prospective Fontan surgical planning patients with follow-up data: How accurate is surgical planning? *J Thorac Cardiovasc Surg* 2019;157:1146-55.
86. Daley PJ, Sagar KB, Wann LS. Doppler echocardiographic measurement of flow velocity in the ascending aorta during supine and upright exercise. *Br Heart J* 1985;54:562-7.
87. Ennezat PV, Maréchaux S, Iung B, Chauvel C, LeJemtel TH, Pibarot P. Exercise testing and exercise stress echocardiography in asymptomatic aortic valve stenosis. *Heart* 2009;95:877-84.
88. Su B, Zhang JM, Zou H, Ghista D, Le TT, Chin C. Generating wall shear stress for coronary artery in real-time using neural networks: Feasibility and initial results based on idealized models. *Comput Biol Med* 2020;126:104038.
89. Jordanski M, Radovic M, Milosevic Z, Filipovic N, Obradovic Z. Machine Learning Approach for Predicting Wall Shear Distribution for Abdominal Aortic Aneurysm and Carotid Bifurcation Models. *IEEE J Biomed Health Inform* 2018;22:537-44.
90. Liang L, Mao W, Sun W. A feasibility study of deep learning for predicting hemodynamics of human thoracic aorta. *J Biomech* 2020;99:109544.
91. Annabi MS, Touboul E, Dahou A, et al. Dobutamine Stress Echocardiography for Management of Low-Flow, Low-Gradient Aortic Stenosis. *J Am Coll Cardiol* 2018;71:475-85.
92. Picano E, Pibarot P, Lancellotti P, Monin JL, Bonow RO. The emerging role of exercise testing and stress echocardiography in valvular heart disease. *J Am Coll Cardiol* 2009;54:2251-60.
93. Romagnoli S, Ricci Z, Quattrone D, et al. Accuracy of invasive arterial pressure monitoring in cardiovascular patients: an observational study. *Crit Care* 2014;18:644.
94. McWilliams RG, Robertson I, Smye SW, Wijesinghe L, Kessel D. Sources of error in intra-arterial pressure measurements across a stenosis. *Eur J Vasc Endovasc Surg* 1998;15:535-40.
95. Li X, Yang Q, Wang Z, Wei D. Shear stress in atherosclerotic plaque determination. *DNA Cell Biol* 2014;33:830-8.
96. Wentzel JJ, Chatzizisis YS, Gijsen FJ, Giannoglou GD, Feldman CL, Stone PH. Endothelial shear stress in the evolution of coronary atherosclerotic plaque and vascular remodelling: current understanding and remaining questions. *Cardiovasc Res* 2012;96:234-43.
97. Creswell A, White T, Dumoulin V, Arulkumaran K, Sengupta B, Bharath AA. Generative Adversarial Networks: An Overview. *IEEE Signal Processing Magazine* 2018;35:53-65.
98. Zhang H, Xu T, Li H, et al. StackGAN++: Realistic Image Synthesis with Stacked Generative Adversarial Networks. *IEEE Trans Pattern Anal Mach Intell* 2019;41:1947-62.

Danksagung

An dieser Stelle möchte ich allen beteiligten Personen danken, die mich bei der Anfertigung dieser Arbeit unterstützt haben.

Mein besonderer Dank gilt Herrn Prof. Dr. med. Felix Berger, Klinikdirektor der Abteilung Kinderkardiologie und Angeborene Herzfehler des Deutschen Herzzentrums der Charité, für seine kontinuierliche und stets wohlwollende Unterstützung meines klinischen und wissenschaftlichen Werdegangs.

Ebenfalls bedanken möchte ich mich bei Herrn Prof. Dr. med. Titus Kühne für sein Vertrauen und die außergewöhnliche Förderung zu Beginn meiner Forschungsarbeit. Für stets neue große Ideen und viele inspirierende und motivierende Gespräche bin ich ihm zu ganz besonderem Dank verpflichtet.

Weiterhin möchte ich meinen Kolleginnen und Kollegen des Instituts für kardiovaskuläre Computer-assistierte Medizin danken für die freundschaftliche Arbeitsatmosphäre, viele wertvolle Anregungen und die stete Hilfsbereitschaft, die wesentlich zum Gelingen dieser Arbeit beigetragen haben. Insbesondere bei Sarah Nordmeyer, Leonid Goubergrits, Florian Hellmeier, Pavlo Yevtushenko und Jan Brüning möchte ich mich für die außerordentlich gute Zusammenarbeit der letzten Jahre sowie für ihre ansteckende Begeisterung an der Forschung bedanken.

Dem Berliner Institut für Gesundheitsforschung danke ich für das mir gewährte Privileg, neben meiner klinischen Ausbildung in geschützter Zeit zu forschen.

Auch meinen ärztlichen und pflegerischen Kolleginnen und Kollegen aus der Abteilung für Kinderkardiologie und Angeborene Herzfehler des Deutschen Herzzentrums der Charité möchte ich für die herzliche und spannende Zusammenarbeit danken. Prof. Dr. med. Katharina Schmitt danke ich für ihre zuverlässige, fördernde und fordernde Betreuung in den letzten Jahren.

Von ganzem Herzen danke ich meiner Familie, meinen Eltern und meinem Mann für ihren Zuspruch und ihre fortwährend liebevolle Unterstützung, in guten wie in schweren Zeiten. Tief verbunden und dankbar bin ich meiner verstorbenen Mutter, der ich diese Arbeit widme.

Erklärung

§ 4 Abs. 3 (k) der HabOMed der Charité

Hiermit erkläre ich, dass

- weder früher noch gleichzeitig ein Habilitationsverfahren durchgeführt oder angemeldet wurde,
- die vorgelegte Habilitationsschrift ohne fremde Hilfe verfasst, die beschriebenen Ergebnisse selbst gewonnen sowie die verwendeten Hilfsmittel, die Zusammenarbeit mit anderen Wissenschaftler*innen und mit technischen Hilfskräften sowie die verwendete Literatur vollständig in der Habilitationsschrift angegeben wurden,
- mir die geltende Habilitationsordnung bekannt ist.

Ich erkläre ferner, dass mir die Satzung der Charité – Universitätsmedizin Berlin zur Sicherung Guter Wissenschaftlicher Praxis bekannt ist und ich mich zur Einhaltung dieser Satzung verpflichte.

.....
Datum

.....
Unterschrift